Graduate School ETD Form 9
(Revised 12/07)

PURDUE UNIVERSITY
GRADUATE SCHOOL
Thesis/Dissertation Acceptance

This is to certify that the thesis/dissertation prepared

By PRASHANT SRINIVASAN

Entitled INVESTIGATION OF QUANTUM FLUCTUATIONS IN A NONLINEAR INTERFEROMETER WITH HARMONIC GENERATION AND COHERENT INTERACTION OF LIGHT AND CS ATOMS

For the degree of Doctor of Philosophy

Is approved by the final examining committee:

Dr. Z. Y. Ou
Chair

Dr. R. S. DECCA

Dr. G. VEMURI

Dr. H. I. PETRACHE

To the best of my knowledge and as understood by the student in the *Research Integrity and Copyright Disclaimer (Graduate School Form 20)*, this thesis/dissertation adheres to the provisions of Purdue University's "Policy on Integrity in Research" and the use of copyrighted material.

Approved by Major Professor(s): Dr. Z. Y. Ou

Approved by: Dr. R. S. DECCA 11/06/2012
Head of the Graduate Program Date

Graduate School Form 20
(Revised 9/10)

PURDUE UNIVERSITY
GRADUATE SCHOOL

Research Integrity and Copyright Disclaimer

Title of Thesis/Dissertation:

INVESTIGATION OF QUANTUM FLUCTUATIONS IN A NONLINEAR INTERFEROMETER WITH HARMONIC GENERATION AND COHERENT INTERACTION OF LIGHT AND CS ATOMS

For the degree of Doctor of Philosophy

I certify that in the preparation of this thesis, I have observed the provisions of *Purdue University Executive Memorandum No. C-22,* September 6, 1991, *Policy on Integrity in Research.**

Further, I certify that this work is free of plagiarism and all materials appearing in this thesis/dissertation have been properly quoted and attributed.

I certify that all copyrighted material incorporated into this thesis/dissertation is in compliance with the United States' copyright law and that I have received written permission from the copyright owners for my use of their work, which is beyond the scope of the law. I agree to indemnify and save harmless Purdue University from any and all claims that may be asserted or that may arise from any copyright violation.

PRASHANT SRINIVASAN

Printed Name and Signature of Candidate

11/06/2012

Date (month/day/year)

*Located at http://www.purdue.edu/policies/pages/teach_res_outreach/c_22.html

INVESTIGATION OF QUANTUM FLUCTUATIONS IN A NONLINEAR INTERFEROMETER WITH HARMONIC GENERATION AND COHERENT INTERACTION OF LIGHT AND CS ATOMS

A Dissertation

Submitted to the Faculty

of

Purdue University

by

Prashant Srinivasan

In Partial Fulfillment of the

Requirements for the Degree

of

Doctor of Philosophy

December 2012

Purdue University

Indianapolis, Indiana

To my parents, whose love, strength and encouragement made this possible.

ACKNOWLEDGMENTS

This dissertation would not have been possible without the guidance of several individuals who contributed to the completion of this study.

First and foremost, I am indebted to my advisor Prof. Z. Y. Ou for sharing his experience, patience and whose guidance has made this momentous occasion possible. Prof. G. Vemuri, for generosity with equipment, suggestions, constant encouragement and the fantastic class on lasers! Prof R. S. Decca, who alleviated dull days in the dungeon by periodically trying to hunt me down for those oscilloscopes and for the useful comments that improved this manuscript. Prof. A. Gavrin, for his patience and steadfast encouragement throughout my academic career. Prof. H. Petrache, teacher extraordinaire, motivator and friend, for your unfailing support and inspiration. Tom Halmser (Purdue) and Joe Heurkampf (IUPUI MET), for lending your machine design expertise. Prof. V. Natarajan and Prof. A. Selvarajan, Indian Institute of Science, for introducing me to research.

No graduate school experience is complete without the love and support of friends and colleagues. Derek Scott, for unreserved generosity. Joe Suelzer, for pushing me to break running records. Dr. John "Rambo" Ross for your mentoring and advice. My dearest and best friend Megan Koerner, who was always there to give me a boost when things did not work. Edwin Tham, your computational genius saved me months of work. Connie Ely and Kelly Miholic, the most amazing office staff for your unfailing kindness and patience. Jennifer Neisivich (IUPUI OIA), for assistance with my VISA.

Last but not the least, my family, for sacrificing so much to see me succeed.

TABLE OF CONTENTS

Page

LIST OF TABLES

LIST OF FIGURES

Figure Page

ABSTRACT

Srinivasan, Prashant Ph.D., Purdue University, December 2012. Investigation of quantum fluctuations in a nonlinear interferometer with harmonic generation and coherent interaction of light and Cs atoms . Major Professor: Zhe-Yu Jeff Ou.

In the first part of this thesis, we investigate the propagation of quantum fluctuations in a nonlinear interferometer comprising under conditions of harmonic generation by computer simulations. This investigation assumes idealized conditions such as lossless and uniform nonlinear media, an ideal cavity and ideal photodetectors. After linearizing wave equations for harmonic generation with a coherent state input, we obtain equations for one dimensional spatial propagation of the mean field and quantum fluctuations for initial conditions set by arbitrary interferometer phase. We discover that fluctuations are de-squeezed in the X and Y quadratures as the interferometer phase is tuned. However, we discover that there is are quadratures P-Q obtained by rotating the X-Y quadratures for which squeezing is improved by factors of 10^9. We present a practical idea to implement rotation of X quadrature fluctuations to the Q quadrature by using an ideal empty optical cavity. Signal-to-Noise ratio of the nonlinear interferometer was calculated and compared with that of a linear interferometer with coherent state input. We calculated a maximum performance improvement of a factor of 60 for a normalized propagation length $\zeta_0 = 3$ under ideal conditions. In the second part of this thesis, we investigate experimental arrangements to transfer atomic coherence from light to cesium atoms. We discuss the experimental arrangement to generate coherence under conditions of electromagnetically induced transparency (EIT). We measure a continuous wave EIT width of 7.18 MHz and present results for pulsed arrangements.

PART I: QUANTUM FLUCTUATIONS IN A NONLINEAR INTERFEROMETER WITH HARMONIC GENERATION

1. INTRODUCTION

1.1 Precision Measurements

Experiments have played an unequivocal role in the development of physics [1, 2]. Within the realm of experimental physics, precision measurements have a long and rich history in contributing to our understanding of nature [3]. While the motivation for precision measurements has remained the same, with the advent of quantum physics, the "tools of the trade" have become increasingly sophisticated. Almost all current precision measurement techniques rely on some aspect of quantum theory. The cornerstone of precision measurements is based on the Heisenberg uncertainty principle, which asserts that there exists a fundamental lower bound on the precision with which certain pairs of physical properties of an object can be simultaneously known. One can also argue that since measurements require energy we cannot determine a physical quantity to infinite accuracy as it would require infinite energy. The difference between measurements in classical and quantum theory is that in quantum theory, uncertainties in measurements are due to the structure of the theory itself, whereas in classical physics uncertainties are due experimental factors that may be eliminated by improving the quality of measurement procedures. A common theme among precision techniques is to exploit the sensitivity of quantum states to small variations in external parameters (such as phase). In practice, we can use either discrete quantum variables such as photon number, or continuous variables such as the quadrature amplitudes of light for measurements. It is therefore useful to understand the limits of such quantum measurement devices. The earliest and perhaps most useful example of such an approach is interferometry.

1.2 Interferometry

Interference occurs when radiation follows more than one path from its source to the point of detection. The striking feature of interference is the redistribution of energy, which manifests as a departure from the law of addition of intensities. Derived from interference is the technique of interferometry, one of the most important measurement techniques with applications in other branches of science. The development of optical interferometry extends over 300 years and is closely linked with the history of wave optics. In the 1600's Hook and Boyle put forward the wave theory of light to explain interference of light reflected by a film, which was expanded by Huygens in 1690. In 1801 and 1803 Thomas Young explained the principle of superposition of light and the theory in its final form was perfected by Fresnel in 1818 [4]. An interferometer is a device that measures small lengths and phase shifts [5]. The physical principle exploited is the superposition of field amplitudes. In its simplest form, a generic interferometer is a four port device that consists of two input channels, an interaction region and two output channels. An input coherent field is split into two arms, one of which is the phase sensing field. The phase sensing field interacts with the system under study and acquires a phase shift. This phase-sensing field is then superposed with the unmodified field at the output. Any changes that occur in the system under study modify the output and the desired information about the system under investigation can be extracted from the output signal. This is the basic principle of interferometry.

Broadly speaking, we can divide interferometers into two classes, matter interferometers (ex. BEC's, cold atoms) [6] and electromagnetic interferometers, where the fields employed are photons. Optical interferometers are the most commonly used subgroup of electromagnetic interferometers. Optical Interferometry is a widely applied technique in sensitive measurements and has resulted in basic experiments starting with the famous Michaelson-Morley experiment to measure the speed of light [7].

1.3 Interferometer Phase Sensitivity and Precision

The dictionary definition of the word sensitivity is given as the *"degree of susceptibility to stimulation"* [8]. In the context of an interferometer, the response is the formation of interference fringes and the quality of this response is the fringe visibility [5]. Another useful evaluation metric is Signal-to-Noise ratio (SNR) which is defined as the ratio of signal power to noise power. The classical phase sensitivity of an interferometer is defined as the smallest phase change that generates a measurable output. However, this description is incomplete and does not work for weak fields. Also, implied within such a definition is the assumption that in principle, one can have an interferometer of infinite sensitivity because, according to classical theory, noise is deterministic and all experimental noise sources can, in principle, be eliminated. A practical interferometer cannot measure phase differences with arbitrary precision. A quantum mechanically formulated definition is given by the unity SNR criterion. According to this definition, the minimum detectable phase shift is the one where the signal equals the noise. The difference between quantum and classical definitions is that in quantum theory, noise (given as the variance) cannot be eliminated. In sections 1.4 and 1.5 we discuss two important limits pertaining to quantum noise.

1.4 Standard Quantum Limit (SQL)

The sensitivity of a practical interferometer is encapsulated by the so called "Standard Quantum Limit" (SQL). The standard quantum limit (SQL) is a consequence of Heisenberg's Uncertainty Principle and sets a limit to the sensitivity of a continuous measurement (monitoring) of a quantity that does not commute with itself at different times. For example, in the gravitational wave interferometer, the SQL has contributions from both shot noise and radiation pressure noise. Shot noise is associated with the "irregularity" or discontinuities in flow of electronic current (assuming an ideal photodetector, photon statistics are transferred to the electronic current). We can attribute shot noise to the Poissonian statistics of photons exhibited by laser

light as there is a one to one correlation between the arrival of a photon wave-packet and the generation of the photo-current.

In literature, it is common to see the use of the terms *Shot noise* and SQL interchangeably. The nomenclature depends on the context. For low intensity fields, the major contribution to measurement uncertainty is due to the *Shot Noise*, whereas for strong fields such as those employed in the LIGO project, the major factor is radiation pressure noise.

The best precision in phase measurement which can be obtained using classical states of light (light that exhibits Poissonian statistics) scales as $\frac{1}{\sqrt{N}}$, where N is the number of photons in the sensing beam. Traditional interferometers operate above or at best, at the SQL and therefore a large body of research is devoted to designing devices that operate below the standard quantum limit [9]. A 'classical' solution to decrease the *Shot noise* consists of an increase of the circulating light power. A higher optical power inside the interferometer will, however, lead to thermally-induced beam distortion as well as to an increased radiation pressure noise. Therefore, something else has to be done.

1.5 Heisenberg Limit (HL)

In the previous sections we discussed a practical limit to precision measurements with a classical (coherent) state called the SQL. However, it turns out that this is not a fundamental limit. In general, the HL can be defined as the uncertainty in the value of an unknown parameter $\Delta\phi$ of an observable $\mathcal{X}$ given by the rule $\Delta\phi \geq \frac{1}{N}$, where N is the number of physical systems in the probe (number of photons) [10–12].

Current research has placed more demands on the sensitivity of an interferometer and the need for interferometers that go beyond the SQL is urgently necessary [13]. The Advanced LIGO project [14] for example, the experimental search for gravitational waves predicted by the general theory of relativity, requires a sensitivity that

goes beyond the (SQL) [15, 16]. This has led to developing theoretical and experimental schemes to approach the Heisenberg limit [17].

Increasing beam power alone does not improve the noise performance. If an experiment has to be improved, an obvious candidate for improvement would be the measuring device or an active component in the measuring device. In our case, the measuring device is the interferometer and the active component is light itself. The modification of the quantum state of light has taken two approaches: Techniques that use discrete variables, such as photon number, and techniques that use continuous variables, such as the quadrature amplitudes of the electromagnetic field. Most of the focus in the past was on using non-classical states of light (light exhibiting sub-Poissonian statistics) to improve measurement precision beyond the SQL.

Use of the so-called squeezed states of light [18] as a probe was first proposed by Caves [10]. Such a light field has a characteristic non-classical noise distribution in the field quadratures, the relevant point being a reduction in fluctuation of amplitudes.

Experiments have used non-classical light input such as squeezed states and the so called maximally entangled NOON states [19, 20]. In all these approaches, the interferometer itself was not modified, i.e. the interferometer used linear optical elements, only the input state of light was changed. While the problem was solved in theory, there were many practical difficulties that prevented widespread implementation of linear interferometers with quantum sources. The main drawback in schemes that use non-classical light sources is the difficulty in generating sufficiently bright non-classical light and their fragility due to un-avoidable losses in experiments. Nonetheless, the principle of modifying a traditional interferometer to improve sensitivity resulted in new and interesting physics [21].

1.6 Nonlinear Interferometry

In the previous sections, we discussed some aspects of current research, the use of squeezed light to improve measurement precision and experimental drawbacks that were encountered.

This thesis takes a different approach to the works cited earlier. In a series of important papers by Yurke [22] and Ou [9] , the possibility of replacing the linear optics of an interferometer (see figure 1.1) with nonlinear beam splitters (NLBS) was investigated (see figure 1.2). Ou in particular cast the problem in terms of a unitary transformation process, where the nonlinear medium acts as a generator of squeezing. The main advantage is that there is no need to use a special probe with non-classical photon statistics. In this scheme, a coherent state is injected into the input NLBS. The light interacts with the NLBS and a second harmonic is generated [23]. The unconverted fundamental field is the phase sensing beam. Ou showed that the phase sensing beam (probe)undergoes intensity squeezing, i.e has intensity fluctuations that are far below the vacuum noise level. In fact, we are generating squeezed light within the system itself and more importantly, the intensity of the probe beam can be controlled experimentally. The fundamental and second harmonic light are then combined on the output NLBS, which is setup for parametric downconversion and measurements are made on the phase sensing beam at the output.

To fully understand the feasibility of this approach, it is necessary to first understand how quantum fluctuations evolve in a nonlinear medium and this is the focus of our investigation. The main theory [9, 24, 25] and its experimental realization [26] in the context of parametric amplifiers was developed by Ou.

We investigate a nonlinear interferometer based on harmonic generation and our calculations show that we can expect an improvement of a factor of 60 over a linear interferometer.

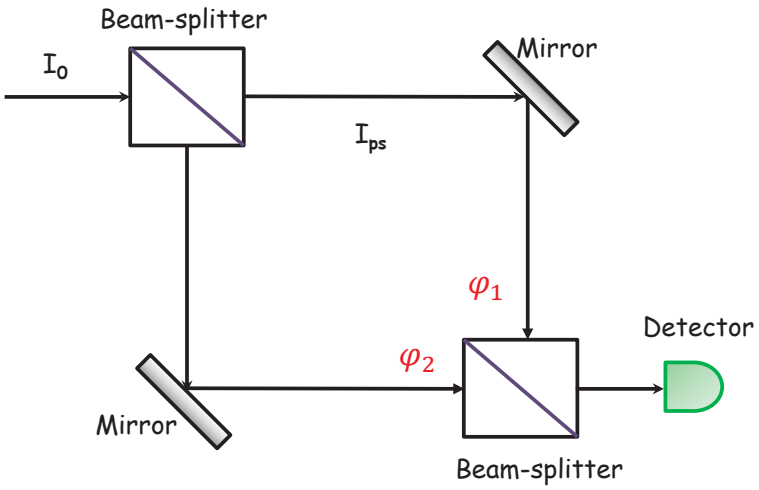

Figure 1.1. Schematic of a normal interferometer. Linear optical elements are used.

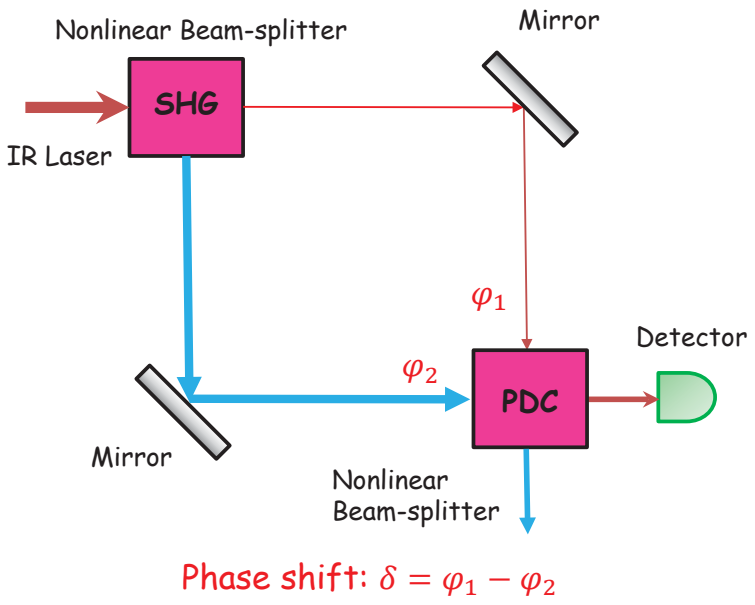

Figure 1.2. A schematic representation of a nonlinear interferometer with beamsplitters replaced by nonlinear crystals (in pink) operating under conditions of harmonic generation (SHG) and parametric downconversion (PDC).

2. SINGLE PASS HARMONIC GENERATION AND PARAMETRIC DOWNCONVERSION

2.1 Introduction

Optical nonlinearity is quantified by the dependence of the dipole moment per unit volume (polarization) of the medium on the electric field strength of the light. The normal response of a medium to light is linear and as a consequence most optical phenomena can be described with a linear refractive index. With the advent of laser sources the available optical power level increased to a level where the response of the medium started to deviate from the linear behavior. It was discovered that at sufficiently high light intensities the response of the material depends on the light intensity (E^2). This gave birth to the field of nonlinear optics and led to a flood of interesting phenomena such as second harmonic and sum, difference frequency generation [23, 27]. Harmonic generation has found wide applications in diverse areas such as engineering, consumer electronics and medicine [28].

Most of the above mentioned applications in diverse areas exploit the classical features (mainly intensity) of the Harmonic generation process. In this thesis we focus on the quantum properties of the generated light. More specifically, we are interested in the propagation of quantum fluctuations or "squeezing" of the intensity fluctuations. This chapter is organized as follows, in section 2.2, we revisit well known classical theory of harmonic generation, in section 2.3 we discuss the motivation for working with continuous quantum variables and we solve the spatial propagation equations obtaining solutions for the propagation of the mean field, in section 2.3 we explore in the use of field quadratures in detail and derive equations for propagation of quantum fluctuations for a couple of special cases.

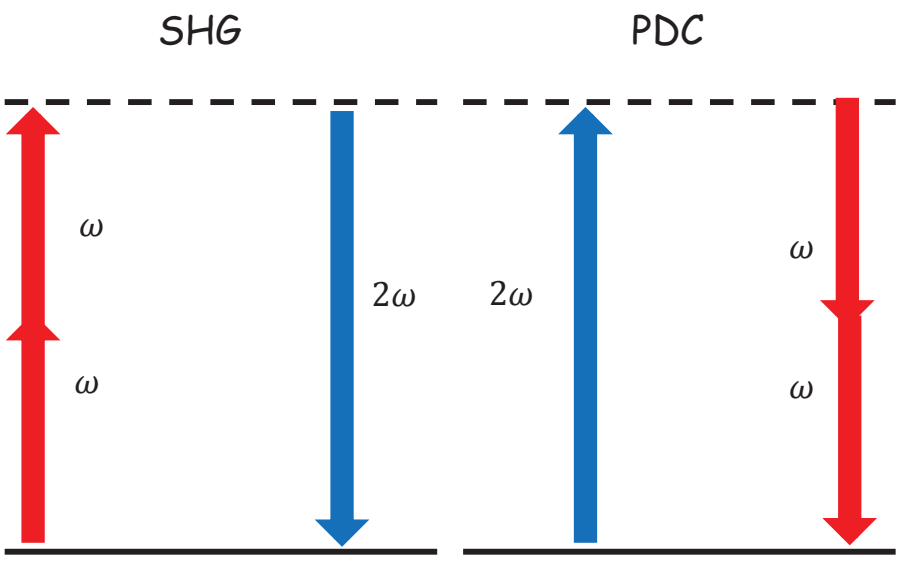

Figure 2.1. Physical processes of harmonic generation (SHG) and parametric downconversion (PDC).

2.2 Classical Field Equations

Second harmonic generation (SHG) is a nonlinear process in which light of frequency ω (fundamental) is converted to light at 2ω (second harmonic) by eliciting a nonlinear response from a dielectric medium. The reverse process is known as parametric downconversion (PDC). The theory of conversion from fundamental to harmonic is well known and is governed by nonlinear propagation equations. These equations are obtained by solving the electromagnetic wave equation with the polarization of the medium as the source term and are described in standard books on nonlinear optics [23, 29]. Nonetheless it is useful to summarize the basic ideas for clarity of the subsequent discussion.

The polarization of a medium can be written as a sum of its linear and nonlinear response to an optical field as

$$\vec{\mathbf{P}}(z,t) = \vec{\mathbf{P}}^{(L)}(z,t) + \vec{\mathbf{P}}^{(NL)}(z,t), \tag{2.1}$$

where $\vec{\mathbf{P}}^{(L)}(z,t)$ is the linear polarization and $\vec{\mathbf{P}}^{(NL)}(z,t)$ is the nonlinear polarization of the medium as a function of position and time.

Wave mixing is a phenomena where light of different frequencies interact with a nonlinear medium and generate additional frequencies. For a general wave-mixing problem, the nonlinear response of the medium can be written as a sum of the responses due to each field. Harmonic generation is a special case of wave-mixing.

In general, the second order nonlinear polarization that describes wave mixing can be written as [23]

$$P_i\left(\omega_n + \omega_m\right) = \epsilon_0 \sum_{\mathrm{jk}} \sum_{(\mathrm{nm})} \chi^{(2)}_{\mathrm{ijk}}\left(\omega_n + \omega_m, \omega_n, \omega_m\right) E_j\left(\omega_n\right) E_k\left(\omega_m\right), \tag{2.2}$$

where $\chi^{(2)}_{ijk}$ is the second order nonlinear susceptibility, i, j, k are cartesian components of the fields and $n, m = 1, 2$ label the fields. In harmonic generation $\omega_1 = \omega_2$ and $\omega_3 = 2\omega_1$. Equation 2.2 can be written as [23]

$$P_i\left(2\omega_1\right) = \epsilon_0 \sum_{\mathrm{jk}} \chi^{(2)}_{\mathrm{ijk}}\left(2\omega_1, \omega_1, \omega_1\right) E_j\left(\omega_1\right) E_k\left(\omega_1\right), \tag{2.3}$$

For lossless, uniform media, the amplitude of the electromagnetic fields at every point in space and time is governed by the electromagnetic wave equation

$$\nabla^2 E_n - \frac{\epsilon^{(L)}\left(\omega_n\right)}{c^2}\frac{\partial^2 E_n}{\partial t^2} = \frac{1}{\epsilon_0 c^2}\frac{\partial^2 P_n^{(\mathrm{NL})}}{\partial t^2}, \tag{2.4}$$

The derivation to obtain the evolution of the optical fields from 2.3 and 2.4 is complicated and was done in detail in [30]. To summarize the calculation, optical fields are decomposed as plane waves given by $E_j(z,t) = A_j(z)e^{i(k_j z - \omega_j t)} + A_j^*(z)e^{-i(k_j z - \omega_j t)}$, where $A_j(z)$ is the field amplitude, k_j is the wave vector, ω_j is the frequency and $j = 1, 2$ are subscripts that denote the fundamental and second harmonic fields. The resulting spatial propagation equations are [23, 30–32]

$$\begin{aligned} \frac{dA_1(z)}{dz} &= 2\alpha A_1(z)^* A_2(z) e^{-i\Delta k z} \\ \frac{dA_2(z)}{dz} &= -\alpha A_1^2(z) e^{i\Delta k z}, \end{aligned} \tag{2.5}$$

Where $A_1(A_2)$ are slowly-varying amplitudes of the Fundamental and Harmonic fields, $\Delta k = 2k_1 - k_2$ is the wave vector mismatch, $\alpha = d_{\mathrm{eff}}\sqrt{\frac{2{\omega_1}^2\omega_2\hbar}{\epsilon_0 c^2 V n_1^2 n_2}}$ is the nonlinear matter electromagnetic field coupling coefficient, V is the mode volume, n_1, n_2 are the refractive indices of the medium at angular frequency ω_1, ω_2, d_{eff} is the effective second order nonlinearity and z is the propagation length through the crystal.

2.3 Generalized Quantum Propagation Equations

2.3.1 Motivation

We are interested in continuous variables of the light field. A complete description of a given quantum state has to take into account its degrees of freedom and for an optical field, some of the important degrees of freedom are photon number, frequency, polarization and phase. When the electromagnetic field is quantized, the procedure followed yields quantized excitation (energy) per field mode called the photon. Degrees of freedom such as phase and amplitude retain their continuous character. However, if we look at variables such as field amplitudes or phase, their spectrum is continuous. Nonetheless, quantization results in unavoidable uncertainties between conjugate variables described by Heisenberg's relations. Is a continuous variable description more useful than a discrete variable description? The usefulness of the theoretical description (representation) depends on the experiment it tries to describe. To be clear, both descriptions are equally valid, describe the same physical reality and one can consistently go back and forth between the two representations. The choice of representation depends on convenience. If say, we have a photon counting experiment, then the logical choice is to use a photon number state basis. On the other hand, if we have intense fields, then such a basis, is not suitable because detectors cannot distinguish between say, 10^{10} and $10^{10}+1$ photons. In this case, it is more suitable to setup an interference experiment and use continuous variables such as field amplitude and phase. The "quantumness" of light, in this case, manifests as the uncertainty of the conjugate amplitude and phase quadrature observables. To re-emphasize, if an unsuitable basis is used, the details of the description may not be experimentally accessible. In our work, we are interested in the uncertainties in the continuous variables of field amplitude and phase and we study how these uncertainties evolve with spatial propagation through the nonlinear medium.

Since we are interested in studying the evolution of quantum fluctuations, we need to extend the earlier classical analysis to the quantum field regime. This has been done in many ways [33–36] and the results are the same as invoking the Bohr correspondence principle, where we just replace the field amplitudes by operators $\hat{A}_j(z)$ where j =1,2 to obtain a quantum picture. The main framework our research builds upon was first established by Ou [31] and by Li [32].

Assuming a lossless system, the field evolution equations 2.5 thus become

$$\begin{aligned} \frac{d\hat{A}_1}{dz} &= 2\alpha \hat{A}_1^{\dagger} \hat{A}_2 e^{-i\Delta kz} \\ \frac{d\hat{A}_2}{dz} &= -\alpha \hat{A}_1^2 e^{i\Delta kz}, \end{aligned} \tag{2.6}$$

The operator equations 2.6 are nonlinear and analytical solutions are possible only if we make an approximation in linearizing them. The standard technique employed based on the so called background field method is to write the total field amplitude as a sum of the mean field amplitude and fluctuations about the mean. The theory also allows us to decouple the fluctuations from the mean field values [37–42].

$$\begin{aligned} \hat{A}_1 &= \langle \hat{A}_1 \rangle \mathbb{1} + \hat{a}_1 \\ \hat{A}_2 &= \langle \hat{A}_2 \rangle \mathbb{1} + \hat{a}_2, \end{aligned} \tag{2.7}$$

We make an approximation by neglecting the terms $\hat{a}_1^{\dagger}\hat{a}_2$ and $\hat{a}_1^2$. This can justified because in an experiment, the mean field amplitudes are much larger than the fluctuations. This approximation is rendered invalid for extremely weak fields i.e. fields with a very low photon number. We make an assumption that the fluctuations between the fundamental and harmonic fields are completely uncorrelated before they interact with the nonlinear medium in SHG. As we will show, it is the nonlinear interaction that generates correlations between the photon statistics of the two optical fields. Later, we will exploit this fact to study the noise performance of our nonlinear interferometer.

2.3.2 Mean Field Solutions

Substituting equations 2.7 in 2.6 we obtain

$$\begin{aligned} \frac{d\langle \hat{A}_1 \rangle}{dz} &= 2\alpha \langle \hat{A}_1^* \rangle \langle \hat{A}_2 \rangle e^{-i\Delta k z} \\ \frac{d\langle \hat{A}_2 \rangle}{dz} &= -\alpha \langle \hat{A}_1 \rangle^2 e^{i\Delta k z}, \end{aligned} \tag{2.8}$$

where $\hat{A}_1, \hat{A}_2$ are the mean field amplitudes of the fundamental and second harmonic fields, z is the propagation length in the medium, α is the nonlinear coupling coefficient and Δk is the wave-vector mismatch.

We now proceed to obtain solutions to the mean field equations 2.8. These solutions were first derived by Amstrong *et.al.,* in 1962 [30] from purely classical considerations. It is easier to solve these coupled equations if we define dimensionless quantities [23, 31, 32]. Using the definitions in table 2.1, we can write,

$$\begin{aligned} A_1 &= a \times u_1 A_{10} e^{i\varphi_1} \\ A_2 &= b \times u_2 A_{10} e^{i\varphi_2} \\ \zeta &= c \times \alpha z A_{10} \\ \Delta s &= d \times \frac{\Delta k}{\alpha A_{10}}, \end{aligned} \tag{2.9}$$

Where a,b,c,d are undetermined real, numerical constants that make the equations 2.8 dimensionless and φ_1, φ_2 are the phases of the fields. Using the definitions in equation 2.9 and setting $\Delta k = 0$ we can re-write 2.8 as

$$\begin{aligned} c\left(\frac{du_1}{d\zeta} + iu_1 \frac{d\varphi_1}{d\zeta}\right) &= 2bu_1 u_2 e^{-i(2\varphi_1 - \varphi_2)} \\ bc\left(\frac{du_2}{d\zeta} + iu_2 \frac{d\varphi_2}{d\zeta}\right) &= -a^2 u_1^2 e^{i(2\varphi_1 - \varphi_2)}, \end{aligned} \tag{2.10}$$

For the above equations to be dimensionless we obtain the conditions $c = 2b, d = c$ and $bc = a^2$. Choosing $a = 1$ we obtain $a = 1, b = \frac{1}{\sqrt{2}}, c = \sqrt{2}, d = \sqrt{2}$.

Table 2.1: Variables used in deriving nonlinear propagation equations.

Normalization variables		
Variable	Description	Value
A_{10}	Initial fundamental field amplitude	$\mid \langle A_1(0) \rangle \mid$
A_{20}	Initial harmonic field amplitude	$\mid \langle A_2(0) \rangle \mid$
A_1	Fundamental field amplitude	$\mid \langle A_1(\zeta) \rangle \mid$
A_2	Harmonic field amplitude	$\mid \langle A_2(\zeta) \rangle \mid$
ζ	Normalized length	$\mid \langle A_2(\zeta) \rangle \mid$
u_1	Normalized fundamental amplitude	$\frac{\mid \langle \hat{A}_1(\zeta) \rangle \mid}{\mid \langle \hat{A}_1(0) \rangle \mid}$
u_2	Normalized harmonic amplitude	$\sqrt{2}\frac{\mid \langle \hat{A}_2(\zeta) \rangle \mid}{\mid \langle \hat{A}_1(0) \rangle \mid}$
Δs	Normalized phase mismatch	$\frac{\Delta k(\zeta)}{\alpha \mid \langle \hat{A}_1(0) \rangle \mid}$

Taking equations 2.10 and equating real and imaginary parts we obtain the propagation equations for the fields and their phases as

$$\boxed{\begin{aligned}\frac{du_1}{d\zeta} &= u_1 u_2 \cos\theta \\ \frac{du_2}{d\zeta} &= -u_1^2 \cos\theta \\ \frac{d\varphi_1}{d\zeta} &= u_2 \sin\theta \\ \frac{d\varphi_2}{d\zeta} &= \frac{u_1^2}{u_2}\sin\theta,\end{aligned}} \tag{2.11}$$

where $\theta(\zeta) = 2\varphi_1(\zeta) - \varphi_2(\zeta)$.

It is useful to look for invariants in these system of equations. This was done in [23, 30] by considering the spatial derivative of $\log u_1^2 u_2$ along with equations 2.12 and the invariant quantity was calculated to be $\Gamma = -u_1^2 u_2 \sin\theta$.

2.3.3 Special Cases

Thus, the mean field equations can be written in a compact form as

$$\frac{du_1}{d\zeta} = u_1 u_2 \cos\theta \tag{2.12}$$

$$\frac{du_2}{d\zeta} = -u_1^2 \cos\theta$$

$$\frac{d\varphi_1}{d\zeta} = \frac{\Gamma}{{u_1}^2} \tag{2.13}$$

$$\frac{d\varphi_2}{d\zeta} = \frac{\Gamma}{{u_2}^2}$$

$$\frac{d\theta}{d\zeta} = (\frac{2}{{u_1}^2} - \frac{1}{{u_2}^2})\Gamma, \tag{2.14}$$

The above equations give us information about the evolution of the amplitudes and phases of the harmonic and fundamental fields as they propagate through the nonlinear medium.

2.3.3.1. Harmonic Generation $\theta = \pi$

Setting $\theta = \pi$ corresponds to the case of SHG and we can obtain the analytical solutions by direct integration as $u_1(\zeta) = \text{sech}\,(\zeta_0 - \zeta), u_2(\zeta) = \tanh(\zeta_0 - \zeta)$. With the initial conditions as $u_1(0) = 1$ and $u_2(0) = 0$ we obtain $u_1(\zeta) = \text{sech}\,(\zeta),\ u_2(\zeta) = \tanh(\zeta)$. The solution to the above special case of $\theta = \pi$ can be plotted graphically as shown in figure 2.2 and is a well known result [23, 30]. We see that eventually all the fundamental is converted into the harmonic.

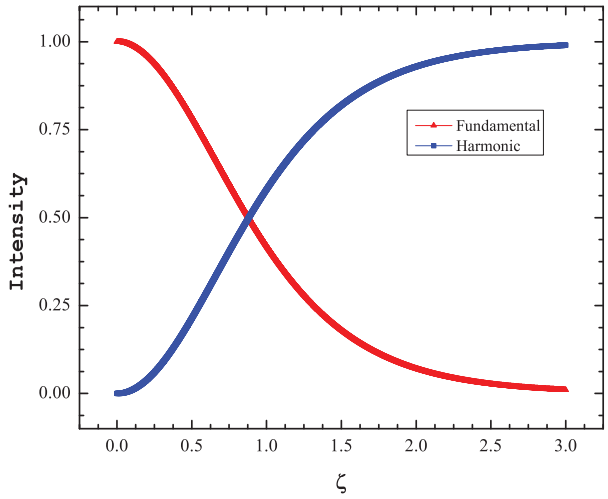

Figure 2.2. Spatial evolution of fundamental (red) and harmonic (blue) intensities in second harmonic generation.

2.3.3.2. Parametric Downconversion $\theta = 0$

Parametric downconversion is the nonlinear process by which a pump photon at frequency ω_0 is destroyed to produce two new photons (called the signal and idler) at frequencies ω_s and ω_i [23]. This process may occur spontaneously with only a pump field as an input, or seeded by the presence of an additional field at some other frequency (usually at the desired signal frequency). In the seeded case, this

externally provided signal field will be amplified, accompanied by the production of an idler beam at an appropriate wavelength. In literature, the common terms one encounters are, optical parametric generator, optical parametric amplifier, parametric oscillator. An optical parametric generator (OPG) is based on the spontaneous parametric downconversion (SPDC) effect described earlier, an optical parametric amplifier amplifies a weak seed beam and optical parametric oscillator configuration is an optical cavity enhanced conversion process, where the nonlinear crystal is placed in an optical cavity.

We can think of parametric amplification/downconversion (PDC) as the reverse process of harmonic generation with the essential difference that in the specific case we are interested in, both fundamental and harmonic field injection is necessary. In PDC, the harmonic is strong and the fundamental serves as a weak seed. As the fields interact with the medium, the harmonic gets depleted and the fundamental gets amplified. The necessary phase condition for a normal parametric down-conversion process is $\theta = 0$. An important point to note is that PDC occurs as long as the initial phase condition is satisfied. The phases of both fields evolve as the propagate through the medium and once they attain $\theta = 0$, the interaction reverts back to harmonic generation as in figure 2.3.

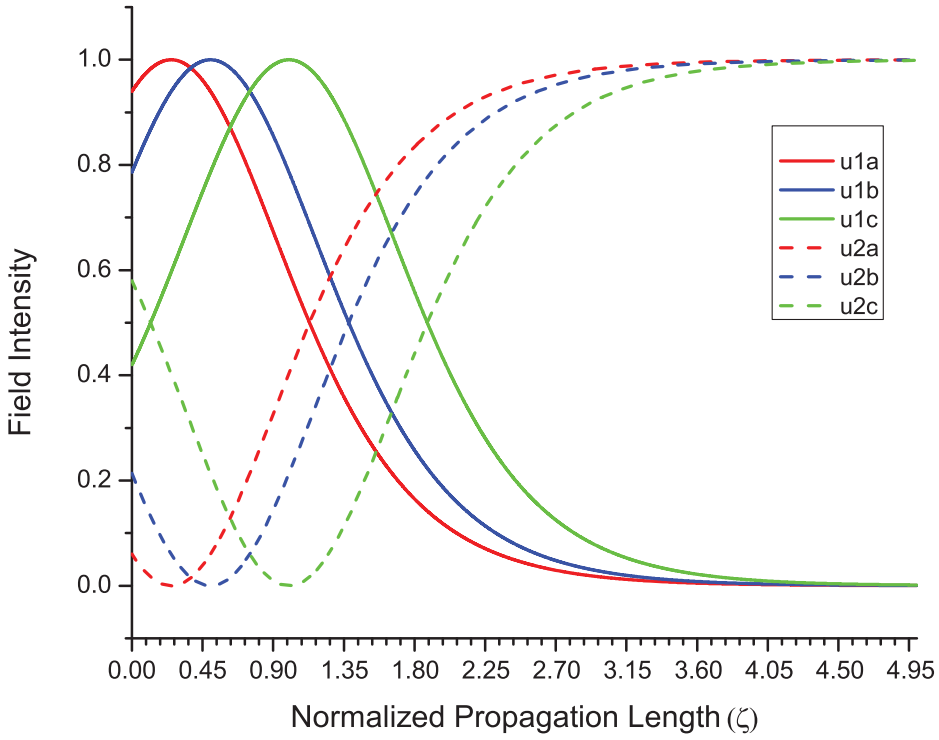

Figure 2.3. Spatial evolution of fundamental and harmonic fields for different input intensities with $\theta = 0$.

2.4 Quantum Fluctuations

2.4.1 Quadrature Representation

Field quadratures are related to the amplitude and phase properties of light. In the quantum description, they correspond to position and momentum of a simple harmonic oscillator and constitute an infinite dimensional Hilbert space. Our main interest is to work with intense optical fields (also known as a *bright* field). As discussed earlier, measurements with photodetectors have limited resolution, which means they are not capable of distinguishing between individual photon numbers, therefore it is customary to decompose the field operator for large field amplitudes into a "classical" displacement and a quantum operator and we will see later that in the limit of sufficiently large classical field amplitudes, the generated photocurrents yield direct information about the amplitude quadrature, while the uncertainty about the orthogonal phase quadrature cannot be seen. In direct detection, the bright beam carries its own local oscillator and thus intrinsically determines a fixed phase difference. However, direct detection lacks any information about the phase quadrature. We will explore this in more detail in the next chapter of this thesis.

2.4.1.1. Classical Field Quadratures

In an experiment, we measure the intensity of light and this measurement yields a real number as a result. In general, from a classical point of view we can describe a monochromatic sinusoidal electric field as a sum of two complex quantities $E(t) = \frac{1}{2}(a(t) + a^*(t))$, where $a(t)$ is a complex quantity that can be written as $a(t) = ae^{-i\omega t}$, where a the time independent, complex amplitude. Writing the amplitude as $a = x + iy$, the electric field can be written as

$$E(t) = x\cos\omega t + y\sin\omega t \tag{2.15}$$

x and y are called quadrature components because they are orthogonal to each other.

2.4.1.2. Quadrature Representation of Quantum Fields

The same formalism can be used for quantum operators. Annihilation and creation operators are non-Hermitian so they are not observables. When related to experiments, the real part of the field operator $\hat{a}_j$ has information about the photon number while the imaginary part can be related to the phase. Our goal is to study the fluctuations of these two parameters (of which, photon number fluctuations are direct observables). Therefore, we define a new set of Hermitian operators called the field quadrature operators, $\hat{x}_j$ and $\hat{y}_j$, where φ_j (j=1,2) is the phase of the fundamental and harmonic fields respectively.

$$\begin{aligned}\hat{x}_j &= \frac{\hat{a}_j e^{-\mathrm{i}\varphi_j} + \hat{a}_j^\dagger e^{\mathrm{i}\varphi_j}}{2},\\ \hat{y}_j &= \frac{\hat{a}_j e^{-\mathrm{i}\varphi_j} - \hat{a}_j^\dagger e^{\mathrm{i}\varphi_j}}{2i},\end{aligned} \tag{2.16}$$

We define the following correlation relationships between the quadrature operators based on the assumption that before the interaction with the nonlinear medium, the fields are just vacuum

$$\begin{aligned}\langle\hat{x}_i(0)\hat{x}_j(0)\rangle = \langle\hat{y}_i(0)\hat{y}_j(0)\rangle &= \frac{1}{4}\delta_{\mathrm{ij}}\\ \langle\hat{x}_i(0)\hat{y}_j(0)\rangle = \langle\hat{y}_i(0)\hat{x}_j(0)\rangle &= 0\\ \langle\hat{x}_i(0)\hat{y}_i(0)\rangle + \langle\hat{x}_j(0)\hat{y}_j(0)\rangle &= 0,\end{aligned} \tag{2.17}$$

From equations 2.6, 2.7

$$\frac{d\hat{a}_1}{dz} = 2\alpha\left\{\hat{a}_1^{\dagger}A_2 + A_1^{*}\hat{a}_2\right\} \tag{2.18}$$
$$\frac{d\hat{a}_2}{dz} = -2\alpha\hat{a}_1 A_1,$$

Substituting equations 2.16 in 2.18 we get

$$\frac{d}{\mathrm{d}\zeta}\left\{(\hat{x}_1 + i\hat{y}_1)\,e^{\mathrm{i}\varphi_1}\right\} = u_2\,(\hat{x}_1 - i\hat{y}_1)\,e^{-\mathrm{i}\varphi_1}e^{\mathrm{i}\varphi_2} + \sqrt{2}u_1\,(\hat{x}_2 + i\hat{y}_2)\,e^{-\mathrm{i}\varphi_1}e^{\mathrm{i}\varphi_2},$$

$$\frac{d\hat{x}_1}{\mathrm{d}\zeta} + i\hat{x}_1\frac{\mathrm{d}\varphi_1}{\mathrm{d}\zeta} + i\frac{d\hat{y}_1}{\mathrm{d}\zeta} - \hat{y}_1\frac{\mathrm{d}\varphi_1}{\mathrm{d}\zeta} = u_2\,(\hat{x}_1 - i\hat{y}_1)\,e^{-i(2\varphi_1-\varphi_2)} + \sqrt{2}u_1\,(\hat{x}_2 + i\hat{y}_2)\,e^{-i(2\varphi_1-\varphi_2)}$$

Using $\theta = 2\varphi_1 - \varphi_2$ and $\dfrac{\mathrm{d}\varphi_1}{\mathrm{d}\zeta} = \dfrac{\Gamma}{u_1^2}$ we get

$$\frac{d\hat{x}_1}{\mathrm{d}\zeta} + i\hat{x}_1\frac{\Gamma}{u_1^2} + i\frac{d\hat{y}_1}{\mathrm{d}\zeta} - \hat{y}_1\frac{\Gamma}{u_1^2} = u_2\,(\hat{x}_1 - i\hat{y}_1)\,e^{-\mathrm{i}\theta} + \sqrt{2}u_1\,(\hat{x}_2 + i\hat{y}_2)\,e^{-\mathrm{i}\theta},$$

Using the expansion $e^{i\theta} = \cos\theta + i\sin\theta$, equating real and imaginary parts we have

$$\frac{d\hat{x}_1}{\mathrm{d}\zeta} = u_2\hat{x}_1\mathrm{cos}\theta - \hat{y}_1\left(u_2\mathrm{sin}\theta - \frac{\Gamma}{u_1^2}\right) + \sqrt{2}u_1\hat{x}_2\mathrm{cos}\theta + \sqrt{2}u_1\hat{y}_2\mathrm{sin}\theta, \tag{2.19}$$

$$\frac{d\hat{y}_1}{\mathrm{d}\zeta} = \left(u_2\mathrm{sin}\theta - \frac{\Gamma}{u_1^2}\right)\hat{x}_1 - u_2\hat{y}_1\mathrm{cos}\theta - \sqrt{2}u_1\hat{x}_2\mathrm{sin}\theta + \sqrt{2}u_1\hat{y}_2\mathrm{cos}\theta, \tag{2.20}$$

Likewise, for the harmonic equating real and imaginary parts for the resultants gives us

$$\frac{d\hat{x}_2}{\mathrm{d}\zeta} = -\sqrt{2}u_1\hat{x}_1\mathrm{cos}\theta + \sqrt{2}u_1\hat{y}_1\mathrm{sin}\theta + \hat{y}_2\frac{\Gamma}{u_2^2} \tag{2.21}$$

$$\frac{d\hat{y}_2}{\mathrm{d}\zeta} = -\sqrt{2}u_1\hat{x}_1\mathrm{sin}\theta - \sqrt{2}u_1\hat{y}_1\mathrm{cos}\theta + \hat{x}_2\frac{\Gamma}{u_2^2}, \tag{2.22}$$

2.4.1.3. Harmonic Generation

The case of $\theta = \pi$ describes harmonic generation where $u_1(0) = 1$, $u_2(0) = 0$, $\Gamma = 0$ hence the quadrature fluctuation equations simplify as

$$\boxed{\begin{aligned} \frac{d\hat{x}_1}{d\zeta} &= -u_2\hat{x}_1 - \sqrt{2}u_1\hat{x}_2 \\ \frac{d\hat{y}_1}{d\zeta} &= u_2\hat{y}_1 - \sqrt{2}u_1\hat{y}_2 \\ \frac{d\hat{x}_2}{d\zeta} &= \sqrt{2}u_1\hat{x}_1 \\ \frac{d\hat{y}_2}{d\zeta} &= \sqrt{2}u_1\hat{y}_1, \end{aligned}} \tag{2.23}$$

2.4.1.4. Parametric Downconversion

The case of $\theta = 0$ describes parametric downconversion where $u_1(0) = \epsilon$ (ϵ is a small number), $u_2(0) = 1$, $\Gamma = 0$ and the quadrature fluctuation equations simplify as

$$\boxed{\begin{aligned} \frac{d\hat{x}_1}{d\zeta} &= u_2\hat{x}_1 + \sqrt{2}u_1\hat{x}_2 \\ \frac{d\hat{y}_1}{d\zeta} &= -u_2\hat{y}_1 + \sqrt{2}u_1\hat{y}_2 \\ \frac{d\hat{x}_2}{d\zeta} &= -\sqrt{2}u_1\hat{x}_1 \\ \frac{d\hat{y}_2}{d\zeta} &= -\sqrt{2}u_1\hat{y}_1, \end{aligned}} \tag{2.24}$$

Equations 2.23, 2.24 are linear in $\hat{x}_i, \hat{y}_i$ and were first derived by Ou [31] and Li [32]. These equations describe the spatial propagation of quadrature components of the quantum fluctuations. Note that there are no cross terms in the differential equations and can be solved analytically.

2.4.2 Numerical Solutions to the Evolution Equations

The solution to the operator equation 2.23 can be obtained in terms of the evolution of the coefficients. We can organize these equations in a matrix form as shown below

$$\frac{d}{d\zeta}\begin{pmatrix}\hat{x}_1\\ \hat{y}_1\\ \hat{x}_2\\ \hat{y}_2\end{pmatrix} = \begin{pmatrix}-u_2 & 0 & -\sqrt{2}u_1 & 0\\ 0 & u_2 & 0 & -\sqrt{2}u_1\\ \sqrt{2}u_1 & 0 & 0 & 0\\ 0 & \sqrt{2}u_1 & 0 & 0\end{pmatrix}\begin{pmatrix}\hat{x}_1\\ \hat{y}_1\\ \hat{x}_2\\ \hat{y}_2\end{pmatrix}, \tag{2.25}$$

Next, we obtain solutions to the coupled system by using the fact that the solution to any linear differential equation can be expressed as a linear combination of the initial conditions. We can write the solutions in Matrix form as

$$\begin{pmatrix}\hat{x}_1(\zeta)\\ \hat{y}_1(\zeta)\\ \hat{x}_2(\zeta)\\ \hat{y}_2(\zeta)\end{pmatrix} = \begin{pmatrix}c_{11}(\zeta) & c_{12}(\zeta) & c_{13}(\zeta) & c_{14}(\zeta)\\ c_{21}(\zeta) & c_{22}(\zeta) & c_{23}(\zeta) & c_{24}(\zeta)\\ c_{31}(\zeta) & c_{32}(\zeta) & c_{33}(\zeta) & c_{34}(\zeta)\\ c_{41}(\zeta) & c_{42}(\zeta) & c_{43}(\zeta) & c_{44}(\zeta)\end{pmatrix}\begin{pmatrix}\hat{x}_1(0)\\ \hat{y}_1(0)\\ \hat{x}_2(0)\\ \hat{y}_2(0)\end{pmatrix}, \tag{2.26}$$

Substituting equation 2.26 in 2.25 we end up with

$$\frac{d}{d\zeta}\begin{pmatrix}c_{11} & c_{12} & c_{13} & c_{14}\\ c_{21} & c_{22} & c_{23} & c_{24}\\ c_{31} & c_{32} & c_{33} & c_{34}\\ c_{41} & c_{42} & c_{43} & c_{44}\end{pmatrix} =$$

$$\begin{pmatrix}-\sqrt{2}c_{31}u_1 - c_{11}u_2 & -\sqrt{2}c_{32}u_1 - c_{12}u_2 & -\sqrt{2}c_{33}u_1 - c_{13}u_2 & -\sqrt{2}c_{34}u_1 - c_{14}u_2\\ -\sqrt{2}c_{41}u_1 + c_{21}u_2 & -\sqrt{2}c_{42}u_1 + c_{22}u_2 & -\sqrt{2}c_{43}u_1 + c_{23}u_2 & -\sqrt{2}c_{44}u_1 + c_{24}u_2\\ \sqrt{2}c_{11}u_1 & \sqrt{2}c_{12}u_1 & \sqrt{2}c_{13}u_1 & \sqrt{2}c_{14}u_1\\ \sqrt{2}c_{21}u_1 & \sqrt{2}c_{22}u_1 & \sqrt{2}c_{23}u_1 & \sqrt{2}c_{24}u_1\end{pmatrix} \tag{2.27}$$

Note that u_i and c_{ij} are functions of the normalized propagation length ζ.

2.5 Squeezing

In the preceding section, we have derived the evolution of quadratures. The question is, how can we experimentally quantify any changes that have occurred to the light? Since we established earlier that fluctuations are directly related to measurement precision, it is logical to investigate the variances of the quadrature operators. This is encapsulated by the paradigm of *"squeezing"*. Light is said to be squeezed if the variance of a certain field quadrature falls below the level of vacuum state fluctuations. Following [31], [32] we define squeezing as the ratio of the average variance at propagation lengths ζ and 0. Values of $Sx, Sy < 1$ indicate a decrease in fluctuations or *"squeezing"* in uncertainty in a quadrature, while $Sx, Sy > 1$ would indicate an increase in fluctuation or *"de-squeezing"*.

$$S_{1x} \equiv \frac{\langle \hat{x}_1(\zeta)^2 \rangle}{\langle \hat{x_1}(0)^2 \rangle},\ S_{1y} \equiv \frac{\langle \hat{y}_1(\zeta)^2 \rangle}{\langle \hat{y_1}(0)^2 \rangle}$$

$$S_{2x} \equiv \frac{\langle \hat{x}_2(\zeta)^2 \rangle}{\langle \hat{x_2}(0)^2 \rangle},\ S_{2y} \equiv \frac{\langle \hat{y}_2(\zeta)^2 \rangle}{\langle \hat{y_2}(0)^2 \rangle}, \tag{2.28}$$

Making use of the correlation properties of the quadrature operators given in equation 2.17 that describes the spatial evolution of the quadratures the variances can be organized as

$$\begin{pmatrix} \hat{x}_1^2(\zeta) \\ \hat{y}_1^2(\zeta) \\ \hat{x}_2^2(\zeta) \\ \hat{y}_2^2(\zeta) \end{pmatrix} = \begin{pmatrix} c_{11}^2\hat{x}_1^2(0) + 2c_{11}c_{13}\hat{x}_1(0)\hat{x}_2(0) + c_{13}^2\hat{x}_2^2(0) + c_{12}^2\hat{y}_1^2(0) + 2c_{12}c_{14}\hat{y}_1(0)\hat{y}_2(0) + c_{14}^2\hat{y}_2^2(0) \\ c_{21}^2\hat{x}_1^2(0) + 2c_{21}c_{23}\hat{x}_1(0)\hat{x}_2(0) + c_{23}^2\hat{x}_2^2(0) + c_{22}^2\hat{y}_1^2(0) + 2c_{22}c_{24}\hat{y}_1(0)\hat{y}_2(0) + c_{24}^2\hat{y}_2^2(0) \\ c_{31}^2\hat{x}_1^2(0) + 2c_{31}c_{33}\hat{x}_1(0)\hat{x}_2(0) + c_{33}^2\hat{x}_2^2(0) + c_{32}^2\hat{y}_1^2(0) + 2c_{32}c_{34}\hat{y}_1(0)\hat{y}_2(0) + c_{34}^2\hat{y}_2^2(0) \\ c_{41}^2\hat{x}_1^2(0) + 2c_{41}c_{43}\hat{x}_1(0)\hat{x}_2(0) + c_{43}^2\hat{x}_2^2(0) + c_{42}^2\hat{y}_1^2(0) + 2c_{42}c_{44}\hat{y}_1(0)\hat{y}_2(0) + c_{44}^2\hat{y}_2^2(0) \end{pmatrix}$$

$$\begin{pmatrix} \hat{x}_1^2(\zeta) \\ \hat{y}_1^2(\zeta) \\ \hat{x}_2^2(\zeta) \\ \hat{y}_2^2(\zeta) \end{pmatrix} = \frac{1}{4}\begin{pmatrix} c_{11}^2 + c_{12}^2 + c_{13}^2 + c_{14}^2 \\ c_{21}^2 + c_{22}^2 + c_{23}^2 + c_{24}^2 \\ c_{31}^2 + c_{32}^2 + c_{33}^2 + c_{34}^2 \\ c_{41}^2 + c_{42}^2 + c_{43}^2 + c_{44}^2 \end{pmatrix}, \tag{2.29}$$

Using the definition of the squeezing function given in equation 2.28

$$\begin{pmatrix} S_{x1} \\ S_{y1} \\ S_{x2} \\ S_{y2} \end{pmatrix} = \begin{pmatrix} c_{11}^2 + c_{12}^2 + c_{13}^2 + c_{14}^2 \\ c_{21}^2 + c_{22}^2 + c_{23}^2 + c_{24}^2 \\ c_{31}^2 + c_{32}^2 + c_{33}^2 + c_{34}^2 \\ c_{41}^2 + c_{42}^2 + c_{43}^2 + c_{44}^2 \end{pmatrix}, \tag{2.30}$$

2.5.1 Squeezing in Harmonic Generation

We numerically solve equation 2.4.2 for c_{ij}'s and plot the results for squeezing of both optical fields as a function of ζ as shown in figure 2.4. The values of Sx, Sy give us information about the fluctuations in photon number and phase fluctuations respectively. Assuming a coherent state input for the fundamental field, we can see that the amplitude fluctuations in the fundamental field can be suppressed to an arbitrarily small value, while for the harmonic field, at best 50% squeezing of amplitude fluctuations is possible. These results were first obtained by Ou [31].

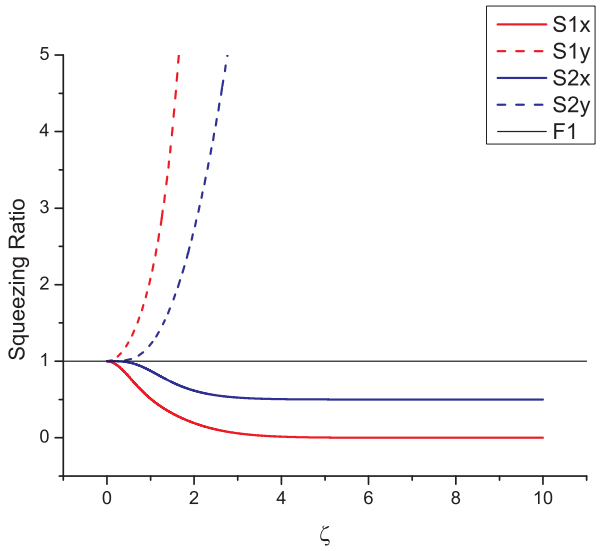

Figure 2.4. Spatial evolution of fundamental and harmonic squeezing.

2.5.2 Squeezing in Parametric Downconversion

Inspecting the linear differential equations 2.24, we can clearly expect a smooth reversal in behavior when compared with the SHG case. So if we place back to back SHG and PDC stages, the fluctuations should go back to the vacuum state after interacting with the same characteristic length of the medium. The equations are numerically evaluated and the results are plotted as shown in figure 2.5

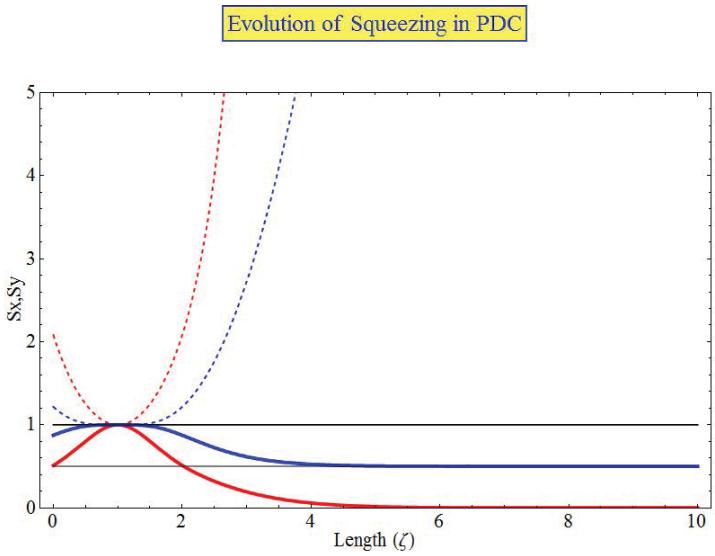

Figure 2.5. Fundamental quadrature squeezing is given by the red curves and harmonic quadrature squeezing is given by the blue curves. Solid curves are the x quadrature and dotted curves are the y quadrature. The normalized length of the crystal is $\zeta_0 = 1$.

3. NONLINEAR INTERFEROMETER ANALYSIS

3.1 Nonlinear Interferometer Setup

In the previous chapter, we discussed the evolution of mean fields and fluctuations in specific cases of harmonic generation and parametric downconversion. In this chapter, we investigate the physics of the system for a more general case of an arbitrary phase difference between the optical fields, parameterized by the variable δ.

From chapter 1, the basic construction of a nonlinear interferometer can be depicted as shown in the figure 3.1. The nonlinear interferometer setup consists of two nonlinear crystals which serve as field splitter and combiner (SHG/PDC).[1] We will see later that the same unitary evolution formalism that was used to describe a linear interferometer can be applied to our system. Each crystal has two inputs and and two outputs. In the SHG stage, a strong, coherent IR laser (u_{10}) serves as the pump (fundamental). There is no harmonic input, just vacuum modes that couple into the system through this port. The nonlinear process of second harmonic generation creates entanglement between the pump field and the vacuum field [26, 43] akin to a linear beamsplitter with the important difference that in a nonlinear process, new fields are generated and this manifests as a squeezed coherent output at the end of the SHG stage. The fundamental intensity decreases as it is converted to a harmonic field and as we saw in the previous chapter, both fields are squeezed. The phase shifted fundamental and the harmonic fields are then superposed on the second crystal. We address the question of how the fluctuations evolve if we change the external phase δ between the depleted fundamental and the generated harmonic. From the previous chapter, we saw that both the fundamental and harmonic fields are intensity

[1] In a linear interferometer these elements would be glass beamsplitters.

squeezed. Our proposal is a form of squeezed state enhanced interferometry suggested by Caves [10, 44] and the second stage of our interferometer accomplishes just that with the important advantage of the phase sensing field being amplified.

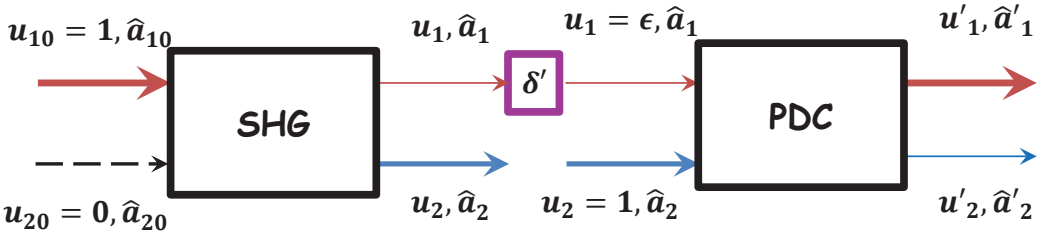

Figure 3.1. Introduction of a controllable phase delay δ' at the PDC stage. Note that the initial conditions are set by the SHG stage.

3.2 Mean Field Solutions For Arbitrary Phase

We shift the phase of the fundamental by $\delta/2$ such that the, the mean field propagation equations are modified as follows

$$\boxed{\begin{aligned} \frac{du_1}{d\zeta} &= u_1 u_2 \cos(\theta + \delta) \\ \frac{du_2}{d\zeta} &= -u_1^2 \cos(\theta + \delta) \\ \frac{d\varphi_1}{d\zeta} &= \frac{\Gamma(\delta)}{{u_1}^2} \\ \frac{d\varphi_2}{d\zeta} &= \frac{\Gamma(\delta)}{{u_2}^2} \\ \frac{d\theta}{d\zeta} &= (\frac{2}{{u_1}^2} - \frac{1}{{u_2}^2})\Gamma(\delta) \\ \Gamma(\delta) &= -u_{10}^2 u_{20} \sin\delta, \end{aligned}} \tag{3.1}$$

Γ is still an invariant, but unlike the special cases where $\Gamma = 0$, we have a non-zero value here which renders the system of equations analytically unsolvable. Hence

we resort to a numerical solution[2]. In the simulation, we vary $\delta \epsilon [0, 2\pi]$ and report how the field amplitudes, optical phases evolve as a function of δ and their spatial evolution over the interaction length.

3.2.1 Mean Field Simulation Results

3.2.1.1. Amplitude and Phase Evolution

We claimed that a nonlinear interferometer not only suppresses quantum fluctuations, but also amplifies the phase sensing signal (u_1). Figures 3.2, 3.3 show the phase sensing field at the output of the second stage of the interferometer. From the analysis of propagation of quantum fluctuations in harmonic generation, we saw that squeezing of the fundamental was directly proportional to the interaction length of the nonlinear crystal. However, the penalty incurred was in terms of the decreased amplitude of the phase sensing field. In any measurement scheme, we would like the measuring device to not influence or taint the measurement itself. While this may not be possible, we minimize the possibility by using a weak phase sensing field. So, the fact that the phase sensing field is weak is not the problem, the problem lies in the recovery of information imprinted on the phase sensing field. The second stage of the nonlinear interferometer alleviates this problem by amplifying the phase sensing field. Figures 3.2, 3.3 show this for two specific lengths $\zeta_0 = 0.5$ and $\zeta_0 = 3.0$. Hence the second stage does indeed act as an amplifier and it is possible to obtain a full recovery of the phase sensing signal. We plot the fundamental field amplitude u_1 as a function of propagation length for different values of δ. It can be seen that conversion from harmonic to fundamental depends critically on the relative phase between the fields. We can use the special case of $\delta = 0$ as our reference. As the phase is tuned, conversion from harmonic to fundamental first decreases and then begins to recover as δ approaches 2π.

[2]C++ and Mathematica code can be found in the appendices

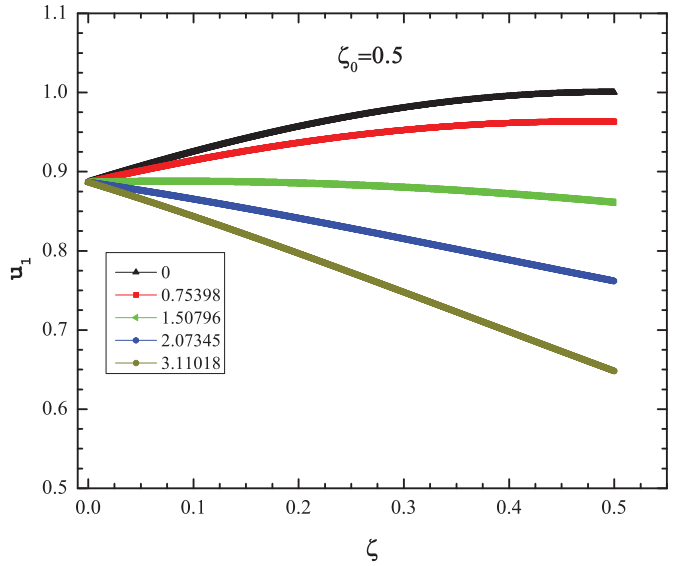

Figure 3.2. Colors represent u_1 for different δ, the values of which are given in the legend for $\zeta_0 = 0.5$.

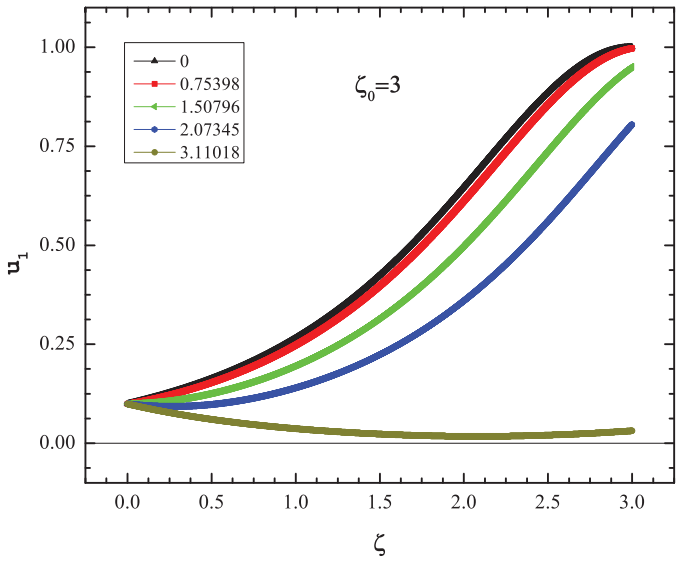

Figure 3.3. Colors represent the fundamental field amplitude, u_1 for different δ, values for which are given in the legend for $\zeta_0 = 3$.

In an interferometer sensitivity to phase is of paramount importance. With this in mind, we can look at data for variation of optical phase with interaction length for different values of δ. In figure 3.4 we plot the optical phase of the fundamental as a function of normalized interaction length. When we compare interaction lengths of $\zeta_0 = 0.5$ in figure 3.4 and $\zeta_0 = 3$ in figure 3.5 we notice that the behavior of φ_1 is dramatically different for $\delta = 3.11$, where the phase decreases more rapidly.

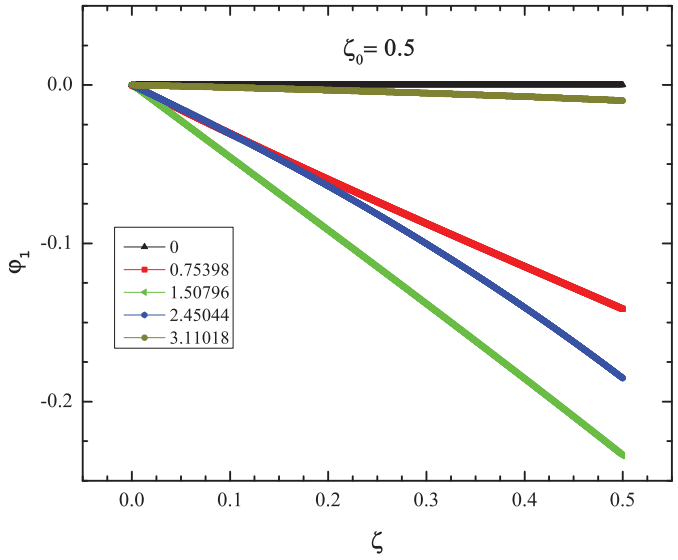

Figure 3.4. Colors represent φ_1 for different δ, whose values are given in the legend at $\zeta_0 = 0.5$.

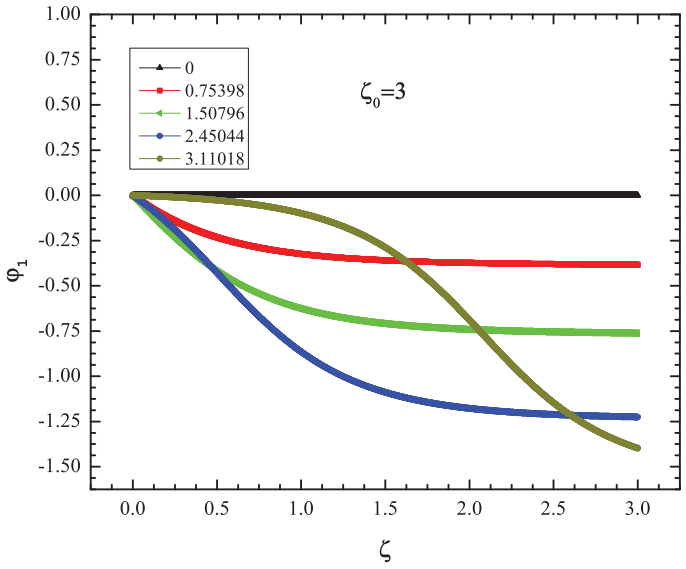

Figure 3.5. Colors represent φ_1 for different δ at $\zeta_0 = 3$.

3.2.1.2. Interferometer Fringes

As discussed earlier, the output of an interferometer is an intensity that follows the phase difference between the fields in its arms. Usually, the phase is such that the intensity is periodic. In a linear interferometer, the output has the same frequency as the input light. In a nonlinear interferometer, new optical fields are generated and the phase dependence manifests as oscillations in both the fundamental and harmonic fields as shown in figures 3.8 and 3.9.

Visibility, defined as $\mathcal{V} = (I_{max} - I_{min})/(I_{max} + I_{min})$ is close to unity when $I_{max} \gg I_{min}$. From table 3.1 and figure 3.6 we can see that it is indeed possible to attain maximum visibility with a nonlinear interferometer, contingent on the fact that the visibility does vary with the interaction length. So in this respect, both the linear and nonlinear interferometers behave identically. For better phase sensitivity, it is desirable to operate the interferometer in the region of maximum slope of the intensity phase graph. In a nonlinear interferometer, there is enhancement of the phase sensing signal, so it is possible to obtain a steeper slope, which translates to a better discrimination of phase. For $\zeta_0 = 0.5$, the slope is small because full conversion from harmonic to fundamental has not occurred. From figure 3.7, we see that the slope increases with increasing interaction length. The slope saturates at about $\zeta_0 = 2$, which means the sensitivity of the interferometer based on the steepness of the slope does not show dramatic improvements for longer normalized lengths ζ_0.

Table 3.1: Slope and visibility of the interferometer fringe.

Slope and visibility				
ζ	m	I_{max}	I_{min}	$\mathcal{V}$
0.5	0.29088	1.0	0.41997	0.41
0.75	0.42475	1.0	0.18071	0.69
1.0	0.52722	1.0	0.0765	0.0.87
1.25	0.61634	1.0	0.02659	0.94
1.50	0.68607	1.0	0.00987	0.98
1.75	0.7347	1.0	0.00364	0.992
2.0	0.76597	1.0	0.00134	0.997
3.0	0.80296	1.0	0.00098	0.998

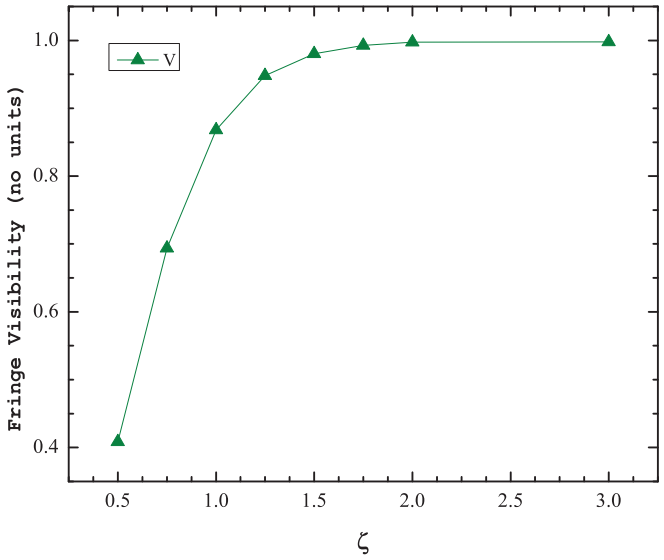

Figure 3.6. Fringe visibility as a function of normalized propagation length ζ_0.

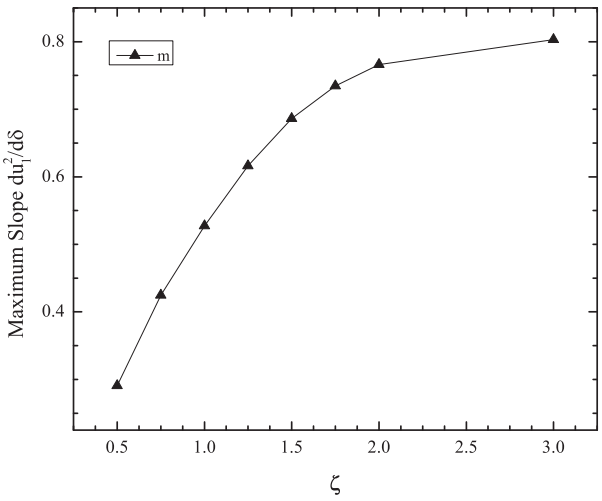

Figure 3.7. Maximum slope of the interference fringe for different normalized propagation lengths ζ_0.

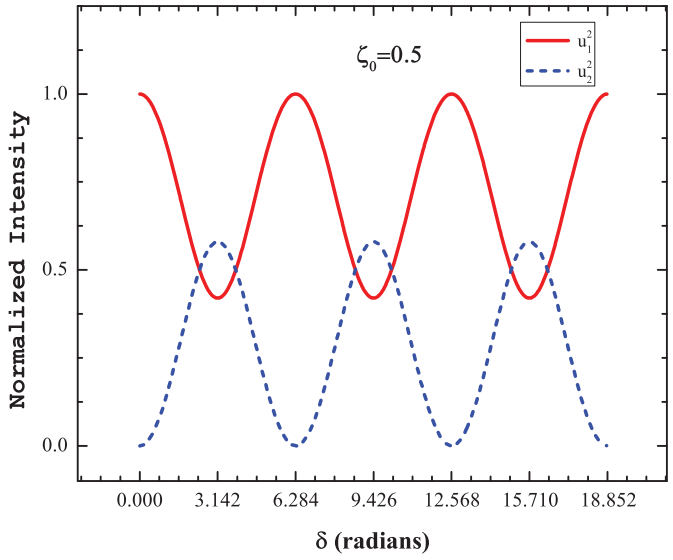

Figure 3.8. Interferometer fringes for $\zeta_0 = 0.5$. Complete conversion from harmonic to fundamental is not achieved.

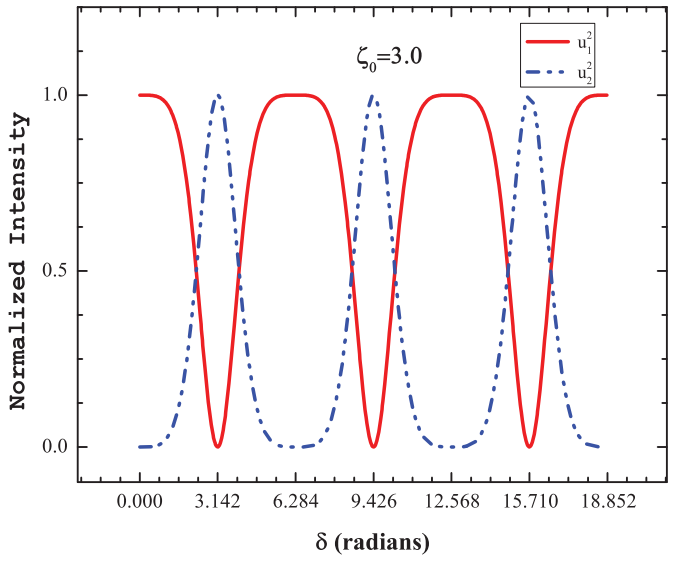

Figure 3.9. Interferometer fringes for $\zeta_0 = 3.0$. Note that there is some saturation of intensity.

3.2.1.3. Variation of Phase φ_1 with δ

Next, we look at the variation of the mean field phase of the fundamental with δ. From figure 3.10 the propagation length increases, the phase plot becomes more linear and its slope increases.

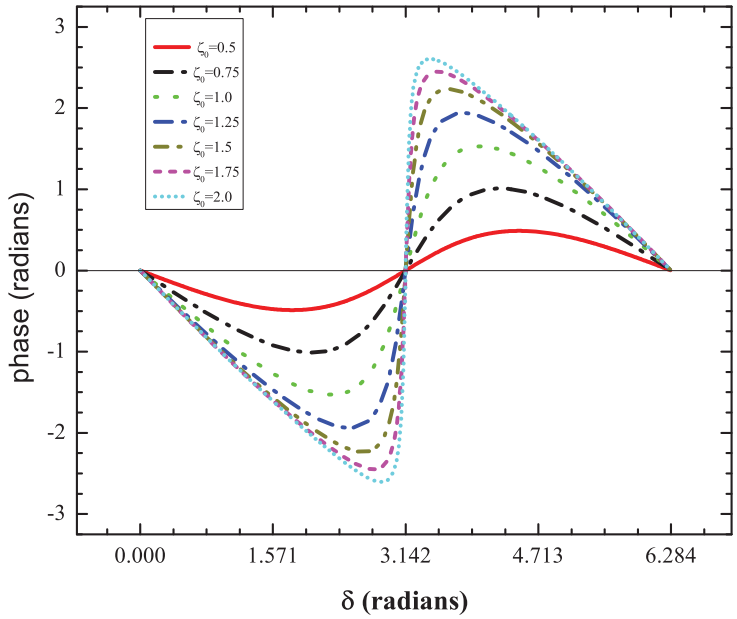

Figure 3.10. Variation of fundamental phase φ_1 as a function of interferometer phase δ for different characteristic lengths ζ_0.

3.3 Propagation of Quantum Fluctuations

3.3.1 Solutions for Arbitrary Phase

In the previous section, we studied the evolution of the mean field. In this section, we investigate the propagation of quantum fluctuations. Using the output of quantum fluctuations for $\zeta = \zeta_0$ from the previous section, we can study the evolution of

quantum fluctuations at $\zeta = 2\zeta_0$. After the fields propagate by ζ_0 their amplitude fluctuations are squeezed and serve to seed further evolution. But the difference is that our control of the relative phase between the mean fields governs the subsequent evolution of the quadrature fluctuations from ζ_0 to $2\zeta_0$ To do so, we take the generalized form of equation 2.4.2 which can be written as

$$\frac{d}{\mathrm{d}\zeta}\begin{pmatrix}\hat{x}_1\\ \hat{y}_1\\ \hat{x}_2\\ \hat{y}_2\end{pmatrix} = M\begin{pmatrix}\hat{x}_1\\ \hat{y}_1\\ \hat{x}_2\\ \hat{y}_2\end{pmatrix} \tag{3.2}$$

$$M = \begin{pmatrix} u_2\cos\theta & \left(\frac{\Gamma}{u_1^2} - u_2\sin\theta\right) & \sqrt{2}u_1\cos\theta & \sqrt{2}u_1\sin\theta \\ -u_2\sin\theta - \frac{\Gamma}{u_1^2} & -u_2\cos\theta & -\sqrt{2}u_1\sin\theta & \sqrt{2}u_1\cos\theta \\ -\sqrt{2}u_1\cos\theta & \sqrt{2}u_1\sin\theta & 0 & \frac{\Gamma}{u_2^2} \\ -\sqrt{2}u_1\sin\theta & -\sqrt{2}u_1\cos\theta & \frac{-\Gamma}{u_2^2} & 0 \end{pmatrix}, \tag{3.3}$$

Following the same arguments that lead to equation (2.26) outlined in section 2.4.2 we obtain the evolution of quantum fluctuations explicitly given by

$$\begin{pmatrix} \sqrt{2}d_{31}\cos(\theta+\delta)u_1 + \sqrt{2}d_{41}\sin(\theta+\delta)u_1 + d_{11}\cos(\theta+\delta)u_2 + d_{21}\left(\frac{\Gamma}{u_1^2} - \sin(\theta+\delta)u_2\right) \\ \sqrt{2}d_{41}\cos(\theta+\delta)u_1 - \sqrt{2}d_{31}\sin(\theta+\delta)u_1 - d_{21}\cos(\theta+\delta)u_2 + d_{11}\left(-\frac{\Gamma}{u_1^2} - \sin(\theta+\delta)u_2\right) \\ -\sqrt{2}d_{11}\cos(\theta+\delta)u_1 + \sqrt{2}d_{21}\sin(\theta+\delta)u_1 + \frac{d_{41}\Gamma}{u_2^2} \\ -\sqrt{2}d_{21}\cos(\theta+\delta)u_1 - \sqrt{2}d_{11}\sin(\theta+\delta)u_1 - \frac{d_{31}\Gamma}{u_2^2} \end{pmatrix}$$

$$\begin{pmatrix} \sqrt{2}d_{32}\cos(\theta+\delta)u_1 + \sqrt{2}d_{42}\sin(\theta+\delta)u_1 + d_{12}\cos(\theta+\delta)u_2 + d_{22}\left(\frac{\Gamma}{u_1^2} - \sin(\theta+\delta)u_2\right) \\ \sqrt{2}d_{42}\cos(\theta+\delta)u_1 - \sqrt{2}d_{32}\sin(\theta+\delta)u_1 - d_{22}\cos(\theta+\delta)u_2 + d_{12}\left(-\frac{\Gamma}{u_1^2} - \sin(\theta+\delta)u_2\right) \\ -\sqrt{2}d_{12}\cos(\theta+\delta)u_1 + \sqrt{2}d_{22}\sin(\theta+\delta)u_1 + \frac{d_{42}\Gamma}{u_2^2} \\ -\sqrt{2}d_{22}\cos(\theta+\delta)u_1 - \sqrt{2}d_{12}\sin(\theta+\delta)u_1 - \frac{d_{32}\,\Gamma}{u_2^2} \end{pmatrix}$$

$$\begin{pmatrix} \sqrt{2}d_{33}\cos(\theta+\delta)u_1 + \sqrt{2}d_{43}\sin(\theta+\delta)u_1 + d_{13}\cos(\theta+\delta)u_2 + d_{23}\left(\frac{\Gamma}{u_1^2} - \sin(\theta+\delta)u_2\right) \\ \sqrt{2}d_{43}\cos(\theta+\delta)u_1 - \sqrt{2}d_{33}\sin(\theta+\delta)u_1 - d_{23}\cos(\theta+\delta)u_2 + d_{13}\left(-\frac{\Gamma}{u_1^2} - \sin(\theta+\delta)u_2\right) \\ -\sqrt{2}d_{13}\cos(\theta+\delta)u_1 + \sqrt{2}d_{23}\sin(\theta+\delta)u_1 + \frac{d_{43}\Gamma}{u_2^2} \\ -\sqrt{2}d_{23}\cos(\theta+\delta)u_1 - \sqrt{2}d_{13}\sin(\theta+\delta)u_1 - \frac{d_{33}\Gamma}{u_2^2} \end{pmatrix}$$

$$\begin{pmatrix} \sqrt{2}d_{34}\cos(\theta+\delta)u_1 + \sqrt{2}d_{44}\sin(\theta+\delta)u_1 + d_{14}\cos(\theta+\delta)u_2 + d_{24}\left(\frac{\Gamma}{u_1^2} - \sin(\theta+\delta)u_2\right) \\ \sqrt{2}d_{44}\cos(\theta+\delta)u_1 - \sqrt{2}d_{34}\sin(\theta+\delta)u_1 - d_{24}\cos(\theta+\delta)u_2 + d_{14}\left(-\frac{\Gamma}{u_1^2} - \sin(\theta+\delta)u_2\right) \\ -\sqrt{2}d_{14}\cos(\theta+\delta)u_1 + \sqrt{2}d_{24}\sin(\theta+\delta)u_1 + \frac{d_{44}\Gamma}{u_2^2} \\ -\sqrt{2}d_{24}\cos(\theta+\delta)u_1 - \sqrt{2}d_{14}\sin(\theta+\delta)u_1 - \frac{d_{34}\Gamma}{u_2^2} \end{pmatrix}, \tag{3.4}$$

$\theta = 2\varphi_1 - \varphi_2$ is the optical phase that varies with propagation length and δ is user set parameter. The complicated matrix in (3.4) can be evaluated numerically in a few simple sequential steps. First we recognize that the contributions of the mean field terms can be obtained directly by numerically solving equations 3.1. Next, we use these generated numbers along with the initial conditions for the fluctuations that were obtained by numerically solving equation 2.4.2. We can evaluate S_x, S_y for a few select initial conditions and plot the results. From figure 3.11 we see that the X quadrature undergoes de-squeezing as the external phase parameter δ is tuned away from 0. The Y-quadrature also undergoes de-squeezing. Clearly, this is not promising because an increase in fluctuations would imply a degradation of signal to noise ratio. But all hope is not lost! Suppose we ask the question, is there a minimum value of X-quadrature squeezing, i.e one that is smaller than the vacuum noise? If so, what are the conditions under which this occurs? To answer this question, we have to transform to a different quadrature basis. It must be noted that transforming to a different basis still preserves physical properties, i.e. commutator relationships are preserved and this would imply that Heisenberg's uncertainty is not violated $Sx \times Sy \geq 1$. We use this as a check in our simulation.

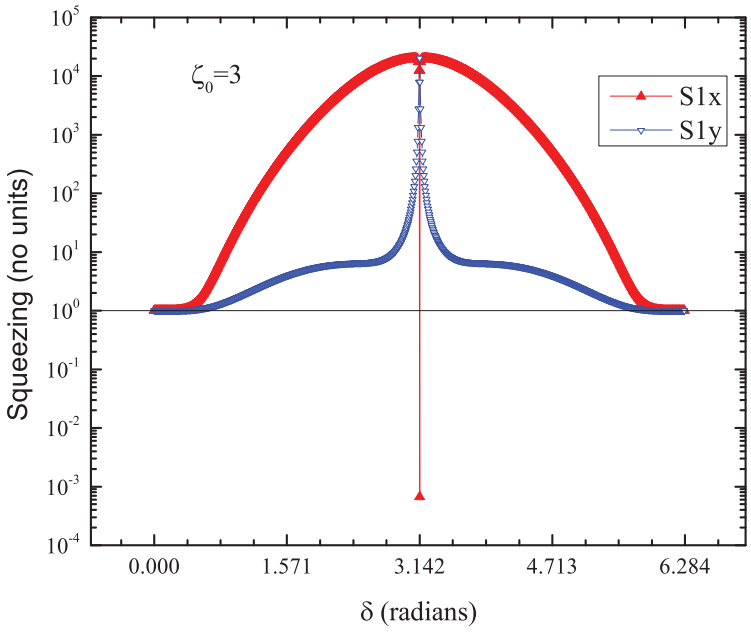

Figure 3.11. X quadrature squeezing (solid triangle) and Y quadrature squeezing (open triangles) as a function of interferometer phase δ. The Sx point at 10^{-3} is the value of X quadrature squeezing for the special case of $\delta = \pi$ discussed in the previous chapter.

3.3.2 Optimum Squeezing

When we introduce a phase shift, it is possible that maximum squeezing may not occur in either the amplitude or the phase quadrature. We can calculate the quadrature with maximum amplitude squeezing by defining a quadrature at an arbitrary phase α_j. We investigate the possibility of rotating to a quadrature where the value of S, the squeezing is optimum.

The field operator $\hat{a}$ and its conjugate can be written in two different basis $(\hat{x}, \hat{y})$ and $(\hat{q}, \hat{p})$, where the former is the original basis and the latter is the basis where squeezing is minimum. We can define arbitrary quadratures as

$$\hat{q}_j = \frac{1}{2}\left(\hat{a}_j e^{-\mathrm{i}\alpha_j} + \hat{a}_j^\dagger e^{\mathrm{i}\alpha_j}\right)$$
$$\hat{p}_j = \frac{1}{2i}\left(\hat{a}_j e^{-\mathrm{i}\alpha_j} - \hat{a}_j^\dagger e^{\mathrm{i}\alpha_j}\right), \tag{3.5}$$

Using the original quadratures given by

$$\hat{x}_j = \frac{1}{2}\left(\hat{a}_j e^{-\mathrm{i}\varphi_j} + \hat{a}_j^\dagger e^{\mathrm{i}\varphi_j}\right), \hat{y}_j = \frac{1}{2i}\left(\hat{a}_j e^{-\mathrm{i}\varphi_j} - \hat{a}_j^\dagger e^{\mathrm{i}\varphi_j}\right),$$

We wish to transform from the *(x,y)* basis to the *(q,p)* basis and therefore we can express the new quadratures in terms of the old as

$$\hat{q}_j = \hat{x}_j \cos\beta_j + \hat{y}_j \sin\beta_j \tag{3.6}$$
$$\hat{p}_j = -\hat{x}_j \sin\beta_j + \hat{y}_j \cos\beta_j, \tag{3.7}$$

where $\beta_j = \alpha_j - \varphi_j$.

To calculate squeezing, we have to calculate the variance of the field operators $(\langle\Delta\hat{q}^2\rangle, \langle\Delta\hat{p}^2\rangle)$. Therefore, we have

$$\langle\Delta\hat{q}_j^2\rangle = \langle\hat{q}_j^2\rangle - \langle\hat{q}_j\rangle^2, \tag{3.8}$$

$$\hat{q}_j^2 = \hat{x}_j^2 \cos^2\beta_j + \hat{y}_j^2 \sin^2\beta_j + \frac{1}{2}\sin 2\beta(\hat{x}_j\hat{y}_j + \hat{y}_j\hat{x}_j)$$
$$\langle\hat{q}_j^2\rangle = \langle\hat{x}_j^2\rangle \cos^2\beta_j + \langle\hat{y}_j^2\rangle \sin^2\beta_j + \frac{1}{2}\sin 2\beta\langle(\hat{x}_j\hat{y}_j + \hat{y}_j\hat{x}_j)\rangle,$$

Using the correlation definitions for the quadratures, we can get

$$\langle\hat{q}_j^2\rangle = \langle\hat{x}_j^2\rangle \cos^2\beta_j + \langle\hat{y}_j^2\rangle \sin^2\beta_j$$
$$\langle\hat{q}_j\rangle^2 = \langle\hat{x}_j\rangle^2 \cos^2\beta_j + \langle\hat{y}_j\rangle^2 \sin^2\beta_j + \langle\hat{x}_j\hat{y}_j\rangle \sin 2\beta_j,$$

Therefore, the variance in the q-quadrature is given as

$$\langle \Delta \hat{q}_j^2 \rangle = \{\langle \hat{x}_j^2 \rangle - \langle \hat{x}_j \rangle^2\} \cos^2 \beta_j + \{\langle \hat{y}_j^2 \rangle - \langle \hat{y}_j \rangle^2\} \sin^2 \beta_j + \langle \hat{x}_j \hat{y}_j \rangle \sin 2\beta_j$$
$$\langle \Delta \hat{q}_j^2 \rangle = \langle \Delta \hat{x}_j^2 \rangle \cos^2 \beta_j + \langle \Delta \hat{y}_j^2 \rangle \sin^2 \beta_j + \langle \hat{x}_j \hat{y}_j \rangle \sin 2\beta_j, \tag{3.9}$$

We originally defined squeezing as

$$S_{jx} = \frac{\langle \hat{x}_j(\zeta)^2 \rangle}{\langle \hat{x}_j(0)^2 \rangle}$$
$$S_{jy} = \frac{\langle \hat{y}_j(\zeta)^2 \rangle}{\langle \hat{y}_j(0)^2 \rangle}$$
$$\langle \hat{x}_j(\zeta)^2 \rangle = \frac{S_{jx}}{4}$$
$$\langle \hat{y}_j(\zeta)^2 \rangle = \frac{S_{jy}}{4}$$
$$S_{jxy} = \frac{\langle \hat{x}_j(\zeta) \hat{y}_j(\zeta) \rangle}{\langle \hat{x}_j(0) \rangle \langle \hat{y}_j(0) \rangle}$$
$$\langle \hat{x}_j(\zeta) \hat{y}_j(\zeta) \rangle = \frac{S_{jxy}}{4}, \tag{3.10}$$

Finally,we have

$$\langle \Delta \hat{q}_j^2 \rangle = \frac{1}{4} \{S_{jx} \cos^2 \beta_j + S_{jy} \sin^2 \beta_j - S_{jxy} \sin 2\beta_j\},$$

Similarly, we can get the variance for the phase quadrature as

$$\langle \Delta \hat{p}_j^2 \rangle = \frac{1}{4} \{S_{jx} \cos^2 \beta_j + S_{jy} \sin^2 \beta_j + S_{jxy} \sin 2\beta_j\},$$

We can explicitly write the q-quadrature fluctuations as

$$\langle \Delta \hat{q}^2(2\zeta) \rangle = \langle \Delta \hat{x}^2(2\zeta) \rangle \cos^2 \beta + \langle \Delta \hat{y}^2(2\zeta) \rangle \sin^2 \beta - \tag{3.11}$$
$$\frac{1}{2} \sin 2\beta \{(\langle \hat{x}(2\zeta) \hat{y}(2\zeta) \rangle - \langle \hat{x}(2\zeta) \hat{y}(2\zeta) \rangle) + (\langle \hat{y}(2\zeta) \hat{x}(2\zeta) \rangle - \langle \hat{y}(2\zeta) \hat{x}(2\zeta) \rangle)\},$$

Designating the first term as $S_{1x} = A$, the second as $S_{1y} = B$ and the third term within parenthesis as $S_{1xy} = C$, we can calculate the value of β at which squeezing is an optimum (minimum) and the value of squeezing by evaluating $\frac{\partial}{\partial\beta}\langle\Delta\hat{q}^2\rangle = 0$, which gives:

$$\boxed{\begin{aligned} \beta &= \frac{1}{2}\tan^{-1}\frac{2C}{B-A} \\ S_q &= \frac{1}{2}\{A+B-\sqrt{4C^2+(B-A)^2}\} \end{aligned}} \tag{3.12}$$

In the actual computation, we revert back to working with the coefficient representation of the quadrature field operators. We can write the output of the first stage (from chapter 2) in compact form as $X_{ij}(\zeta) = C_{ik} \cdot X(0)_{kj}$ and the output after the second stage is gives as $X_{ij}(2\zeta) = D_{il} \cdot X_{lj}(\zeta) = D_{il} \cdot C_{lk} \cdot X_{kj}(0)$. Using this to evaluate Sq we obtain:

$$\boxed{\begin{aligned} S_{1x}(2\zeta) &= f_1 d_{11}^2 + f_2 d_{12}^2 + f_3 d_{13}^2 + f_4 d_{14}^2 + 2(f_5 d_{11} d_{13} + f_6 d_{12} d_{14}) \\ S_{1y}(2\zeta) &= f_1 d_{21}^2 + f_2 d_{22}^2 + f_3 d_{23}^2 + f_4 d_{24}^2 + 2(f_5 d_{21} d_{23} + f_6 d_{22} d_{24}) \\ S_{1xy}(2\zeta) &= f_1 d_{11} d_{21} + f_2 d_{12} d_{22} + f_3 d_{13} d_{23} + f_4 d_{14} d_{24} + \\ &\quad f_5(d_{11} d_{23} + d_{21} d_{13}) + f_6(d_{12} d_{24} + d_{22} d_{14}), \end{aligned}} \tag{3.13}$$

Where f_j are values of squeezing and correlations after the first stage.

$$\begin{aligned} f_1 &= c_{11}^2 + c_{13}^2 \\ f_2 &= c_{24}^2 + c_{22}^2 \\ f_3 &= c_{31}^2 + c_{33}^2 \\ f_4 &= c_{42}^2 + c_{44}^2 \\ f_5 &= (c_{11} c_{31} + c_{13} c_{33}) \\ f_6 &= (c_{42} c_{22} + c_{44} c_{24}), \end{aligned}$$

It can be seen that we now have $X - Y$ cross terms that arise, i.e the term S_{1xy}. The significance of this term is that it is an indicator of the minimum value of squeezing and the shift of this minimum away from the canonical (X) quadrature.

From figure 3.11 we see that as the phase δ is varied the fluctuations in the X-quadrature increase rapidly and as discussed in the previous chapter, this is not the optimum quadrature. The transformed quadrature Q however, exhibits squeezing below the vacuum level of 1. We discuss the data in detail in the next section.

3.3.3 Results and Discussion

3.3.3.1. X,Y Squeezing

Figures 3.12 to 3.20 show the evolution of intensity (X) and phase (Y) quadrature fluctuations as a function of δ, the interferometer phase. We see that both quadratures are de-squeezed, except at $\delta = \pi$. There are two important aspects of the squeezing plots that have a direct bearing on the usable range of the interferometer. First, we take a look at the region close to zero, i.e $\delta \ \varepsilon \ [0, 0.2]$. In this region S_x and S_y are almost equal and upon zooming in, the numerical results show noisy behavior (see insets). This behavior persists with change in numerical parameters such as step size, number of steps and even upon use of different methods. Hence we conclude that this unstable behavior is inherent in the system. Next, we see that at some δ, S_x and S_y cross. This has a serious bearing on the squeezing angle β as a change in sign leads to discontinuities. The number of crossing points dictates the usability range of the interferometer. For small characteristic lengths ζ_0, there is at most one crossing point, but as the length is increased, the crossing point shifts to the right, i.e. towards increasing δ. Figure 3.12 shows only one possible region of crossing, very close to zero. As we increase ζ_0, a second crossing region develops near $\delta = \pi/2$ (figures 3.13 to 3.17). Another point to note about the figures is that as ζ_0 increases, the second

crossing region moves towards $\delta = \pi$. We will see later that these crossing regions between S_x and S_y are undesirable and detrimental to interferometer operation.

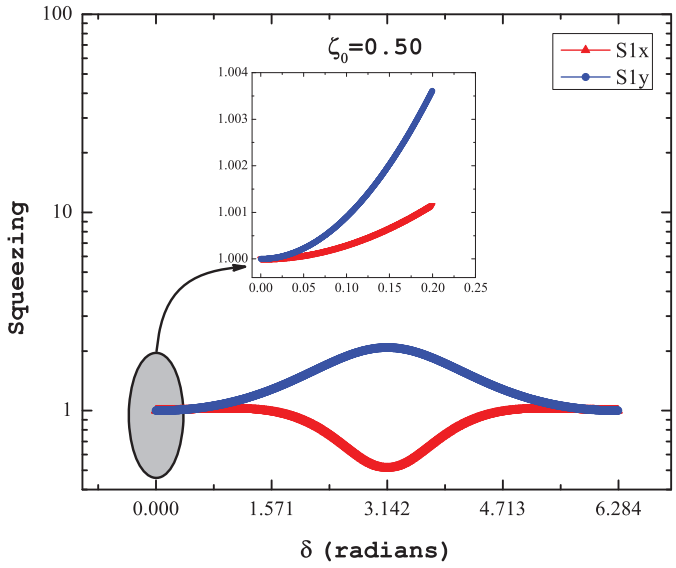

Figure 3.12. The main figure describes X (triangle) and Y (circle) squeezing for $\zeta_0 = 0.5$ as a function of interferometer phase δ. The inset depicts a region where Sx and Sy are almost equal.

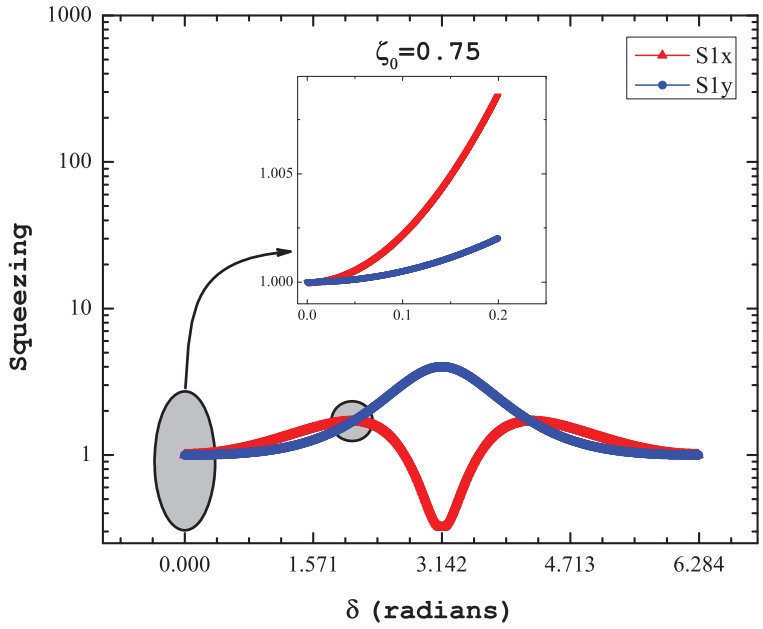

Figure 3.13. The main figure describes X (triangle) and Y (circle) squeezing for $\zeta_0 = 0.75$ as a function of interferometer phase δ. The inset depicts a region where Sx and Sy are almost equal. Sx and Sy cross close to $\delta = \pi/2$.

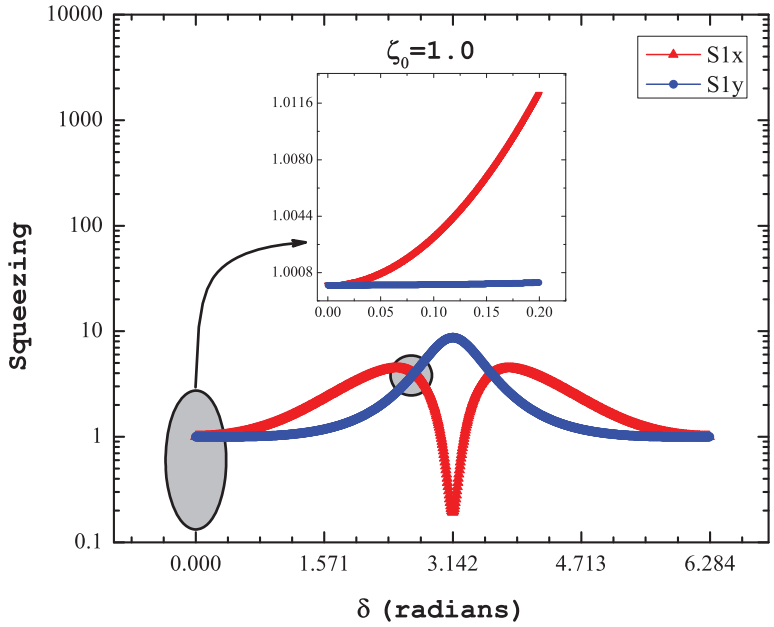

Figure 3.14. The main figure describes X and Y squeezing for $\zeta_0 = 1.0$ as a function of interferometer phase δ. Sx and Sy cross close to $delta = \pi$. The inset on right depicts a region where Sx and Sy are almost equal.

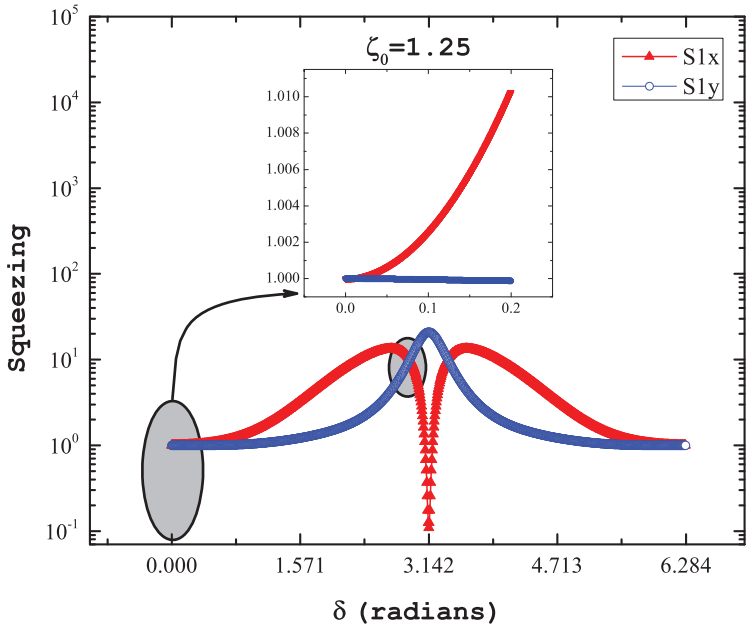

Figure 3.15. The main figure describes X (triangle) and Y (circle) squeezing for $\zeta_0 = 1.25$ as a function of interferometer phase δ. The inset depicts a region where Sx and Sy are almost equal.

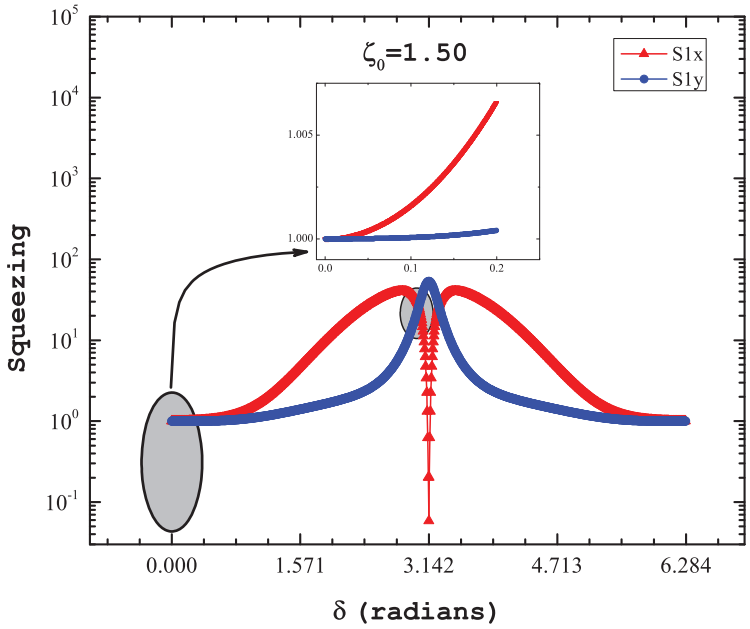

Figure 3.16. The main figure describes X (triangle) and Y (circle) squeezing for $\zeta_0 = 1.5$ as a function of interferometer phase δ. The inset depicts a region where Sx and Sy are almost equal.

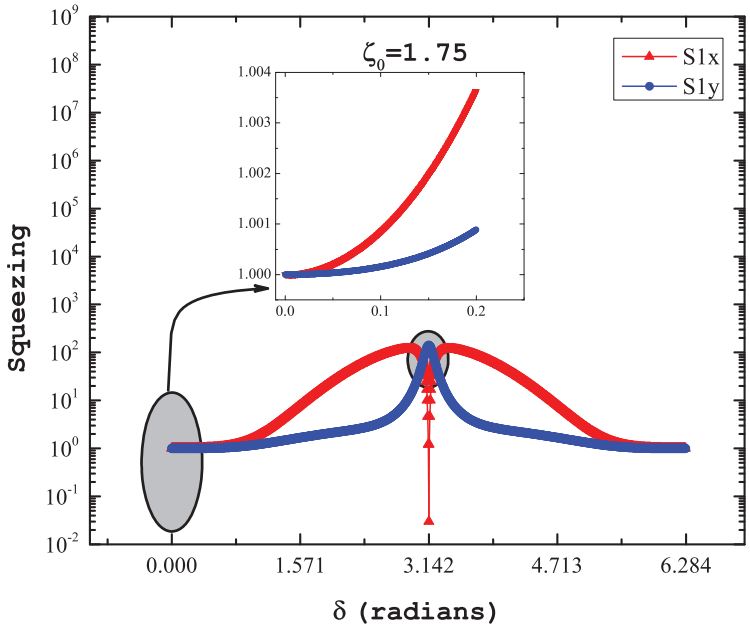

Figure 3.17. The main figure describes X (triangle) and Y (circle) squeezing for $\zeta_0 = 1.75$ as a function of interferometer phase δ. The inset depicts a region where Sx and Sy are almost equal.

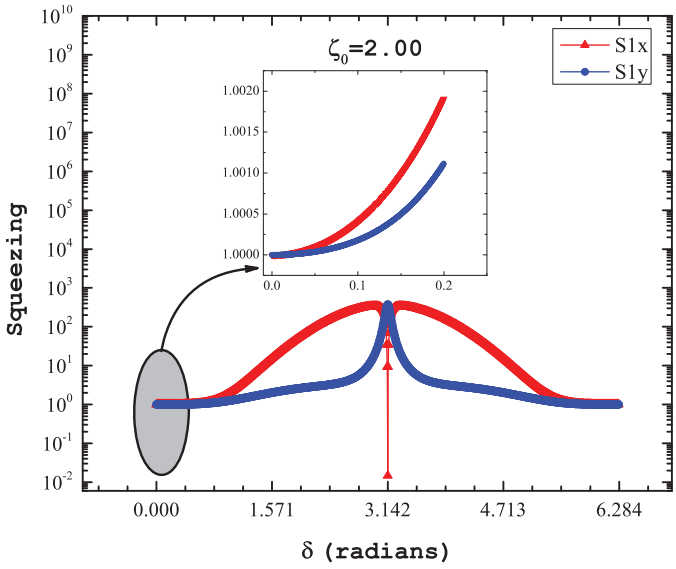

Figure 3.18. The main figure describes X (triangle) and Y (circle) squeezing for $\zeta_0 = 2$ as a function of interferometer phase δ. The inset depicts a region where Sx and Sy are almost equal.

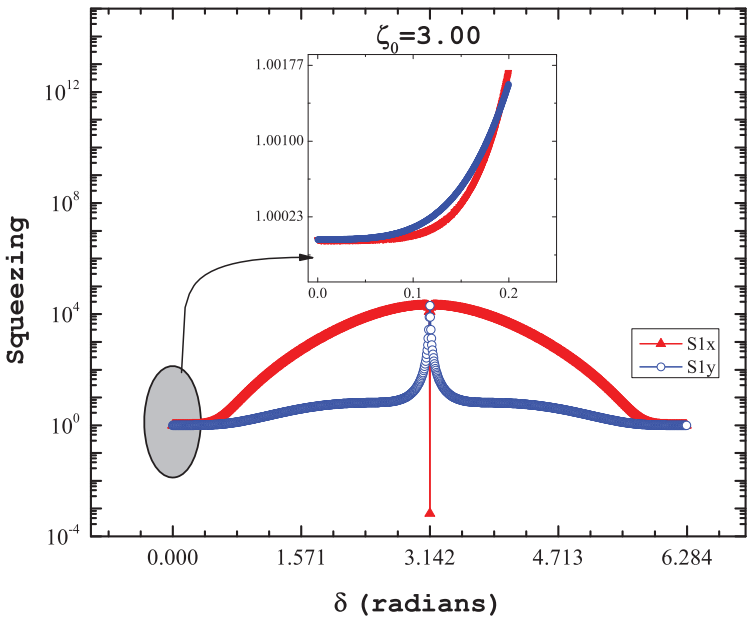

Figure 3.19. The main figure describes X (triangle) and Y (circle) squeezing for $\zeta_0 = 3$ as a function of interferometer phase δ. The inset depicts a region where Sx and Sy are almost equal.

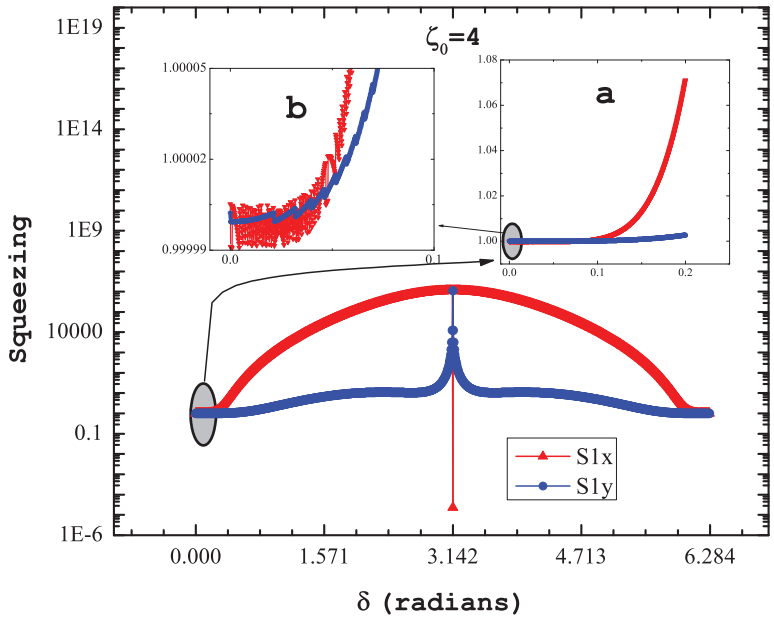

Figure 3.20. The main figure describes X (triangle) and Y (circle) squeezing for $\zeta_0 = 4$ as a function of interferometer phase δ. The inset (a) depicts a region where Sx and Sy are almost equal. Inset (b) shows fluctuations in Sx.

3.3.3.2. Q-Quadrature Squeezing

From the figure 3.21 it can be seen that Sq can go below the vacuum level (indicated by the horizontal line $F1$) for certain range of phase angle δ. The squeezing scales with interaction length and one may be tempted to conclude that by merely having a long crystal we could obtain arbitrarily large SNR. However, as the interaction length increases, after the SHG stage, the intensity of the phase sensing field decreases rapidly. For low values of the phase sensing field, it is possible that our linearization approximation breaks down, but we have not investigated this in detail.

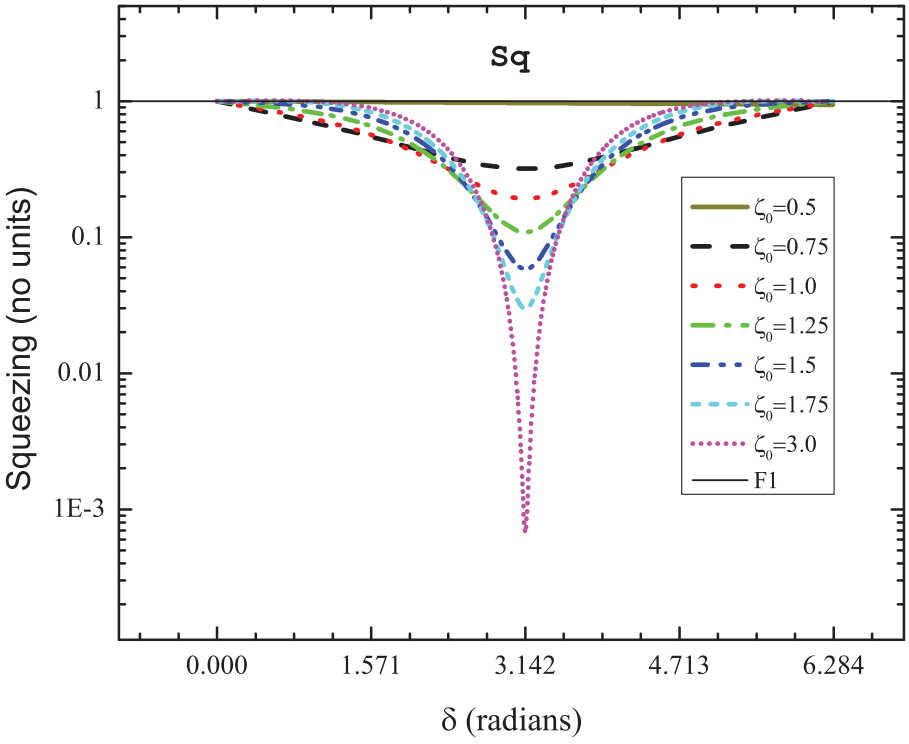

Figure 3.21. Q-quadrature squeezing for different interaction lengths. It can be seen that as the interaction length increases, so does squeezing.

3.3.3.3. Squeezing Angle β

The squeezing angle gives us an indication of the useful operating range of the interferometer. More specifically, we identify smooth, continuous regions of the plot as stable and discontinuous regions as unstable. It should be noted that this has nothing to do with the numerical stability of our differential equations (which are a function of length) but instead indicate the behavior of our system response to different initial conditions encapsulated by the conserved quantity (Γ). Discontinuities arise mainly due to the crossing behavior of S_x and S_y which generates an abrupt change in sign and causes β to latch to extreme values of $\pm\pi/4$.

Figures 3.22 to 3.30 show the squeezing angle as a function of interferometer phase δ. For small characteristic length $\zeta_0 = 0.5$, we see that there are less discontinuities in the squeezing angle (inset of figure 3.22). At $\delta = 0$, the Q-quadrature is the same as the X-quadrature and therefore the squeezing angle is simply 0. However, as we increase the characteristic length ζ_0, we see a few trends in the squeezing angle graphs. First, the graph is broken up into three separate regions symmetric about $\delta = \pi$. From $\zeta_0 = 0.75$ to $\zeta_0 = 4$, the central segment about $\delta = \pi$ gets progressively compressed (main figures 3.23 to 3.30). In addition to this, the fluctuations in the squeezing angle close to $\delta = 0$ begin to progressively increase (inset of figures 3.23 to 3.30).

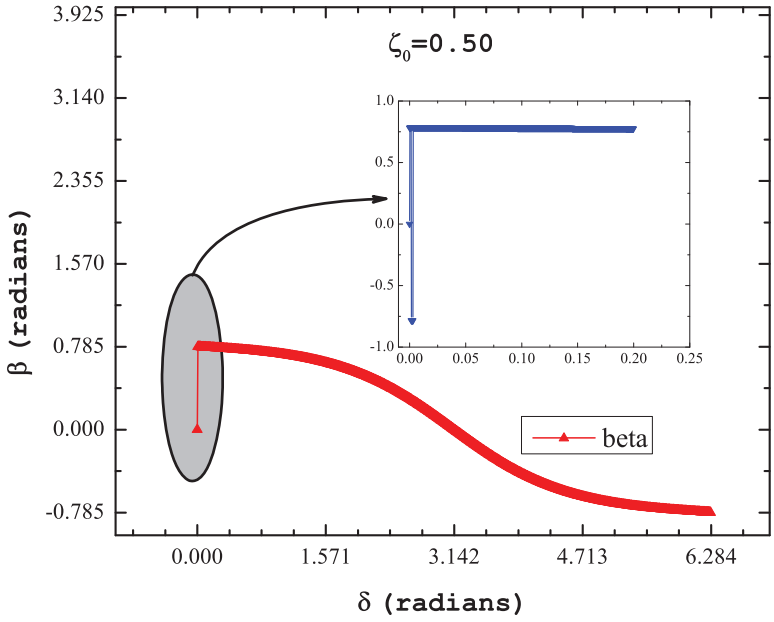

Figure 3.22. Main figure shows the squeezing angle for a length of $\zeta_0 = 0.5$. The inset shows fluctuations in squeezing angle.

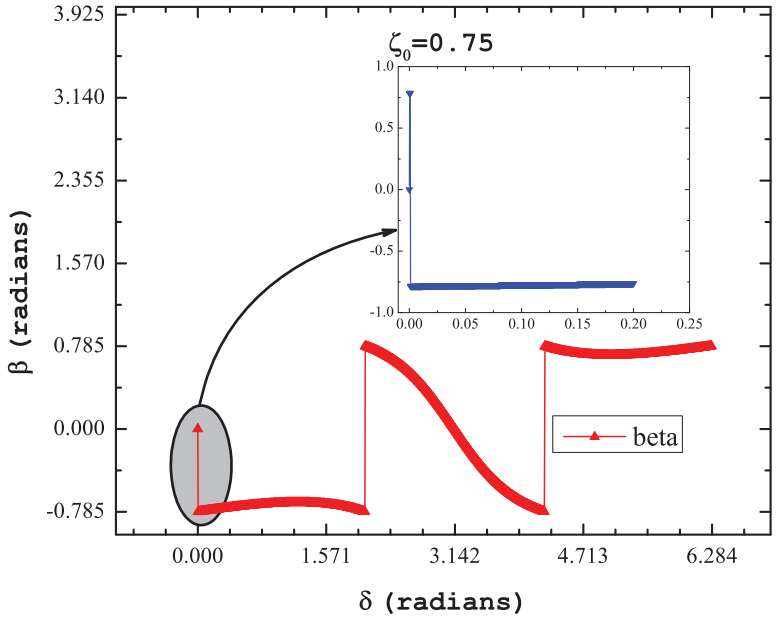

Figure 3.23. Main figure shows the squeezing angle for a length of $\zeta_0 = 0.75$. The inset shows fluctuations in squeezing angle.

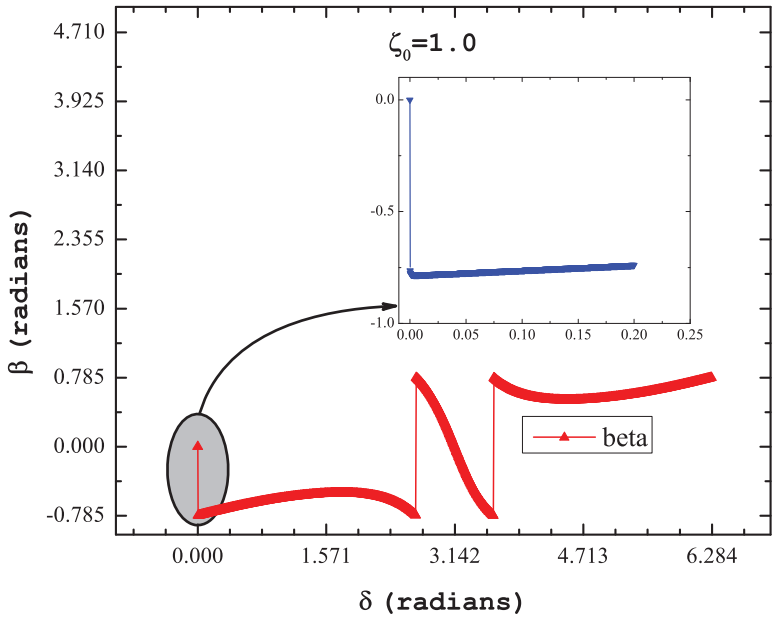

Figure 3.24. Main figure shows the squeezing angle for a length of $\zeta_0 = 1.0$. The inset shows fluctuations in squeezing angle.

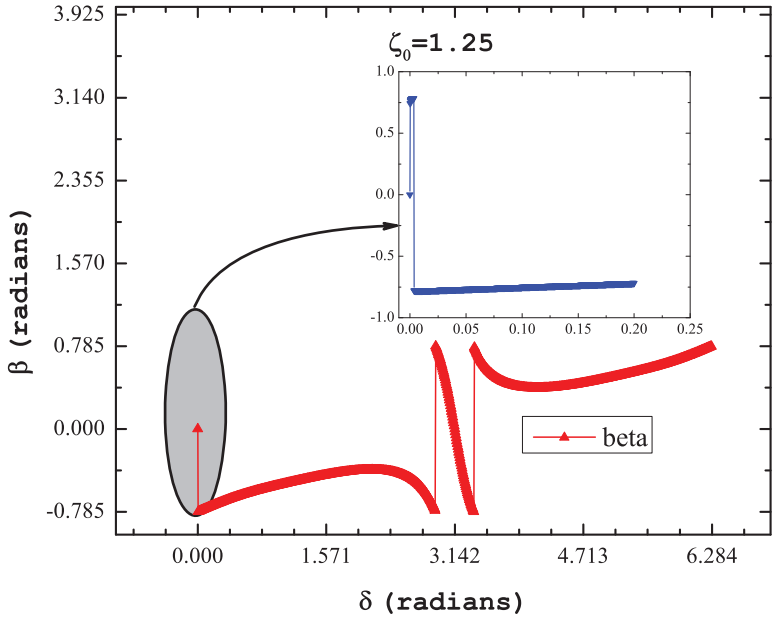

Figure 3.25. Main figure shows the squeezing angle for a length of $\zeta_0 = 1.25$. The inset shows fluctuations in squeezing angle.

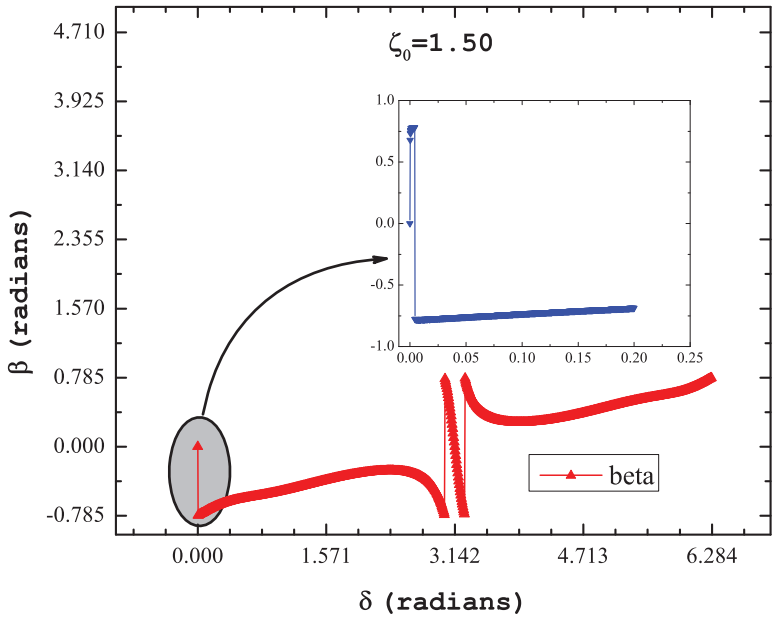

Figure 3.26. Main figure shows the squeezing angle for a length of $\zeta_0 = 1.50$. The inset shows fluctuations in squeezing angle.

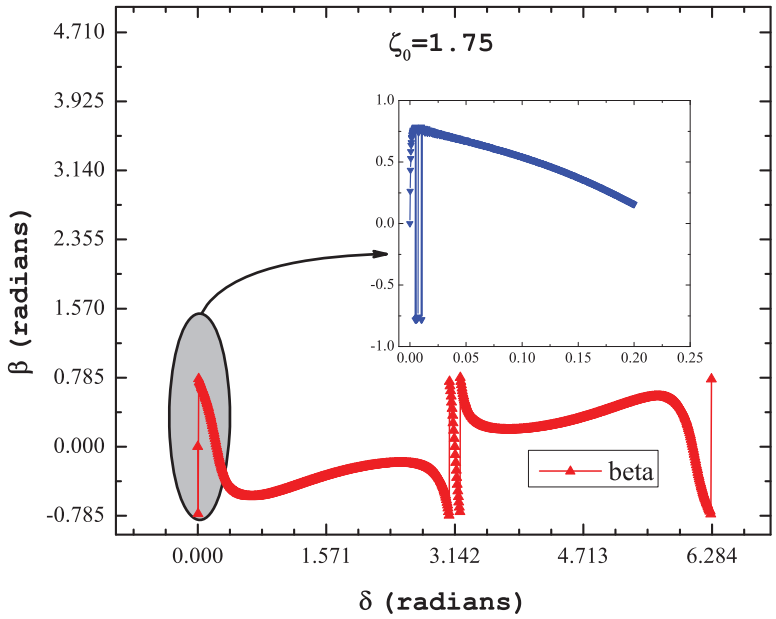

Figure 3.27. Main figure shows the squeezing angle for a length of $\zeta_0 = 1.75$. The inset shows fluctuations in squeezing angle.

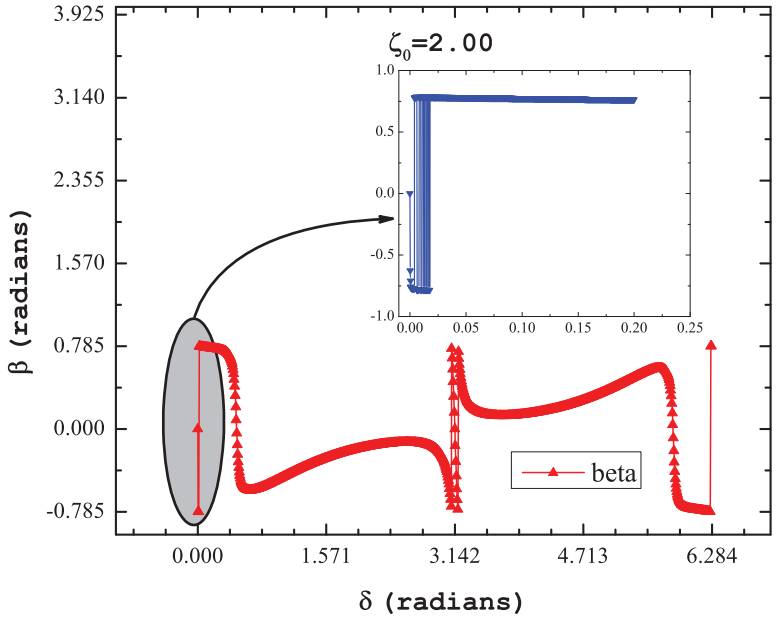

Figure 3.28. Main figure shows the squeezing angle for a length of $\zeta_0 = 2$. The inset shows fluctuations in squeezing angle.

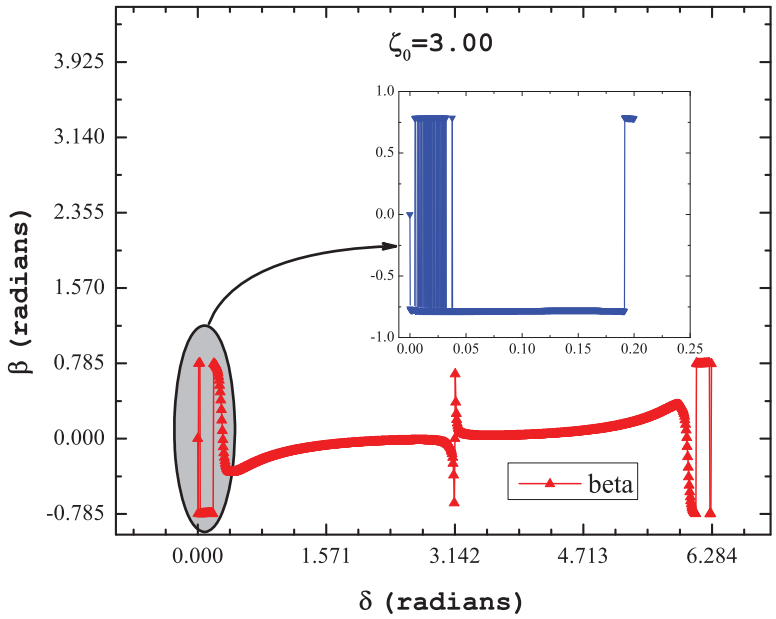

Figure 3.29. Main figure shows the squeezing angle for a length of $\zeta_0 = 3$. The inset shows fluctuations in squeezing angle.

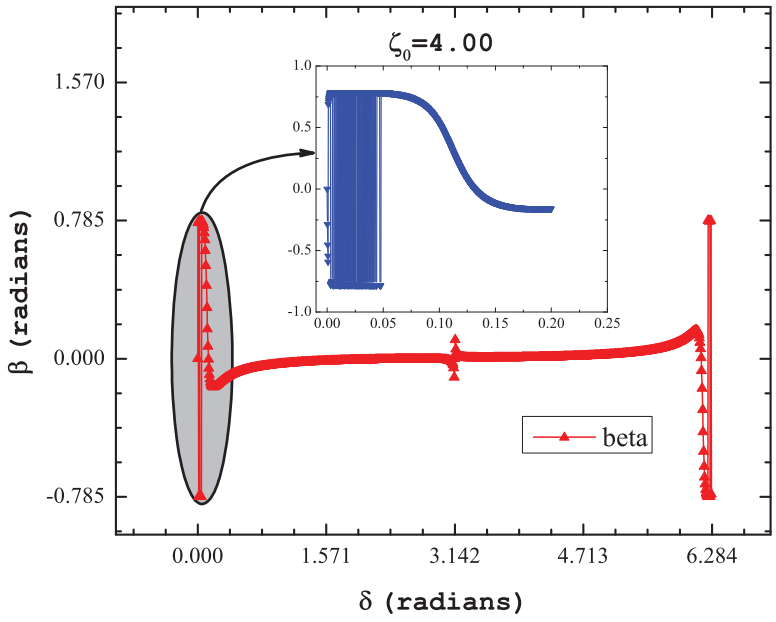

Figure 3.30. Main figure shows the squeezing angle for a length of $\zeta_0 = 4$. The inset shows fluctuations in squeezing angle.

3.4 Rotating X-quadrature to Q-quadrature by an Optical Cavity

In the previous section we discovered that it was possible to obtain reduced quadrature fluctuations if the measurement angle was shifted away from the canonical X-Y quadratures and we calculated the squeezing angle β at which the fluctuations are minimized. In other words, we have to rotate our measuring device by a certain angle ψ to observe this squeezing. The question now is, how do we do it in practice? In this section we present a way to accomplish this experimentally. Our choice of technique is based on the practical limitations involved in detecting quantum fluctuations of a bright (intense) field. In a traditional Mach-Zehnder interferometric setup, measuring the intensity difference between output ports, it is possible to infer the relative phase between the two paths.

The central devices to this technique are an empty optical cavity and a spectrum analyzer (SA). A SA is an electronic device that is used to measure the power spectrum of a signal. To transfer information from the optical domain (THz frequency) to the electronic domain (GHz or MHz) it is necessary to down-shift the signal and therefore the SA is usually based on the super-heterodyne principle [45] where the input RF signal from the photodiode is converted to an intermediate frequency that is analyzed after filtering.

An interferometer directly measures the X quadrature and its fluctuations, but this is not the quadrature where squeezing is optimum. The optimum quadrature is the Q-quadrature, so we need to rotate the angle and this can be accomplished by an optical cavity [46, 47]. This technique relies on the fact that the cavity has a frequency dependent response, i.e. different frequency components acquire different phase shifts. The output light from the cavity consists of the sum of electric fields from the direct reflection from the front mirror and the leaked light from inside the cavity. This is not the same as the input light and therefore in any calculation of SNR, we need to calculate the quadrature rotated signal which is precisely the output of the optical cavity. This is accomplished as shown in figure 3.31.

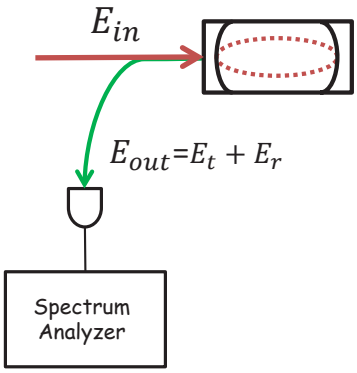

Figure 3.31. Schematic of the detection apparatus.

In the previous sections we discussed introducing an external phase δ and studying the interferometer response. The amplified phase sensing field at the output of the interferometer is given as

$$a(t) = A(1 + m\sin\delta)e^{-i\omega_0 t}e^{i(\varphi+\beta\sin\delta)}, \tag{3.14}$$

Equation 3.14 consists of both amplitude and phase modulation. We can expand equation 3.14 as

$$\bar{a}(t) = A(1 + \frac{m}{2i}(e^{i\delta} - e^{-i\delta}))(1 + \frac{\beta}{2}(e^{i\delta} - e^{-i\delta})e^{-i\omega_0 t}, \tag{3.15}$$

For small modulations, we can neglect $m\beta$ terms and we end up with:

$$\bar{a}(t) = A(1 + \frac{1}{2}(\beta - im)e^{i\delta} - \frac{1}{2}(\beta - im)e^{-i\delta})e^{-i\omega_0 t}, \tag{3.16}$$

Sending the field through a cavity imposes phase shifts on each of the frequency components, i.e $f(\delta) \rightarrow f(\delta)e^{i\varphi_j}$, where φ_j is the cavity imposed phase shift on the j^{th} frequency component, therefore we have

$$\bar{a}(t) = A(1 + \frac{1}{2}(\beta - im)e^{i\delta}e^{i\varphi_1} - \frac{1}{2}(\beta - im)e^{-i\delta}e^{i\varphi_2})e^{-i\omega_0 t}, \tag{3.17}$$

The photodetector measures intensity i.e. $I = \mid \bar{a} \mid^2 = a^* a$ and therefore we have

$$\begin{aligned} I \approx A^2(1 + \frac{1}{2}(\beta + im)e^{-i\delta}e^{-i\varphi_1} - \frac{1}{2}(\beta + im)e^{i\delta}e^{-i\varphi_2})\times \\ (1 + \frac{1}{2}(\beta - im)e^{i\delta}e^{i\varphi_1} - \frac{1}{2}(\beta - im)e^{-i\delta}e^{i\varphi_2}), \end{aligned} \tag{3.18}$$

Neglecting higher order terms we have

$$\mid \bar{a} \mid^2 = A^2(1 + [\frac{(\beta - im)}{2}e^{i\varphi_1} - \frac{(\beta + im)}{2}e^{-i\varphi_2}] + c.c), \tag{3.19}$$

To get the signal, it is sufficient to analyze the positive frequency part of equation 3.19, which can be rewritten as

$$e^{i\frac{(\varphi_1 - \varphi_2)}{2}}[\frac{(\beta - im)}{2}e^{i(\varphi_1 + \varphi_2)} - \frac{(\beta + im)}{2}e^{-i(\varphi_1 - \varphi_2)}], \tag{3.20}$$

Defining $\Delta\varphi = (\varphi_1 + \varphi_2)/2$ and neglecting the global phase, we can write the signal as

$$\boxed{S = \beta \sin \Delta\varphi - m \cos \Delta\varphi} \tag{3.21}$$

$\Delta\varphi$ is the rotation imposed by the Fabry-Perot cavity on the mean field. We would now like to determine the relationship of this angle with the squeezing angle β and do so in the next section.

3.5 Time Domain Analysis

In this section we analyze what happens to the quantum fluctuations after frequency dependent phase shifts have been imposed on it by the Fabry-Perot cavity. The optical field is given as $a(\omega) = e^{i\theta(\omega)}$, where $\theta(\omega)$ is the phase associated with each spectral component of the light. In the time domain, the detector response is the Fourier transform of $a(\omega)$ and is given as

$$a(t) = \int d\omega a(\omega) e^{i\theta(\omega)} e^{-i\omega t}, \tag{3.22}$$

Writing the signal as a sum of its mean value $\bar{a}$ and fluctuations Δa, we have

$$a(t) = \int d\omega [\bar{a}(\omega) + \Delta a(\omega)] e^{i\theta(\omega)} e^{-i\omega t}, \tag{3.23}$$

The carrier is assumed monochromatic so $\bar{a}(\omega) \rightarrow \bar{a}(\omega_0)$ and hence equation 3.23 describes a carrier with a small bandwidth of frequencies around the central frequency. This can be further simplified as

$$\begin{aligned} a(t) &= \int d\omega \bar{a}(\omega) \delta(\omega - \omega_0) e^{i\theta(\omega)} e^{-i\omega t} + \int d\omega \Delta a(\omega) e^{i\theta(\omega)} e^{-i\omega t} \\ &= \bar{a}(\omega_0) e^{i\theta(\omega_0)} e^{-i\omega_0 t} + \int d\omega \Delta a(\omega) e^{i\theta(\omega)} e^{-i\omega t}, \end{aligned}$$

A detector measures intensity $I(t) = a(t)^* a(t)$ and is given by

$$\begin{aligned} I(t) = \{\bar{a}(\omega_0) e^{i\theta(\omega_0)} e^{-i\omega_0 t} + \int d\omega \Delta a(\omega) e^{i\theta(\omega)} e^{-i\omega t}\}^* \times \\ \{\bar{a}(\omega_0) e^{i\theta(\omega_0)} e^{-i\omega_0 t} + \int d\omega \Delta a(\omega) e^{i\theta(\omega)} e^{-i\omega t}\}, \end{aligned} \tag{3.24}$$

Neglecting higher order terms, we have

$$I(t) =\mid \bar{a}(\omega_0) \mid^2 + \bar{a}^*(\omega_0) \int d\omega \Delta a(\omega) e^{i(\theta(\omega)-\theta(\omega_0))} e^{-i(\omega-\omega_0)t} + \bar{a}(\omega_0) \int d\omega \Delta a(\omega)^\dagger e^{-i(\theta(\omega)-\theta(\omega_0))} e^{i(\omega-\omega_0)t}, \tag{3.25}$$

We define the following variables and bear in mind that in a Fourier transform we have positive and negative frequency components and the limits are therefore $(-\infty, \infty)$ and $(\infty, -\infty)$ on the respective integrals

$$\begin{aligned} \Delta\theta(\omega) &= \theta(\omega) - \theta(\omega_0) \\ \omega - \omega_0 &= \Omega \\ \varphi_1 = \Delta\theta(-\Omega) &= \theta(\omega_0 - \Omega) - \theta(\omega_0) \\ \varphi_2 = \Delta\theta(\Omega) &= \theta(\omega_0 + \Omega) - \theta(\omega_0), \end{aligned}$$

Substituting the above variables in equation 3.24we end up with

$$I(t) =\mid \bar{a}(\omega_0) \mid^2 + \bar{a}^*(\omega_0) \int d\Omega \Delta a(\omega_0 + \Omega) e^{i\Delta\theta(\Omega)} e^{-\Omega t} + \bar{a}(\omega_0) \int d\Omega \Delta a^\dagger(\omega_0 - \Omega) e^{-i\Delta\theta(-\Omega)} e^{-\Omega t}, \tag{3.26}$$

In the most general sense, we can write the classical amplitude of an electric field as a sum of its mean value and fluctuations about the mean.

$$a = \overline{a} + \Delta a, \tag{3.27}$$

Using this, we can write

$$I(t) =\mid \bar{a}(\omega_0) \mid^2 + \mid a(\bar{\omega}_0) \mid e^{i\varphi_0} \int d\Omega \Delta a(\omega_0 + \Omega) e^{i\Delta\theta(\Omega)} e^{-\Omega t} + \mid a(\bar{\omega}_0) \mid e^{i\varphi_0} \int d\Omega \Delta a^\dagger(\omega_0 - \Omega) e^{-i\Delta\theta(-\Omega)} e^{-\Omega t}, \tag{3.28}$$

Thus far we have described the response of an ideal detector to an optical field. Our strategy for completing the analysis is as follows: First, we derive the consequences of imposing frequency dependent phase shifts and demonstrate mathematically what exactly the rotation of quadratures means. Next we use equation 3.26 and verify that the quantum fluctuations rotate with the same angle as the mean field .

Since we work with intense fields, we make the assumption $\mid \Delta a(t) \mid \ll \mid \overline{a} \mid$. A photodetector measures the field intensity given as

$$\begin{aligned} I(t) = a^*(t)a(t) &= (\overline{a^*} + \Delta a^*(t))(\overline{a} + \Delta a(t)) \\ &= u^2 + u(\Delta a(t)e^{-i\varphi_0} + \Delta a^*(t)e^{i\varphi_0}), \end{aligned} \tag{3.29}$$

The second term is the perturbation in the field amplitude which we express as

$$\Delta I(t) = u(\Delta a(t)e^{-i\varphi_0} + \Delta a^*(t)e^{i\varphi_0}), \tag{3.30}$$

The amplitude quadrature is defined as

$$\Delta x = \Delta a(t)e^{-i\varphi_0} + \Delta a^*(t)e^{i\varphi_0}, \tag{3.31}$$

The rotation from X-quadrature to the Q-quadrature is with φ_1, φ_2 being the cavity imposed, frequency dependent phase shifts, we can write the transformation equation as

$$\begin{aligned} \Delta q &= \Delta a(t)e^{-i\varphi_0}e^{-i\varphi_2} + \Delta a^*(t)e^{i\varphi_0}e^{-i\varphi_1} \\ &= e^{-i(\varphi_2+\varphi_1)/2}[\Delta a(t)e^{-i\varphi_0}e^{i(\varphi_1-\varphi_2)/2} + \Delta a^*(t)e^{i\varphi_0}e^{-i(\varphi_1-\varphi_2)/2}], \end{aligned} \tag{3.32}$$

Defining $\Delta\varphi = (\varphi_1 - \varphi_2)/2$ and neglecting the global phase term we obtain:

$$\boxed{\Delta q = \Delta a(t)e^{-i\varphi_0}e^{i\Delta\varphi} + \Delta a^*(t)e^{i\varphi_0}e^{-i\Delta\varphi},} \tag{3.33}$$

We can perform the same analysis on equation 3.26. From the second term, we can write Δq as

$$\Delta q = \Delta a(\omega_0 + \Omega)e^{-i\varphi_0}e^{i\varphi_2} + \Delta a(\omega_0 + \Omega)^\dagger e^{i\varphi_0}e^{i\varphi_1},$$

Getting rid of the global phase term and defining $\Delta\varphi$ as before, we end up with:

$$\boxed{\Delta q = \Delta a(\omega_0 + \Omega)e^{-i\varphi_0}e^{i\Delta\varphi} + \Delta a(\omega_0 - \Omega)^\dagger e^{i\varphi_0}e^{-i\Delta\varphi},} \tag{3.34}$$

The significance of equation 3.34 is readily seen when consider the term $\Delta\varphi = \varphi_1 - \varphi_2$, and we set $\varphi_1 = \varphi_2$ or $\Delta\varphi = 0$, then $\Delta q = \Delta x$. The point is, in order to rotate the X-quadrature to the Q-quadrature, we need phase shifts that are different. An optical cavity such as a Fabry-Perot cavity offers a simple and elegant avenue to accomplish this. To summarize, we have proved that both the spectral components of the mean field and the fluctuations associated with each mean field spectral component are rotated by the same phase angle.

In our discussion of squeezing angle, we defined the squeezing angle to be $\beta = \varphi_0 - \alpha$, where α (equation 3.7) was the amount the mean field phase given by φ_0 ought to be rotated by. We can clearly see that α is the same as $\Delta\varphi$ and hence the angle of rotation necessary to obtain best squeezing performance is:

$$\boxed{\Delta\varphi = \varphi_0 - \beta,} \tag{3.35}$$

We use the above angle in our analysis of interferometer performance described in the next section.

3.6 Interferometer Performance

3.6.1 SNR of the Nonlinear Interferometer

In this section, we calculate the SNR for a generic nonlinear interferometer. Consider a schematic described in figure (3.1). From equation 5.5, we identify that the perturbations in amplitude and phase introduced by modulating the phase sensing beam are give by $m_1 = \frac{du_1}{d\delta}$,$m_2 = \frac{d\varphi_0}{d\delta}$ and therefore the signal can be written as

$$S = \frac{d\varphi_1}{d\delta}\sin(\Delta\varphi) - \frac{du_1}{d\delta}\cos(\Delta\varphi), \tag{3.36}$$

Suppose we designate the mean field intensity as I_0, the total signal is given as $S = I_0\Delta I = k\epsilon$ (k is some constant of proportionality). The differential intensity is simply the amplified phase sensing field at the output of the interferometer and if we denote the phase sensing field as u_1' (i.e. after the PDC stage) we can write

$$I_0\Delta I = 2u_1'\Delta u_1' I_0 = 2u_1' k\delta I_0, \tag{3.37}$$

The quadrature noise is given by the value of the Q-Quadrature squeezing. The total noise depends on the light intensity and can be calculated as $u_1'\sqrt{I_0}\sqrt{S_q}$. This is the noise in the phase sensing beam of amplitude u_1'. We can therefore calculate Signal-to-Noise ratio as

$$SNR_{NL} = \frac{2\delta k\sqrt{I_0}}{\sqrt{S_q}}, \tag{3.38}$$

However, if we wish to compare the the performance of the nonlinear interferometer to a linear interferometer, we need the field prior to the output stage and thus $I_0 = I_{ps}/u_1^2$ where $u_1 = \operatorname{sech}\zeta_0$. Using this in equation 3.38we can write the SNR of a nonlinear interferometer as

$$SNR_{NL} = \frac{2k\delta\sqrt{I_{ps}}}{u_1\sqrt{S_q}}, \tag{3.39}$$

Finally, using 3.38 and the SNR for a linear interferometer from equation 3.47, we can define a performance metric $\mathcal{R} = SNR_{NL}/SNR_L$ given as

$$\boxed{\mathcal{R} = \frac{2k}{u_1\sqrt{S_q}}} \tag{3.40}$$

3.6.2 Linear Interferometer

Consider a simple Mach-Zehnder Interferometer made of 50:50 linear beamsplitters and a phase shifter. In the Heisenberg picture, we can write the beamsplitter and phase shifter operators as

$$\hat{B} = \frac{1}{\sqrt{2}}\begin{pmatrix} 1 & -i \\ -i & 1 \end{pmatrix}, \hat{P} = \begin{pmatrix} 1 & 0 \\ 0 & e^{i\varphi} \end{pmatrix}, \tag{3.41}$$

The output $(Out)= \hat{B}\hat{P}\hat{B} \times (In)$ is therefore given as

$$\begin{pmatrix} \hat{a}_{out} \\ \hat{b}_{out} \end{pmatrix} = -ie^{i\varphi/2}\begin{pmatrix} \sin\frac{\varphi}{2} & \cos\frac{\varphi}{2} \\ \cos\frac{\varphi}{2} & -\sin\frac{\varphi}{2} \end{pmatrix}\begin{pmatrix} \hat{a}_{in} \\ \hat{b}_{in} \end{pmatrix}, \tag{3.42}$$

We are interested in the output SNR. The signal is given by the average photon number and the noise is the variance in the average photon number. Explicitly evaluating the operator products we have

$$\begin{aligned} \hat{a}^\dagger_{out}\hat{a}_{out} &= \sin^2\frac{\varphi}{2}\hat{a}^\dagger_{in}\hat{a}_{in} + \cos^2\frac{\varphi}{2}\hat{b}^\dagger_{in}\hat{b}_{in} + \frac{1}{2}\sin\varphi(\hat{a}^\dagger_{in}\hat{b}_{in} - \hat{b}^\dagger_{in}\hat{a}_{in}) \\ \hat{b}^\dagger_{out}\hat{b}_{out} &= \cos^2\frac{\varphi}{2}\hat{a}^\dagger_{in}\hat{a}_{in} + \sin^2\frac{\varphi}{2}\hat{b}^\dagger_{in}\hat{b}_{in} - \frac{1}{2}\sin\varphi(\hat{a}^\dagger_{in}\hat{b}_{in} - \hat{b}^\dagger_{in}\hat{a}_{in}). \end{aligned} \tag{3.43}$$

With a coherent state $|\alpha\rangle$ at the first port and vacuum $|0\rangle$ at the second port, the input state is $|0\rangle\,|\alpha\rangle$. The output is obtained by applying the operator $\hat{a}^{\dagger}_{out}\hat{a}_{out}$ on the input and can be written as

$$I_{out} = \frac{1}{2}(\langle 0|\,\langle\alpha|\,\hat{a}^{\dagger}_{out}\hat{a}_{out}\,|0\rangle\,|\alpha\rangle = I_{ps}(1-\cos\varphi). \tag{3.44}$$

where $I_{ps} =\mid \alpha \mid^2 /2$ is the phase sensing signal.

We are working at a region where the slope of the intensity phase graph is a maximum ($\varphi = \pi/2$). We are interested in the signal ΔI_{out} which can be calculated from equation 3.44 for a small perturbation δ, around $\pi/2$ (such that $\varphi = \frac{\pi}{2} + \delta$) as

$$\frac{dI_{out}}{d\varphi} = I_{ps}\sin\varphi \approx I_{ps}\delta \tag{3.45}$$

where δ is the perturbation in the angle. The noise is given by the square root of the variance of the output photon number and for a coherent state with Poissonian statistics, we can calculate the noise as

$$\sqrt{\langle\Delta\hat{n}^2_{out}\rangle} = \sqrt{\langle\hat{n}^2_{out}\rangle - \langle\hat{n}_{out}\rangle^2} = \sqrt{\frac{1}{2}\mid\alpha\mid^2} = \sqrt{I_{ps}}, \tag{3.46}$$

where $\langle\hat{n}_{out}\rangle = \langle\hat{a}^{\dagger}_{out}\hat{a}_{out}\rangle =\mid \alpha \mid^2$ is the average photon number at the output.

Dividing equation 3.44 by 3.46 the SNR of a linear interferometer is given as

$$SNR_L = (\sqrt{I_{ps}})\delta. \tag{3.47}$$

3.6.3 Summary and Discussion

The results of our analysis encapsulated by equation 3.40 is plotted as a function of interferometer phase δ for different interaction lengths ζ_0 as shown in figures 3.32 to 3.40. The horizontal indicates the baseline value where the nonlinear interferom-

eter (NLI) and linear interferometer (LI) have the same SNR. Values below this line indicate worse performance of the NLI when compared to a LI.

We are interested in regions for which the NLI performance is greater than a corresponding LI. We see a general trend of increase in interferometer performance as the propagation length increases. For small interaction lengths (figure 3.32), there is no improvement over a linear interferometer and in fact it is worse for most of the operating range. We define two metrics that illustrate the usability of the nonlinear interferometer, performance (based on equation 3.40) and stable operating range. Only regions that do not have discontinuities offer stable operating range. We saw earlier that the squeezing angle had discontinuities for certain ranges of δ and this is the cause of instabilities that the discontinuities indicate. Physically, this means the unstable ranges of the interferometer are not experimentally useful. Another point to note is that the performance of a NLI varies with interferometer phase in a non-trivial way. For certain ranges of δ, the performance is much worse than a LI.

Improvement in performance with interaction length is due to squeezing of the phase sensing field. For larger interaction lengths, there is increased squeezing in the Q-quadrature, i.e. a decrease in noise, so not only does the visibility of the interference fringes improved, but also the noise of the signal is reduced.

To summarize, a nonlinear interferometer under conditions of harmonic generation can have better performance than a linear interferometer. We demonstrate theoretically that it is possible to obtain a performance improvement of about a factor of 60 over a linear interferometer. This improvement is because of both amplification and squeezing of the phase sensing beam. Squeezing occurs after the first nonlinear beamsplitter and enhancement of the squeezed signal occurs at the second nonlinear beamsplitter.

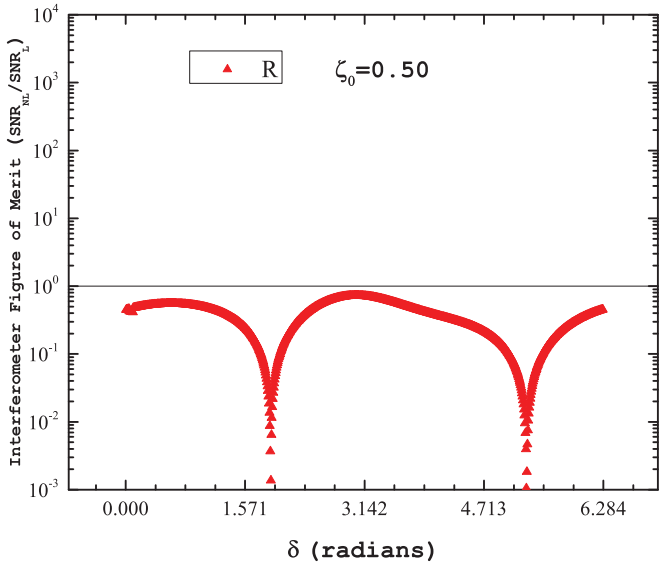

Figure 3.32. Interferometer performance for $\zeta = 0.5$.

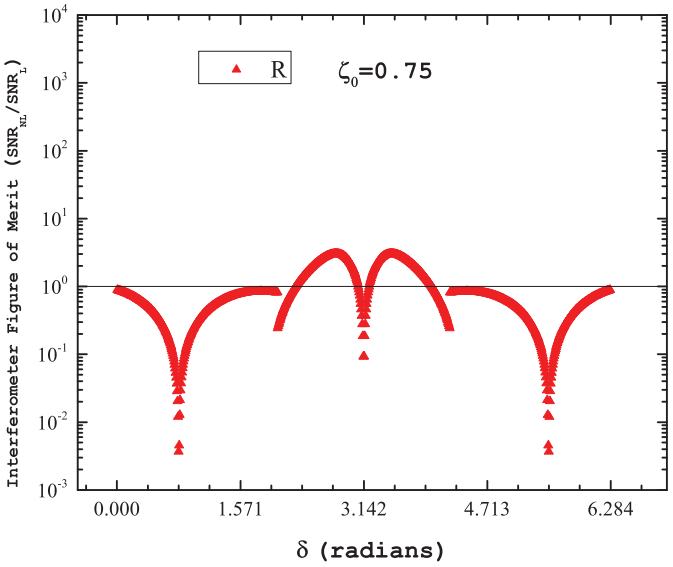

Figure 3.33. Interferometer performance for $\zeta = 0.75$.

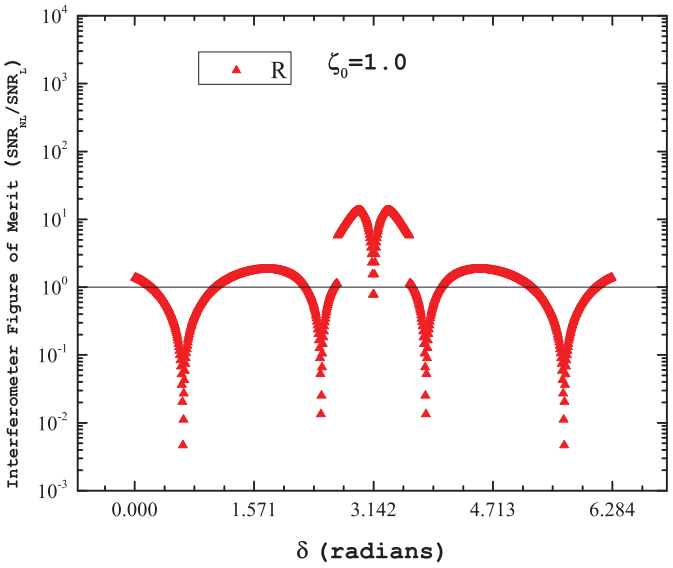

Figure 3.34. Interferometer performance for $\zeta = 1.0$.

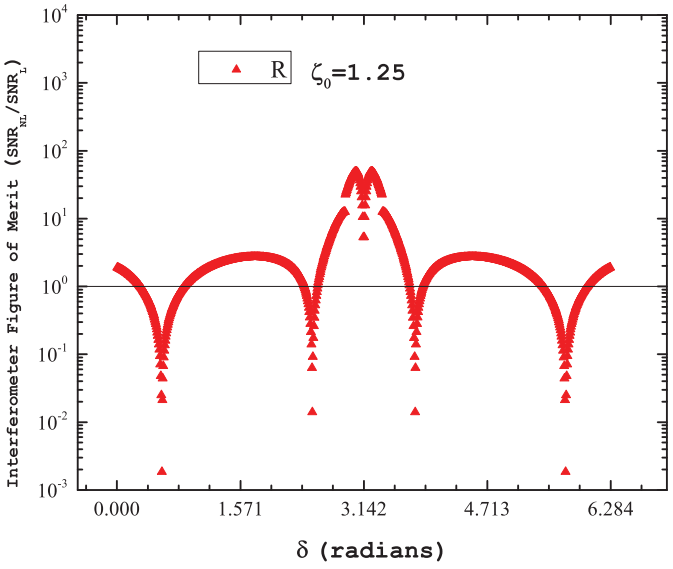

Figure 3.35. Interferometer performance for $\zeta = 1.25$.

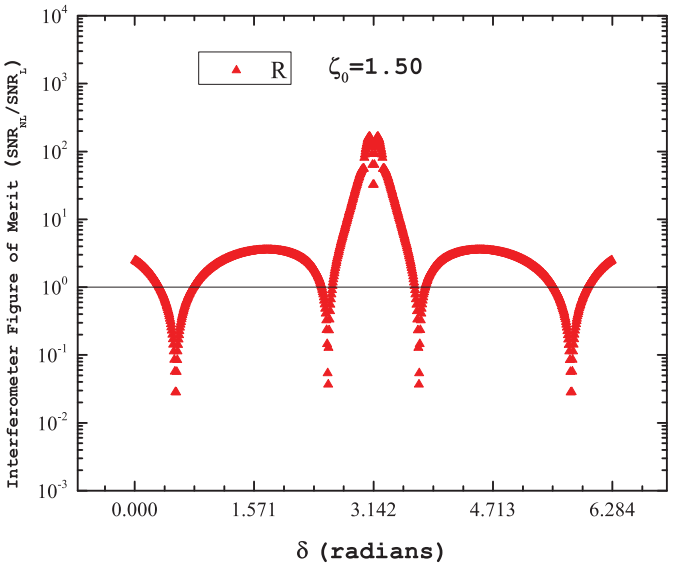

Figure 3.36. Interferometer performance for $\zeta = 1.50$.

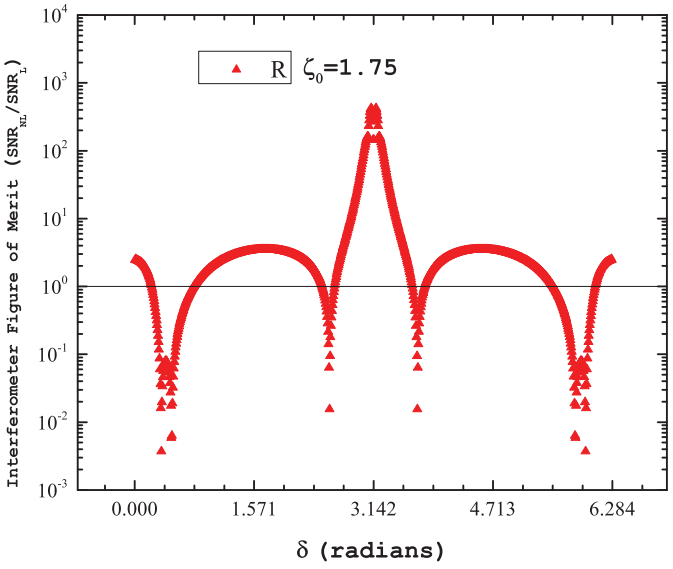

Figure 3.37. Interferometer performance for $\zeta = 1.75$.

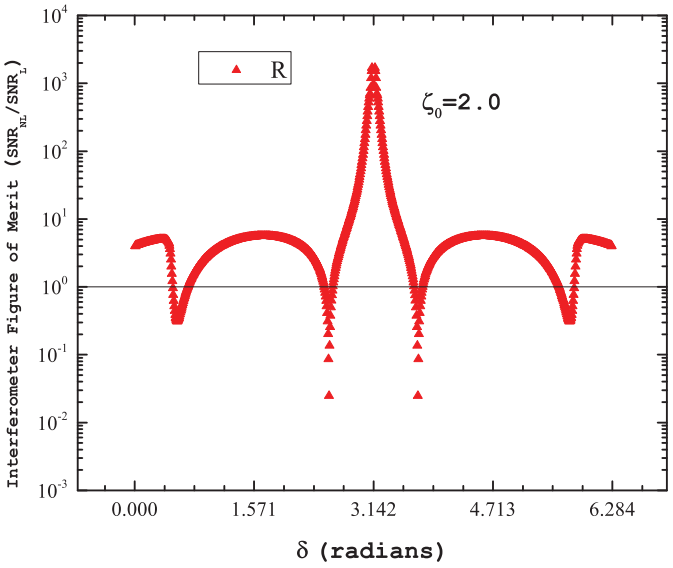

Figure 3.38. Interferometer performance for $\zeta = 2.0$.

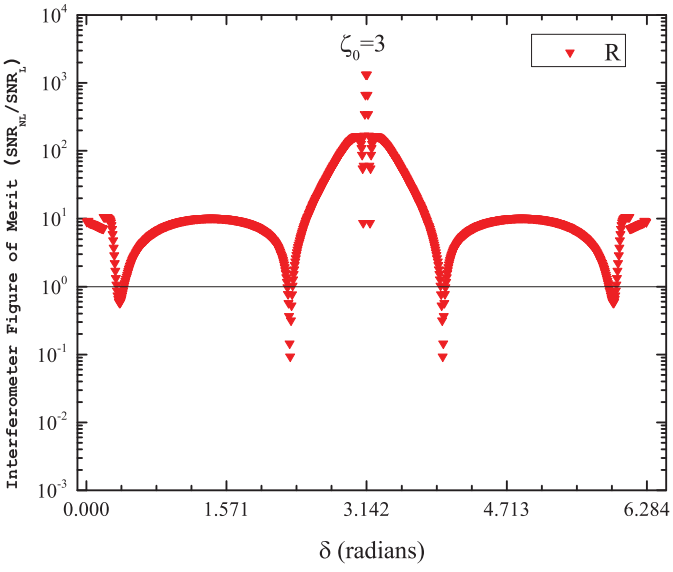

Figure 3.39. Interferometer performance for $\zeta = 3.0$.

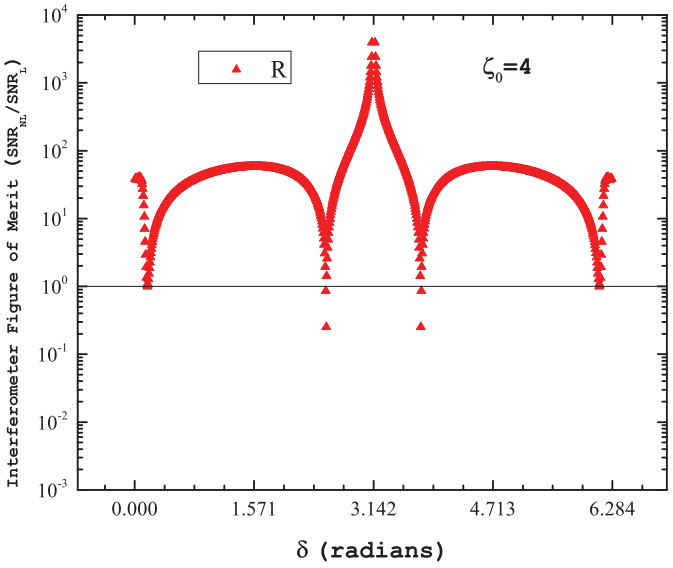

Figure 3.40. Interferometer performance for $\zeta = 4.0$.

To reiterate, as seen from figures 3.32 to 3.40, the performance ratio $\mathcal{R}$ increases with increasing interaction length ζ_0. We plot this dependence in figure 3.41. We see that apart from $\zeta_0 = 0.5$, there is a clear improvement in the performance of the nonlinear interferometer over a linear interferometer. To generate this plot, we choose a region where the graph is reasonably flat, i.e., we avoid regions close to $\delta = \pi$.

In figure 3.42, we plot the value of $\delta = \delta_{max}$ for which maximum performance is obtained. For the most part, best performance is obtained at an angle of about $\delta_{max} = 1.75$ radians. Operational regions were chosen by hand as long as they were continuous and were away from $\delta = \pi$.

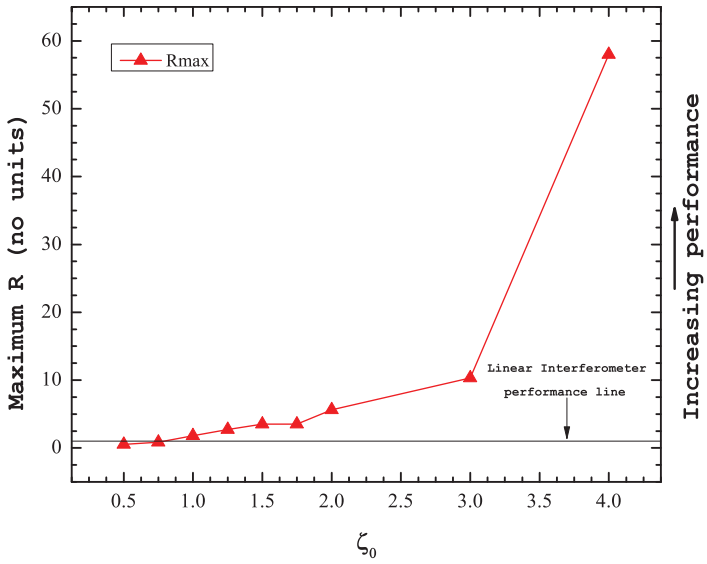

Figure 3.41. Interferometer performance as a function of characteristic length ζ_0. It can be clearly seen that the performance increases as the interaction length increases. The straight line indicates the region where nonlinear and linear interferometer performance are the same. Points above the line indicate performance greater than a linear interferometer and points below the line indicate performance worse than a linear interferometer.

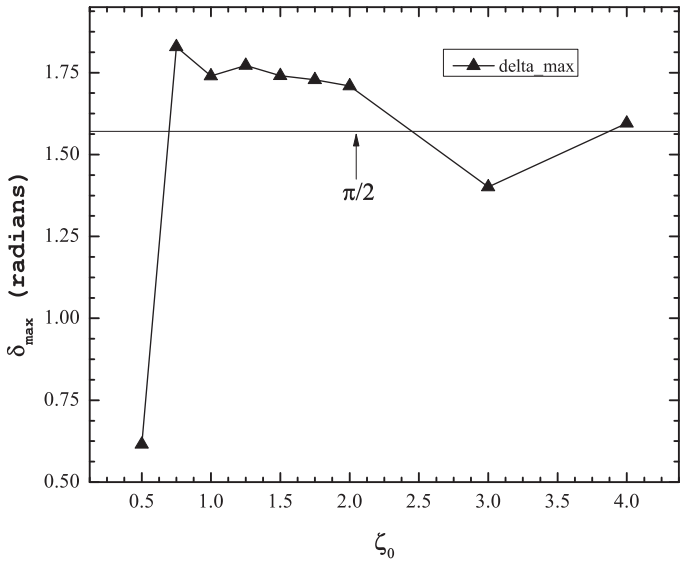

Figure 3.42. The interferometer phase angle δ at which its performance is a maximum as a function of characteristic length ζ_0.

PART II: COHERENT INTERACTION OF LIGHT AND CS ATOMS

4. INTRODUCTION

The experimental development of long-distance quantum communication is of much interest as it would allow secure transmission of messages and faithful transfer of unknown quantum states [48]. Current research is focused on using photons as the information carrier because their interaction with matter in the communication channel can be made very weak. However due to decoherence, quantum communication fidelity decreases exponentially with the length of the transmission line. A possible solution to alleviate the loss of fidelity is to use quantum repeaters [49], [50]. To implement this, some form of quantum memory is required. Since it is difficult to store photons for long times, a possible approach to a practical quantum memory is to reversibly transfer the quantum information carried by photons into a non-photonic form. Coherently prepared atomic gases [51], is one possible candidate to achieve this conversion. Technology is limited by the availability of laser sources and detectors at the single photon level that are not noisy. With these constraints, quantum memory research is currently done at the 750nm 850nm wavelength in alkali metal vapors.

Atom-Photon conversions involve converting the photonic state to an *Atomic Spin wave* by the interaction of a *write* laser beam with a gas of coherently prepared atoms and recovering the photonic state after a pre-determined storage time. The photonic state represents the information carried by a collective photon mode or by a single photon. A photon has a set of observables given as energy, linear momentum and angular momentum. Each of these attributes can be preserved in the collective atomic system and can be faithfully recovered or modified.

The basic principle involves destruction of a *write* photon whose energy is used to flip the spin of a single atom in a ground state hyperfine level by pushing it to the next level in the same manifold. Recovery of the photonic state is accomplished by a *read* laser that reverses this process. This is the atom-photon conversion process

and the system is in an entangled state. We investigate atom-photon conversion by stimulated Raman scattering i.e., reversible storage and retrieval of quantum states of light in a coherently prepared atomic gas of hot cesium atoms. Our investigation is based on the physics of three-wave mixing. The efficiency of conversion from atom to photon can in principle reach 100 percent and in theory, the conversion process can be noiseless [52].

5. PHYSICAL PRINCIPLES

In this chapter, we will discuss the physics of atom-photon conversion. First, we discuss basic light-matter interaction and the feature of superposition of states followed by the atomic structure we choose to work with, and finally present a brief introduction to two schemes that are used to build up atomic coherence and their relative merits and present a possible solution to alleviate the problems associated with the schemes discussed in the previous section.

5.1 Physics of Light-Matter Interaction

5.1.1 Principle of Superposition of States

Quantum mechanics gives us the ability to calculate the probability that a physical event would occur. We describe a path by which an event occurs by a wave function. The wave function has a probability amplitude associated with it. The square of the amplitude gives us the probability of the event occurring. If there is more than one possible pathway for an event to occur and the paths are in principle indistinguishable, the probability for that event to take place can be obtained by summing the probability amplitudes corresponding to the various paths. Taking the square of this sum gives us the probability of the event. In other words, quantum mechanics allows a system to be in a *superposition of states*.

The important concept of superposition of states can also be applied when one tries to determine the quantum state of a physical system. If after some evolution, the system can end up in several states which are indistinguishable, the system is in a coherent superposition of all the possible states. Consider an atomic system with three energy levels $|g\rangle$,$|m\rangle$ and $|e\rangle$ as shown in figure 5.1.

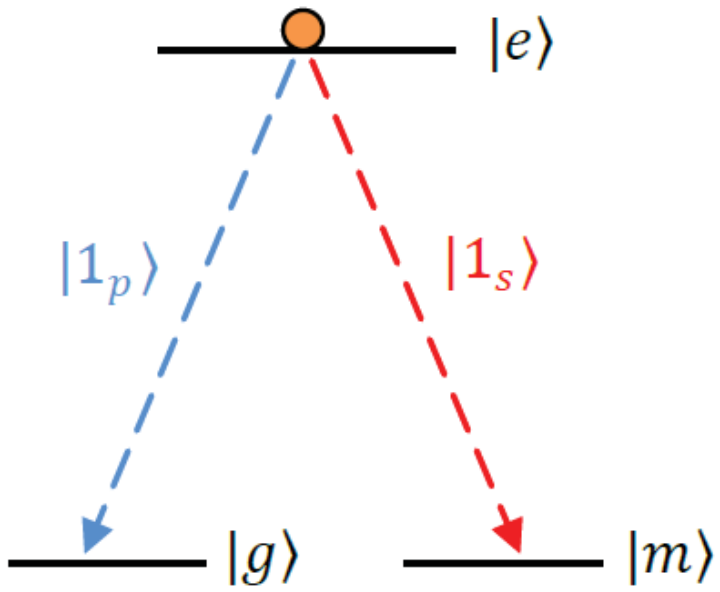

Figure 5.1. A three level Lambda arrangement of energy levels.

Assume that an atom that is initially in an excited state with two decay paths. After the atom decays to the ground states and emits a photon, the state of the system composed of the atom and the emitted photon can be written as

$$|\Psi\rangle = \frac{1}{\sqrt{2}}\{|g\rangle|1_p\rangle + e^{i\phi}|m\rangle|1_s\rangle\}$$
$$|\Psi\rangle = \frac{1}{\sqrt{2}}\{\hat{a}_p^\dagger|0\rangle\}|g\rangle + e^{i\phi}\{\hat{a}_s^\dagger|0\rangle\}|m\rangle, \tag{5.1}$$

where each term stands for the final state of the atom and the emitted photon for the two possible decay paths. Incidentally, the above arrangement of energy levels is called a Λ (Lambda) system. The creation of a light-matter superposition state is also known as an entangled state.

5.1.2 Atomic Coherence

Atomic Coherence is defined as the superposition of ground states $|g\rangle, |m\rangle$ of an atomic system such that the atomic state $|\Psi\rangle_{atom} = \alpha|g\rangle + \beta|m\rangle$. Mathematically, it is given by the off-diagonal elements of the density matrix (representation) in the bare state basis, of the atomic system. This is a very important concept that is central to achieving atom-photon conversion. In this process, we create entangled states of photons and atoms. The states $|g\rangle, |m\rangle$ are chosen such that they are dipole disallowed. Suppose we have an ensemble of atoms in a Lambda configuration, we can define an operator for the atomic system as

$$\hat{S} = \frac{1}{\sqrt{N_a}} \sum_i |g_i\rangle\langle m_i|, \tag{5.2}$$

We now call $\hat{S}$ operator the *Spin Wave*. This operator quantifies atomic coherence. We can see readily that: $\hat{S}|m_i\rangle = |g_i\rangle$. Hence $\hat{S}$ may also be considered an atomic demotion operator where $\langle\hat{S}\rangle \neq 0$. In the context of a real atom, usually, $|g\rangle$ and $|m\rangle$ are ground state hyperfine levels (discussed in the next section) and hence $\hat{S}$ is also known as the spin-flip operator as the spin quantum number of the atom changes. The index i is a label attached to each atom and the sum indicates that the spin-flip operator describes the *collective atomic system* involving many atoms.

5.2 The Cesium Atomic System

As mentioned previously, storage of light is essential to implement quantum memory. An atomic gas is an attractive alternative to accomplish this because of less decoherence when compared with solid state media. This is partly because of the near continuum distribution of energy levels in solids. Equation 5.2 is the simplest form of coherent superposition. This is realized in a real atomic system by choosing atoms with two ground states that couple to a common excited state each via one of two light fields as shown in figure 5.3. The important point to note is that all other energy levels are far enough away that their influence can be neglected. Then, these

atoms can be thought of as three-level-systems, commonly called Λ-systems. Of the atomic systems available, alkali atoms are the simplest systems (experimentally) that can be used in a Λ configuration (in our experiments we choose to work with a system comprising of the $F = 3, 4$ ground states and an excited state such as $F' = 4$. Note that $|g\rangle$ and $\langle m_i|$ are long lived (compared to the timescale on which our experiments take place) states of the systems.

We choose to work with the $6^2S_{1/2}$ - $6^2P_{3/2}$ energy levels (referred to as the D2 Line in spectroscopic literature) of the Cesium atomic system. The energy levels of this system can be accessed by light of wavelength 852 nm. The specifics of the laser system will be discussed in a later section. A compendium of physical and spectroscopic properties of Cs can be found in [53].

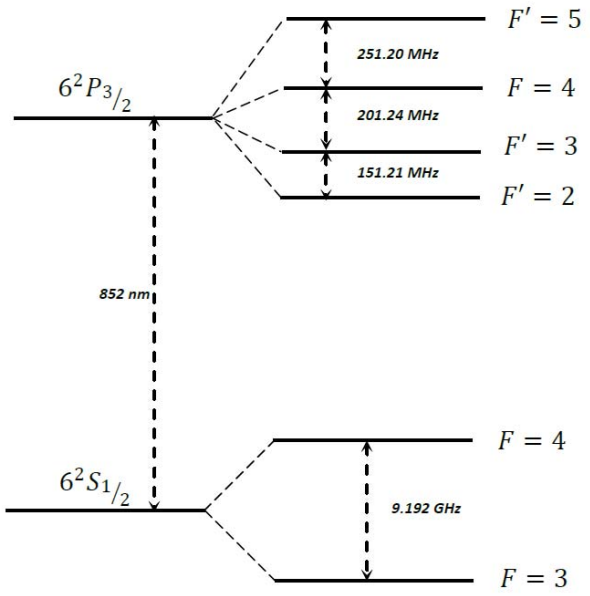

Figure 5.2. The Cesium D2-Line energy level structure.

5.3 Preparation of Atomic Coherence

Experimental configurations for atom-photon conversions independent of each other in terms of the physics, but follow different implementations. The essential difference lies in how the atoms are placed in a coherent superposition of ground states. This can be accomplished by either resonant phenomena such as *Electromagnetically Induced Transparency (EIT)* [54] or via far off-resonant *Raman* processes [48]. In all these experiments, it is essential to prepare the atoms in a ground state i.e in $|g\rangle$ or $|m\rangle$ as a prelude to building up atomic coherence. In an experiment, the accessible part of the atom-photon superposition state are photons. In order to exert control over the evolution of the collective atomic wavefunction via light, we have to build up the coherence as opposed to allowing thermal fluctuations to redistribute atoms. There is no definite phase relationship between atomic wavefunctions in case of thermal distribution and hence a thermal redistribution does not make a coherent state. Ground state preparation of the atomic system is accomplished by shining a strong resonant laser on the atomic ensemble coupling the upper ground state with an excited state and allowing the atoms to spontaneously decay to the next hyperfine state in the same manifold. This is called optical pumping [55].

Next, atomic coherence is generated by a *write* process (as in writing the quantum state of light). EIT based writing has been demonstrated by [56, 57]. In an EIT scheme, a Λ energy level atomic system interacts with two resonant lasers. A strong laser called control A_c, couples the upper ground state $|m\rangle$ to an excited state $|e\rangle$ and a weak laser, called probe or write, A_p couples the lower ground state $|g\rangle$ to $|e\rangle$. It is seen that the probe absorption vanishes at the excitation energy of $|e\rangle$. This unusual effect results from the quantum coherence between two atomic transitions created by the strong control field applied to one of the two transitions and a weak probe field applied to the other. The origin of these effects has been explained in terms of superposition states induced in a multi-level atom driven by two laser fields. The control laser *dresses* the states it couples to into a so called bright and dark state. In the dressed state basis, the probe field absorption vanishes [58].

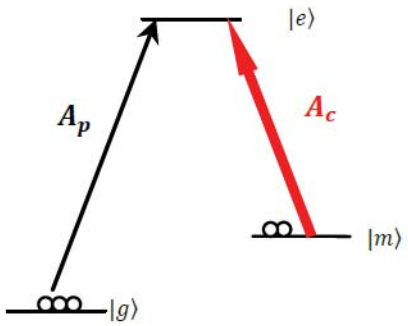

Figure 5.3. EIT configuration in a Lambda system.

In EIT centric studies the emphasis is on investigating what happens to the probe field and not on the atomic system. When the atomic density matrix is calculated, it is done to study the refractive properties of the medium from which propagation of the probe field is studied. For any study of using atoms in quantum computing (quantum registers) [59], the point that the coherence (off-diagonal) terms are non-zero deserves more attention. One of the drawbacks of using EIT in the write process lies in the fact that it is a resonant phenomenon. Hot atoms constitute a Doppler medium due to the Maxwell-Boltzmann distribution of atomic velocities. This means, a weak write beam can be incoherently scattered by closely spaced velocity classes, i.e. photons can be lost due to spontaneous scattering which would be a problem for low intensity write beams used in typical quantum level experiments.

To alleviate absorption issues associated with resonant phenomena, we can look towards off-resonant processes. How can an off-resonant process make coherent preparation possible? The principle is that spontaneously scattered light acts as a seed for stimulated emission [60,61]. In brief, a spontaneously emitted photon, after a series of emissions and absorptions propagates through the atomic sample building up coherence in a spatially narrow pencil like geometry in the direction of the propagation of

the initial light wave. Based on this theory a technique to prepare a coherent superposition of atomic states is by an off-resonant process was demonstrated by [48]. In this scheme, after the initial pure state preparation, a weak, off-resonant write laser incident on the $|g\rangle$ level transfers atoms to the $|m\rangle$ level by a spontaneous Raman scattering. "Reading" is accomplished by the reverse process. Although, losses are significantly lower, the interaction strength is also lower than a resonant process. To compensate, the atomic density must be increased. Although the experiment in [48] was performed in a cold ensemble of laser cooled rubidium atoms, subsequent experiments have demonstrated the success of the scheme in hot atoms [62–64] and in cold atoms [65]. A natural advantage of this process lies in the reading process (the atomic spin wave is converted back to a photon) which can be done at a different frequency than the write process.

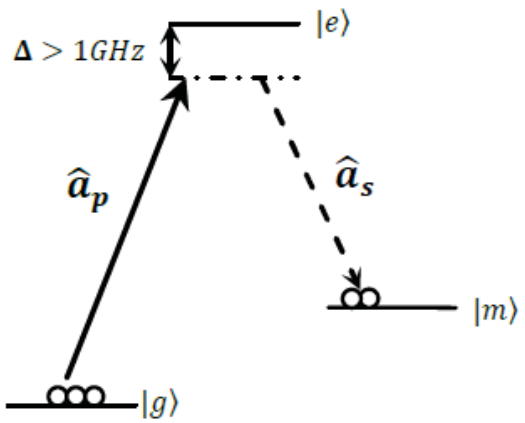

Figure 5.4. Preperation of coherence by spontaneous Raman scattering.

Hot or cold systems have their unique disadvantages and advantages. The main experimental limitation in either case is decoherence or dephasing of the atomic spins [64]. This is an important characteristic of a collective system where there is a unique 1-1 mapping between a scattered photon and a spin flipped atom. In this context, if the atomic spins flip for any reason other than their interaction with the read/write

lasers, this 1-1 correspondence is lost which in turn implies a loss of information. It is the mechanism of dephasing that is different in hot versus cold systems.

In addition, there is always the problem of quantum noise in both schemes. By noise we mean the creation of a photon which has random polarization and is not associated with a corresponding spin flip. In theory, to simplify calculations, we assume that atoms are moving along the beam and that the same velocity class of atoms are being addressed by the control and probe i.e a one dimensional theory. But this is not the case in real experiments. In off-resonant spontaneous Raman experiments, although coherence is built up from spontaneous scattering, the process is essentially noisy. We discuss this in the next chapter.

The main causes of decoherence in a hot atoms vapor cell are wall atom collisions (inelastic), atom-atom collisions and a prepared atom drifting out of the interaction areas serviced by the read/write beams [64, 66]. The collision issues have been alleviated to a certain extent by using paraffin coated cells and buffer gases. While an atom trap containing a cold cloud of atoms seem to solve the collision related decoherence problems, the external magnetic field required to trap the atoms interact with the atomic spins causing inhomogeneous broadening of the ground state and their dephasing [67]. Cost, size and complexity issues also go against a cold atom setup. With this in mind, we have opted to work with hot atomic gas ($T = 50°\mathrm{C}$). A possible solution to achieve high photon-photon conversion efficiency would be to use a stimulated process. The main advantage is that this process is in theory noiseless. We discuss this in detail in the next chapter.

5.4 Atom-Photon and Photon-Photon Conversion in Raman Scattering

In this chapter, we discuss atom to photon conversion and photon to photon conversion in Raman scattering. First we review Raman interactions in a three level Λ system, then we discuss a parametric Raman amplifier, next we discuss atom-

photon conversion by stimulated Raman scattering (when the pump field is large) and finally we discuss photon-photon conversion when the spin wave is large.

In all subsequent discussion, light and the atomic system interactions are given by the following figure:

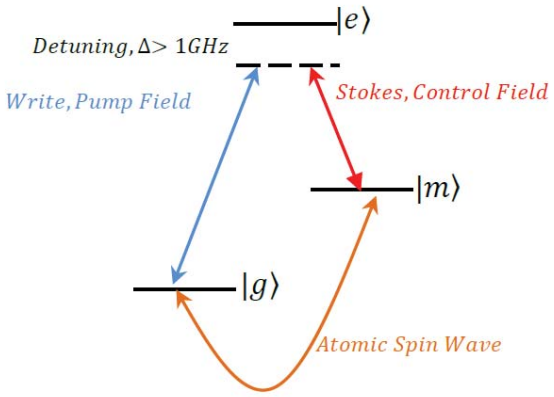

Figure 5.5. The Pump (Write) field couples levels $|g\rangle$ *and* $|e\rangle$, the Control (Stokes) couples levels $|m\rangle$ *and* $|e\rangle$. Optical and spin fields can be either weak (represented by operators) or strong (represented by amplitudes).

5.4.1 Raman Interactions in a Λ System

A Raman interaction is a non-resonant, nonlinear process where a photon of energy $\hbar\omega_1$ is destroyed and simultaneously a photon of energy $\hbar(\omega_1 - \Omega_R)$ is generated [68]. The difference in energy between the two appears as a quantum of Raman excitation $\hbar\Omega_R$. When the energy of the emitted photon is less than the energy of the incident photon, the process is called Stokes scattering. In a Stokes process, the internal energy of the medium increases. The reverse process is called anti-Stokes scattering where the energy of the scattered photon is higher than the energy of the incident photon.

The interaction hamiltonian for a Raman process in a Λ system shown in fig (5.5) was given by Duan *et al.*, in [48] as

$$\hat{H}_R = \imath\hbar\eta\hat{a}_p\hat{a}_s^\dagger\hat{S}^\dagger - \imath\hbar\eta\hat{a}_p^\dagger\hat{a}_s\hat{S}, \tag{5.3}$$

$\hat{S}$ is the spin-flip operator that describes the collective atomic system, $\hat{a}_s, \hat{a}_p$ are operators that describe the light fields and $\eta = g_{eg}g_{em}^*\sqrt{N_a}/\Delta$ where g_{eg}, g_{em} are coupling coefficients between the light and atomic states and Δ is the detuning of the light fields from the upper excited state. Here we are considering a single velocity class of atoms and that information is in Δ, if effects of additional velocity classes are to be considered, we have to convolve the result with a Doppler velocity distribution. Conventionally, the photon fields $\hat{a}_s, \hat{a}_p$ are called signal and idler respectively. In a semi-classical treatment, $\eta\hat{S}$ is usually treated classically and lumped together as one term. This is form of the Hamiltonian is used to describe parametric process, where the interacting light fields do not change the energy of the medium. Figure 5.5 shows pump,stokes and spin waves that constitute the interaction Hamiltonian given in equation 5.3. We can analyze this Hamiltonian under a few special conditions which will correspond to different physical situations.

5.4.2 The Parametric Raman Amplifier

A parametric amplifier can be described by the following interaction Hamiltonian [69]:

$$\hat{H}_R = \imath\hbar\eta\hat{a}_p\hat{a}_s^\dagger\hat{a}_i^\dagger - \imath\hbar\eta\hat{a}_p^\dagger\hat{a}_s\hat{a}_i, \tag{5.4}$$

This represents a non-linear process where a photon in the pump field $\hat{a}_p$ is destroyed and two photons are created in the $\hat{a}_s$ and $\hat{a}_i$ modes. The subscripts stand for pump, signal and idler. Note that the energy structure of the medium is not modified and the only role played by the medium is one of a passive facilitator of mixing the optical fields. In a Raman amplifier however, the energy of the medium is modified and this

results in amplifying a Stokes field with gain being proportional to the pump intensity. Notice the similarity in the structure of the interaction hamiltonian discussed in the previous section and the parametric amplifier hamiltonian.

The output states of the signal and idler fields are given as

$$\begin{aligned} \hat{a}_s^{out} &= \hat{a}_s \cosh|\eta A_p|\tau + e^{i\varphi_p}\hat{a}_i^\dagger \sinh|\eta A_p|\tau \\ \hat{a}_i^{out} &= \hat{a}_i \cosh|\eta A_p|\tau - e^{i\varphi_p}\hat{a}_s^\dagger \sin|\eta A_p|\tau, \end{aligned} \tag{5.5}$$

A Raman amplifier is described by replacing the idler field of equation 5.4 with an atomic spin wave. In other words, the spin wave takes the role of the idler field. Consider a Raman system with a strong pump field where we make the replacement $\hat{a}_p \rightarrow A_p$, i.e., the pump field is intense and hence the operator average can be represented by a classical amplitude. In the absence of a Stokes field we can write the hamiltonian 5.3 as [52]

$$\hat{H}_R = \imath\hbar\eta A_p \hat{a}_s^\dagger \hat{S}^\dagger - \imath\hbar\eta A_p^* \hat{a}_s \hat{S}, \tag{5.6}$$

The output states of the Stokes and idler fields are given below [52]. (Note the difference in designation of the subscripts when comparing equations in 5.5):

$$\hat{S}^{out} = \hat{S}\cosh|\eta A_p|\tau + e^{i\varphi_S}\hat{a}_s^\dagger \sinh|\eta A_p|\tau \tag{5.7}$$

$$\hat{a}_s^{out} = \hat{a}_s \cosh|\eta A_p|\tau - e^{i\varphi_S}\hat{S}^\dagger \sin|\eta A_p|\tau, \tag{5.8}$$

The above equations describe a Raman amplifier operating under high gain conditions.

5.4.3 Atom-Photon Conversion: Strong Pump Regime

As discussed in chapter 2, stimulated emission is seeded by spontaneous scattering. The motivation for this idea stems from the basic principle that the probability of emission into a particular mode is increased by a factor of *n+1* if there are already n

photons in that state. Suppose there is a strong Stokes field injection and the pump field is made very weak, we can rewrite equation 5.3 as

$$\hat{H}_R = \imath\hbar\eta\hat{a}_p A_s^* \hat{S}^\dagger - \imath\hbar\eta\hat{a}_p^\dagger A_s \hat{S}, \tag{5.9}$$

The evolution of the operators in the Heisenberg picture is given as [52]:

$$\hat{a}_p^{out} = \hat{a}_p \cos|\eta A_S|\tau + e^{i\varphi_S}\hat{S}\sin|\eta A_S|\tau \tag{5.10}$$

$$\hat{S}^{out} = \hat{S}\cos|\eta A_S|\tau - e^{i\varphi_S}\hat{a}_p \sin|\eta A_S|\tau, \tag{5.11}$$

Here $e^{i\varphi_S} \equiv \eta A_S^*/|\eta A_S|$. The η term depends on the coupling coefficients between the atom and the field while the A_S term is the classical amplitude of the injected Stokes field. When the argument of the cosine term is $\pi/2$ and when $\varphi_S = 0$ we have $\hat{a}_p^{out} = \hat{S}$ and $\hat{S}^{out} = -\hat{a}_p$. (There is no particular significance to the negative sign.)

This is called atom-photon conversion and vice versa. Equation 5.11 tells us that given an initially prepared atomic system the presence of a strong Stokes field converts the pump photon into an atomic coherence with very high efficiency. Likewise Equation 5.10 describes the reverse process. Note that in the reverse process the Stokes field can be of a different frequency.

5.4.4 Photon-Photon Conversion: Strong Spin Wave Regime

We revisit the fact that it is necessary to build atomic coherence to achieve photon photon conversion. We have also discussed three different schemes that can be used to build atomic coherence.

Suppose the spin wave is very large in equation 5.3, the interaction Hamiltonian can be written as

$$\hat{H}_R = \imath\hbar\eta\hat{a}_p\hat{a}_s S^* - \imath\hbar\eta\hat{a}_p^\dagger\hat{a}_s S, \tag{5.12}$$

We can then treat the spin wave as a classical amplitude. The corresponding output operators for the Stokes field and pump fields will become

$$\hat{a}_s^{out} = \hat{a}_s \cos|\eta S|\tau - e^{i\varphi_S}\hat{a}_p \sin|\eta S|\tau, \tag{5.13}$$

$$\hat{a}_p^{out} = \hat{a}_p \cos|\eta S|\tau - e^{i\varphi_S}\hat{a}_s \sin|\eta S|\tau, \tag{5.14}$$

Here $e^{i\varphi_S} \equiv \eta S^*/|\eta S|$. The η term depends on the coupling coefficients between the atom and the field while the S term is the amplitude of the spin wave. When the argument of the cosine term is $\pi/2$ and when $\varphi_S = 0$ we have $\hat{a}_p^{out} = \hat{a}_S$ for the creation of a pump photon from a Stokes photon as shown in figure 5.6.

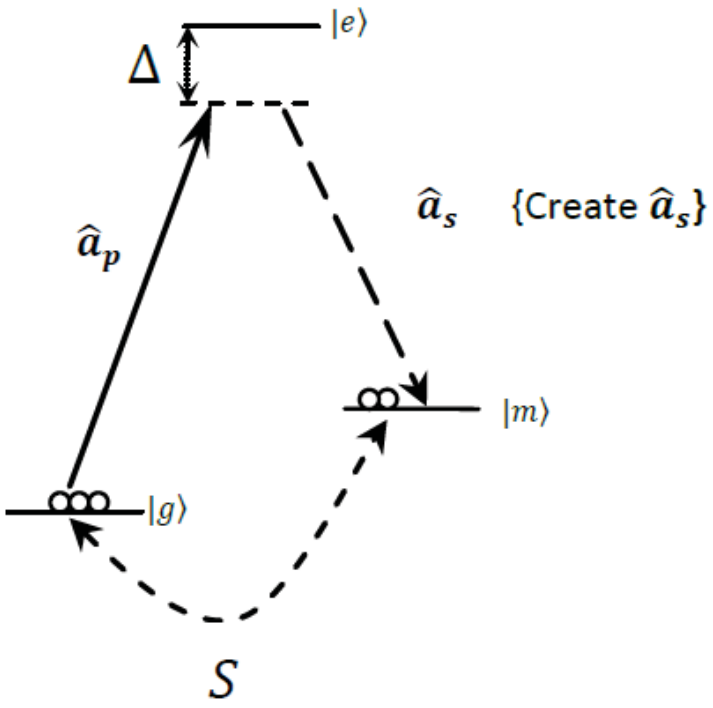

Figure 5.6. Converting a pump photon to a Stokes photon

The result we are interested in given by $\hat{a}_s^{out} = -\hat{a}_p$ describes the creation of a Stokes photon from a pump photon. This can be done with a controllable recovery time. In other words, we can create a large atomic spin wave and after a specific

time delay, recover the photon field in the Stokes mode. In traditional light storage experiments based on resonant phenomena such as EIT, the spin coherence is converted back into a light pulse that has the same frequency as the weak input probe pulse, so there is no frequency conversion. The same field is stored and recovered. Our project is an experimental investigation of frequency conversion by mapping the spin coherence back into light at a different frequency. This is done by injecting a Raman field that is far off-resonant, which means the injected field is not absorbed by the medium and can be made weak, as opposed to a resonant control field in a traditional light storage experiment.

6. EXPERIMENTAL ARRANGEMENTS

6.1 Generating Atomic Coherence by EIT

Electromagnetically Induced Transparency (EIT) is a quantum interference effect where the absorption of a weak resonant field is canceled by the introduction of a strong coupling field. This effect results in the transmission of light through an otherwise opaque medium [70]. Fleischhauer and Lukin [71, 72] developed the theory of light storage in atomic media using the EIT effect and it was experimentally demonstrated by Phillips *et al.*, [56] in Rubidium. If a weak light field and a strong control light field are interacting with an atomic system, the quantum field can be converted fully into atomic coherence by adiabatically changing the control field intensity and pulse shape [71]. Fleischhauer and Lukin proposed a new quantum field to describe the physics of photon-atom conversion called the *dark-state Polariton*. It is basically an operator that is a linear superposition of the an atomic spin wave (eigenstates of $\hat{S}$) and the weak quantum field that describes the light. The main result of the theory and experiment is that this conversion from photon to atom is reversible and the storage time can be controlled by changing the intensity of the control beam.

6.1.1 Continuous Wave EIT

In a typical EIT experiment, a strong control laser and a weak probe laser interact with a lambda system as shown in figure 5.3. The control laser is frequency locked and the probe laser is scanned across the various excited state energy levels. When the two photon resonance condition is met, the probe transmission is increased dramatically (i.e the medium becomes transparent). The point relevant to our experiment is that under conditions of EIT, atomic coherence is generated and by maximizing the

EIT signal, we enhance the generation of atomic coherence. With this in mind, we performed CW EIT experiments to obtain conditions for which enhanced atomic coherence was generated. In the following sections, we discuss important experimental parameters and explain our setup in detail.

6.1.1.1. Cesium Vapor Cells

Metallic cesium (Cs) is highly toxic and reacts violently when exposed to moisture. It is common practice in atomic physics experiments to use vapor cells. These are evacuated glass cells filled with a small quantity of Cs. Under conditions of low pressure (typically 10^{-6} Torr), Cs vaporizes and constitutes a dilute system, i.e. Cs-Cs interactions can be ignored for most purposes. Our cylindrical vapor cells were typically 10cm long and 2.5cm radius. We employed three different kinds of vapor cells, a bare cell consisting of Cs alone, a buffer gas cell filled with Ne at 40 Torr and a paraffin coated cell.

Figure 6.1. The paraffin cell used in our experiment.

From Daniel Steck's Cs D Line data compendium [53], we can calculate the vapor pressure of Cs for as

$$\log_{10} P_v = 8.22127 - \frac{4006.048}{T} - 0.00060194T + 0.19623 \log_{10} T, \tag{6.1}$$

where P_v is the vapor pressure of Cs and T is the temperature in Kelvin.

In detailed studies by Klein *et al.*, the generation of atomic coherence is greatly enhanced by increasing the number density of atoms in the cell [73] and this can be calculated from the vapor pressure at specific temperatures. A theoretical plot is given in figure (6.2).

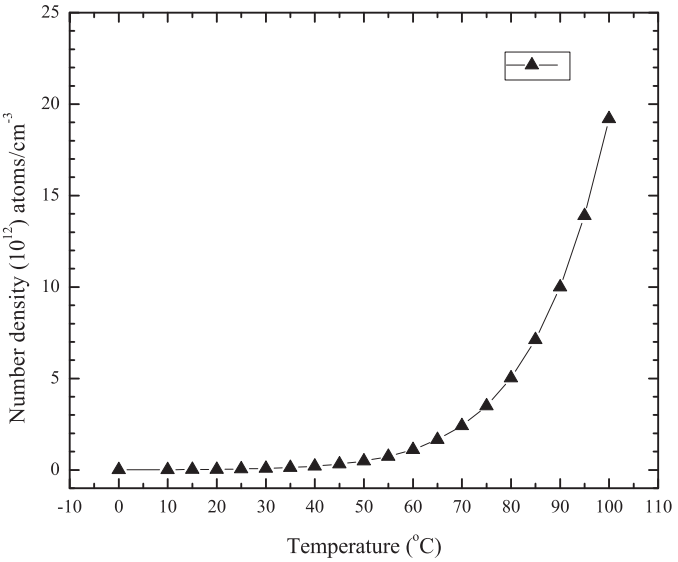

Figure 6.2. Theoretical plot of number density of Cs atoms with temperature.

Another important factor in atomic coherence experiments is the time atoms spend in the laser beams. Assuming a sufficiently dilute system, and a Maxwell-Boltzmann

distribution of atoms, the most probable atomic speed and average speeds are given as [74]

$$v = \sqrt{\frac{2kT}{m_{Cs}}} \tag{6.2}$$

$$\langle v \rangle = \sqrt{\frac{8kT}{\pi m_{Cs}}}, \tag{6.3}$$

For our system at $T = 60°\text{C}$, $\langle v \rangle \approx 250$ m/s. Assuming a typical beam diameter of 2.0 mm, an atom exits the laser beam in about 8μs. This is a serious limitation in atomic coherence experiments because while the system may be coherently prepared, recovery of information is hampered due to loss of atoms from the laser beams. One way to alleviate this problem is to increase the beam diameter, but this comes at the cost of reduced light intensity. To slow down or limit the atoms from escaping the beam, it was suggested that an inert buffer gas be used and a detailed study was performed by Mikhailov [75]. We used a cell filled with 40 Torr Ne buffer gas. The number density of Ne can be calculated from the ideal gas law gives $n_{Ne} \approx 1.3 \times 10^{18}$ cm^{-3}.

The diffusion time of the Cs atoms change due to elastic collisions with Ne and this has been studied in great detail, for example in [76]. The diffusion time is given as $t = r^2/4D^2$ where r is the beam radius and D is the diffusion coefficient [77] . The diffusion coefficient is given as [78]:

$$D = \frac{1}{3}\langle v \rangle \lambda_m \tag{6.4}$$

$$\lambda_m = \frac{1}{n\sigma_{CsNe}}, \tag{6.5}$$

where λ_m is the mean free path n is the number density of Cs, $\langle v_\mu \rangle \approx 600$ m/s is the velocity of the reduced mass of the Cs-Ne system and $\sigma_{Cs-Ne} = 2.871 \times 10^{-14}$ cm^2 is the collisional cross section calculating using the radius of the Cs-Ne molecule given in [79–81]. Using this data, we can calculate $D = 0.168$ cm^2/s and therefore the modified diffusion time is $t = 0.6$ ms.

In addition to loss of atoms from the beam, atoms can depolarize due to collisions with the walls of the cell. This is referred to dephasing of spins and is another undesirable effect. Collisions with walls can result in redistribution of atoms occupying different closely spaced energy levels and consequently, the phase coherence built up when the atomic system interacts with light is destroyed. It was discovered long ago [82] that coating the walls of the vapor cell with paraffin wax minimized depolarization. More recent detailed studies in the context of EIT and generation of atomic coherence have established paraffin coatings as standard technology [83]. We used a paraffin coated cell for the main experiment.

6.1.1.2. Experiment Setup

The complete setup is shown in figure 6.3. We employed two home made 852 nm frequency stable diode lasers in the Littrow configuration [84, 85] that operate on the Cs D2 line. The probe laser was was locked to the $|F = 3\rangle \rightarrow |F' = 4\rangle$ transition at room temperature by standard frequency modulation (FM) spectroscopy. The probe beam had a diameter of 2.5 mm and was linearly polarized by employing a half-wave plate and a polarizing beamsplitter. The orthogonal polarization was used by the locking setup. The laser power was attenuated to 500μW for use in the main experiment. The control laser was locked to the $|F = 4\rangle \rightarrow |F' = 4\rangle$ transition at room temperature by FM spectroscopy. This laser had a power of about 10mW and was linearly polarized and expanded to a diameter of 1cm.

The interaction chamber consists of a paraffin coated Cs cell enclosed in a custom made cylindrical three layer μ-metal shield to keep out stray magnetic fields. Magnetic shielding is necessary to ensure that we work with one lambda system as opposed to a manifold of such systems generated by Zeeman interactions of the atoms with external magnetic fields. The entire chamber was wrapped in a multi-stranded resistive heating wire and covered in aluminum foil. The chamber was maintained at a constant temperature of about 60°C. The laser beams were first made orthogonally polarized

to each other and then superposed on a polarizing beamsplitter in a co-propagating configuration. The polarizations were made orthogonal to ensure that the probe laser can be extracted by an output polarizing beamsplitter. We used appropriate lenses to shape the beam waists of both lasers. Before entering the interaction chamber, both lasers were tapped off by a small glass plate (microscope cover slip) and sent into an 8GHz FSR Burliegh SA100 Fabry-Perot Spectrum Analyzer to monitor their mode quality during the course of the experiment. After exiting the interaction chamber, the signal (probe) beam was separated out by a high quality polarizing beamsplitter (extinction factor of 10^6) and the light was detected by a homemade detector based on the fast photodiode FFD100 made by $EG\&G$[1]. We observed the electronic signals on an oscilloscope (Textronix TDS2014-B)[2].

6.1.1.3. Observation of CW EIT signal

To observe CW EIT signals, we scanned the probe laser between the $|F = 3\rangle \rightarrow |F'\rangle$ transitions, while the control laser was locked to the $|F = 4\rangle \rightarrow |F' = 4\rangle$ transition. The interaction chamber was heated up to stable temperatures of between 50°C up to 75°C. When the control laser was blocked, we observed a peculiar shape for the doppler broadened absorption that seemed to be unique only for the paraffin coated cell as shown in figure 6.4. This does not happen with either a bare cell, or with the buffer gas cell. With the buffer gas cell, the observed fluorescence (by an inexpensive Sony Handycam with nightshot mode)was much less brighter than either the bare cell or the paraffin cell. This indicates that the atoms in the buffer gas cell are spending more time in the laser beam path before diffusing out.

[1]Dark current 5nA, rise time 2ns, bandwidth of 150MHz.
[2]Details of all the home made electronics and other devices including magnetic shielding can be found in the appendices.

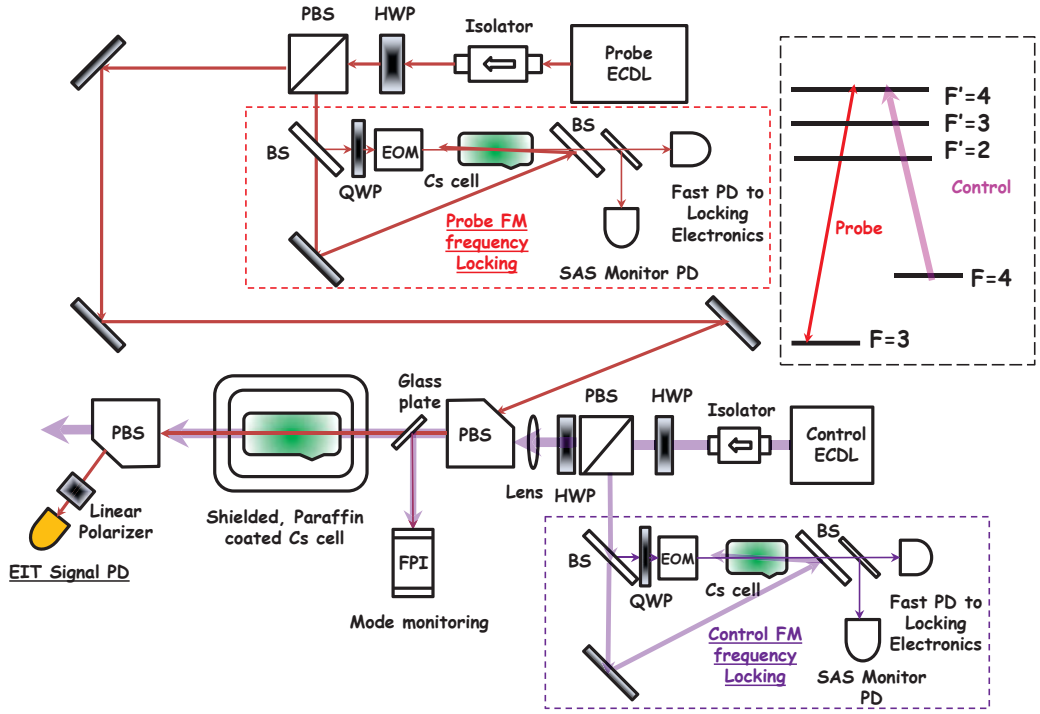

Figure 6.3. CW EIT Setup.

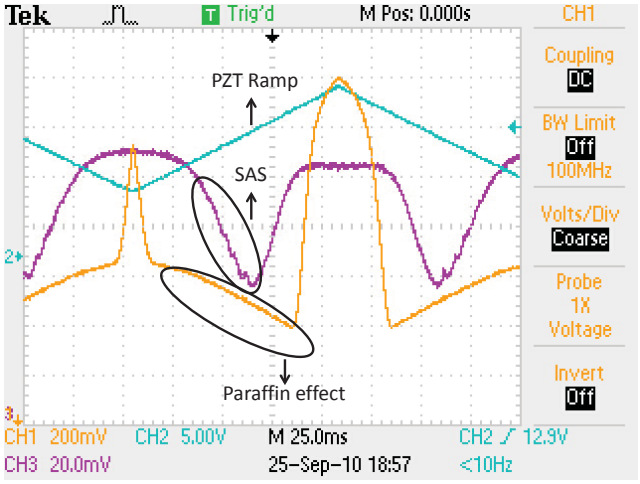

Figure 6.4. Raw data showing the reference saturation spectroscopy signal of the probe laser (pink with small peaks inside), a ramp voltage applied to the piezo which provides the time-base (blue triangle) and the absorption signal of the probe (yellow) after it exits the hot interaction chamber. The probe emerging from the interaction chamber was not at zero because of the DC offset added on by the photodetector used in this measurement.

When the control laser was unblocked, we observed enhanced transmission of the probe signal under conditions of EIT as shown in figure 6.5. The transmission signal could be moved by shifting the lock-point of the control laser. It was sufficient to turn down the servo loop gain to its minimum value and manually changing the piezo DC offset as shown in figure 6.6. The EIT signal under these conditions had a width between 7 MHz to even 17 MHz. Figures 6.5 and 6.6 are two different measurements of the EIT transmission signal. Our best measurement was a width of 7.187 MHz (figure 6.7). We checked calibration in two ways, first by directly calibrating the frequency axis by using a Burliegh 8GHz FP interferometer and as a quick check, we used the theoretical doppler width at the experimental temperature to calibrate the frequency axis. Both methods were consistent with each other over a range of temperatures, but the flattening of the doppler absorption well complicated any attempt to fit the data to a gaussian. The inset in each figure is the saturation absorption spectrum of the probe that indicates the transitions it is scanning over.

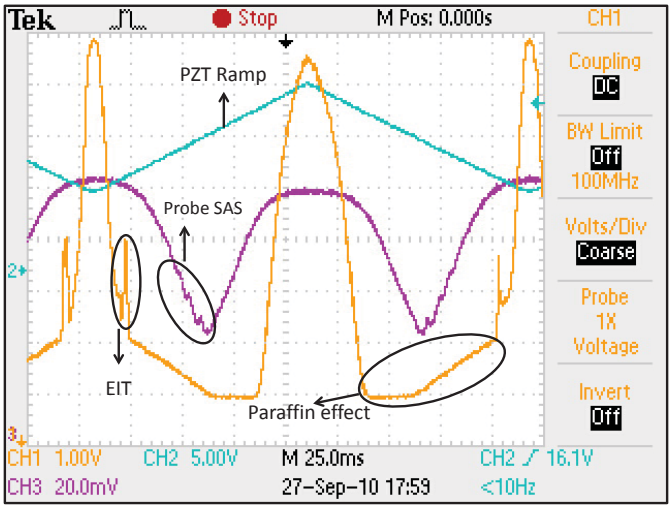

Figure 6.5. Raw data showing the transmission of the probe laser under conditions of EIT after it exits the hot interaction chamber.

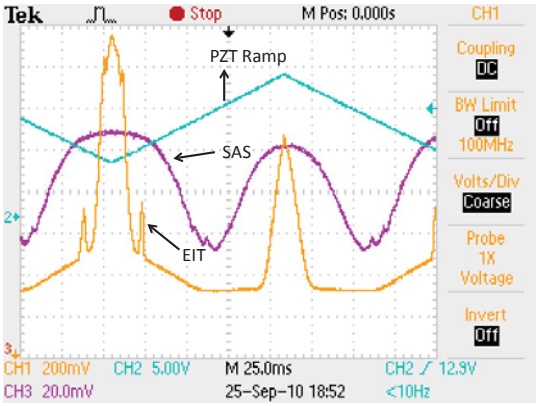

Figure 6.6. Raw data showing the transmission of the probe laser under conditions of EIT after it exits the hot interaction chamber.

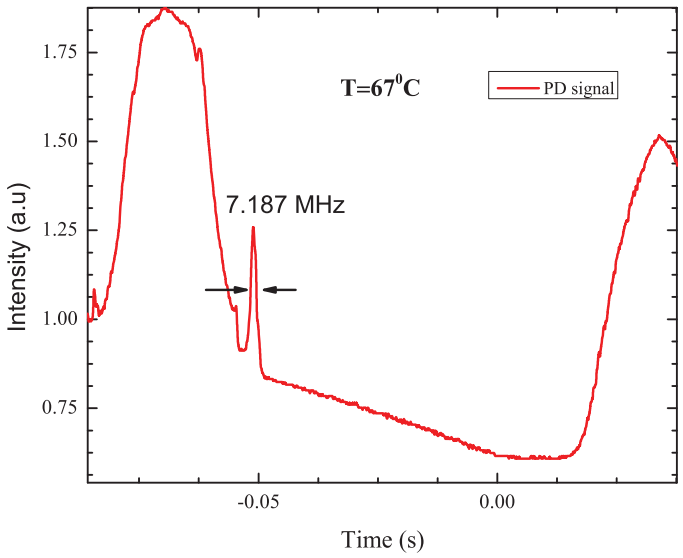

Figure 6.7. EIT transmission signal. Cell temperature was 67°C , probe power of 75μW and a pump power of 10mW. The pump was locked to the F=4→F'=4 transition in an unshielded cell. The probe was scanned across F=3→F' transitions.

6.1.2 Pulsed EIT

Once we saw CW EIT signals, the next step was to investigate generation of a large spin wave based on the light storage experiment of Phillips *et al.,* [56, 63]. We use their idea to obtain a large atomic spin wave under conditions of EIT. In this technique, both the control and probe lasers are pulsed and are partially overlapped. Turning off the control field causes part of the probe to be converted into coherent atomic excitations (spin wave). When the control field is turned on after a short duration, the atomic excitation is converted back to light.

The first step towards generating atomic coherence is to ensure that all the atoms we address are in the lowest $|F = 3\rangle$ ground state. This is accomplished by optical pumping. To test the efficiency of optical pumping, we locked the strong control laser to the $|F = 4\rangle \rightarrow |F' = 4\rangle$ transition and split the beam into a high intensity pulse and a low intensity pulse (attenuated by a neutral density filter) as shown in figure 6.8. Both pulses were controlled by separate acousto-optic modulators (AOM). The pulses were timed such that first, the strong pulse pumped the atoms to $|F = 3\rangle$ and after a brief delay, the weak probe pulse measures optical pumping efficiency by sampling the residual atoms in the upper $|F = 4\rangle$ ground state. The data is shown in figure 6.9. The black pulse is a calibration data-set where both the optical pump and the probe were off resonant. The red pulse shows probe transmission when the optical pump is turned off. As expected, the probe is absorbed. The blue pulse shows greatly enhanced probe transmission with the optical pump pulse turned on which verifies optical pumping.

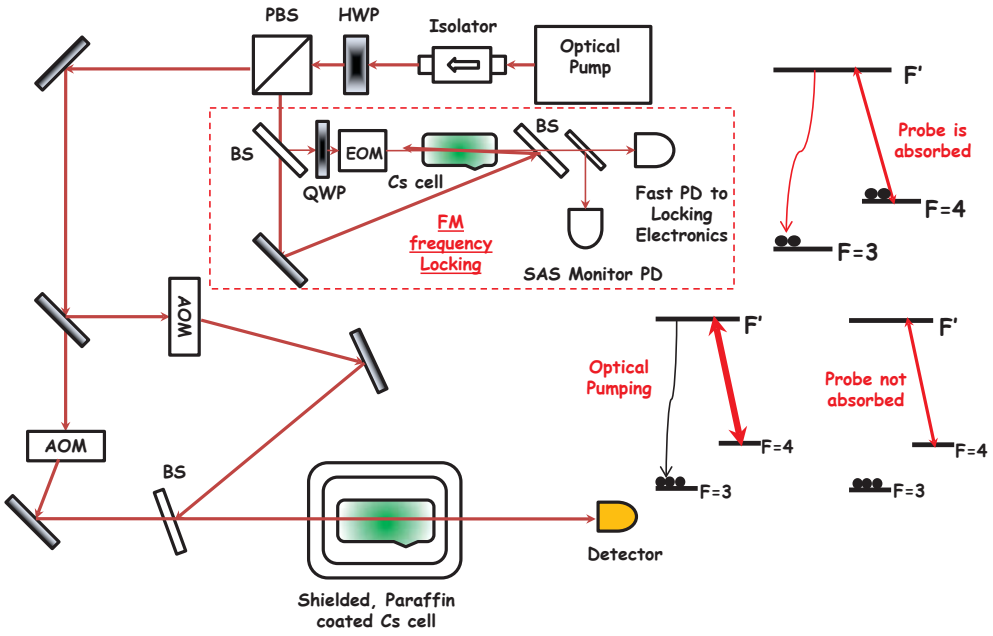

Figure 6.8. Experimental setup to verify optical pumping efficiency. Both pump and probe were derived from the same laser.

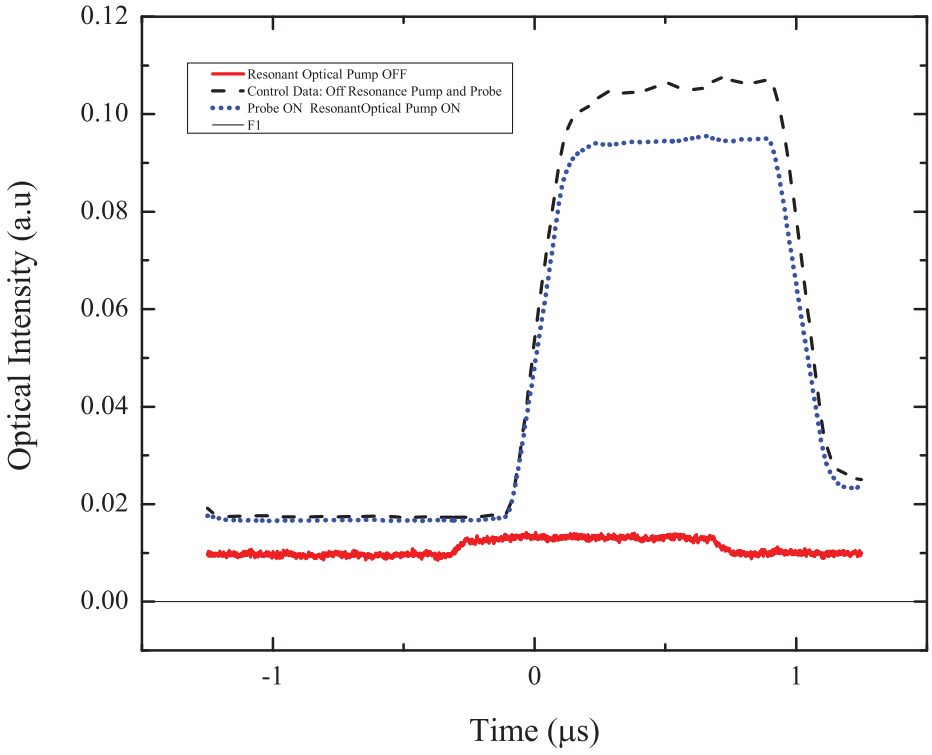

Figure 6.9. Cell temperature was 40° C, probe power of 100μW and a pump power of 4mW. The dashed pulse is the probe transmission completely off resonance. The dotted pulse is the probe transmission with optical pumping turned on. The solid line is the probe absorption with optical pumping turned off. The horizontal line is an aid to the eye.

Next, we have to choose which cell works best for our experiment. We do this by using the optical pumping setup. Optical pumping does not ensure that atoms stay in the pumped ground state $|F = 3\rangle$ forever. Collisions with walls and other Cs atoms due to thermal motion can repopulate the ground state $|F = 4\rangle$. For small time intervals after optical pumping, the $|F = 4\rangle$ is depopulated. By measuring how long it takes for the $|F = 4\rangle$ to repopulate, we can obtain a rough idea about the spin coherence time. If the spin coherence is long lived, then for an appropriate probe pulse width, the intensity should decay proportional to the spin coherence time. For

short spin coherence, the decay profile of the probe pulse should be much steeper. In the extreme case of rapid destruction of coherence, the decay profile gets washed out and can only be seen for extremely short pulse widths. The decay profile of the probe pulse to a simple exponential decay model. In the data shown, the decay tail is fitted to a simple exponential, i.e $N(t) = N_0 e^{-\frac{t}{\tau}}$. The time constant measured for the paraffin cell was measured to about 659.6 μs as shown in figure 6.10 and about 122μs for the buffer gas cell as shown in figure 6.11. We could not obtain reliable results for the bare cell at the same pulse width. In other words, the spin relaxation is definitely worse for a bare cell. With the Ne cell the output signal was very noisy and the temperature of the cell had to be increased to a minimum of 70°C to obtain a large number density of atoms because the partial pressure of Cs was affected by the presence of the buffer gas. Our results were in line with an earlier investigation by Manz *et al.*, who also reported noisy signals when employing buffer gas cells [64]. Based on these results, we choose the paraffin cell as our main experimental cell.

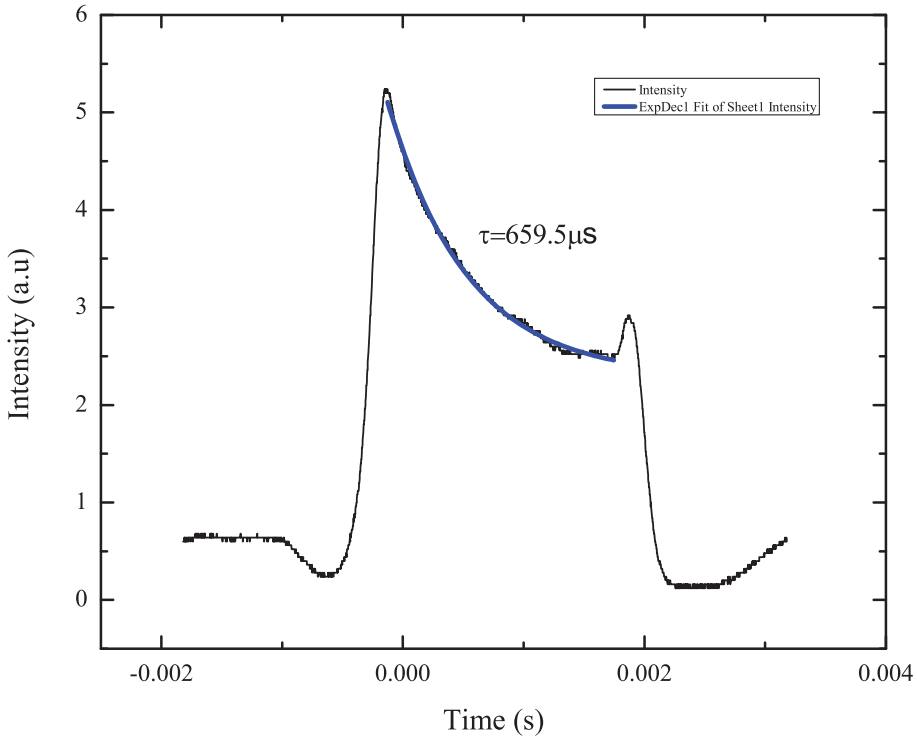

Figure 6.10. Paraffin cell spin relaxation. Cell temperature was 43° C, probe power of 150μW and a pump power of 4mW. The pump was locked to the F=4→F'=4 crossover transition in an unshielded cell and pulsed by an AOM. The probe was derived from the same laser but controlled by a separate AOM.

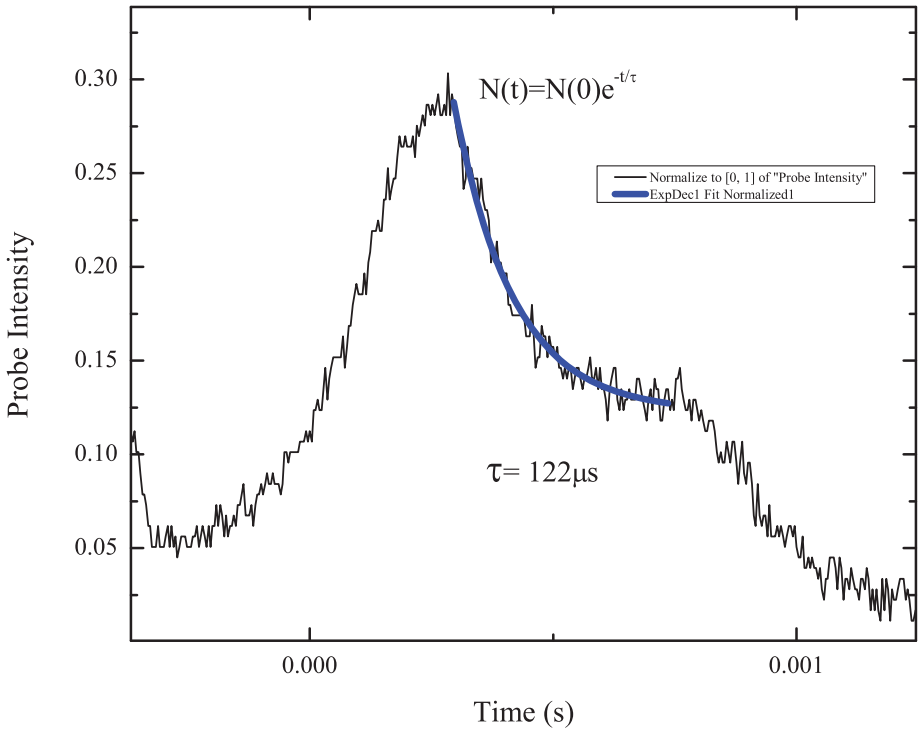

Figure 6.11. Buffer gas cell spin relaxation.Cell temperature was 43° C, probe power of 150μW and a pump power of 4mW. The pump was locked to the F=4→F'=4 crossover transition in an unshielded cell and pulsed by an AOM. The probe was derived from the same laser but controlled by a separate AOM.

We now proceed to the main experiment to generate atomic coherence in Cs vapor by the technique of Phillips *et al.*, [56]. The objective is to generate an atomic spin wave by coherent transfer of quantum state of light to the ensemble of Cs atoms under conditions of EIT. This technique relies on the fact that in EIT, a strong control field dictates the propagation of a weak probe field through a resonant atomic medium and in the process generates strong coupling between the probe photons and the atomic spins. By adiabatically decreasing the control field amplitude, the group velocity is reduced and it is possible to convert the probe pulse entirely to a spin wave. This process is reversible and was theoretically described by the so called Polariton, which is a quasi-particle made up of atomic and photonic excitations [71].

The setup is as shown in figure 6.13. To observe atomic coherence, we need three pulses. An optical pumping pulse ($|F = 4\rangle$), a probe pulse ($|F = 3\rangle$) and a recovery (or read) pulse ($|F = 4\rangle$). The optical pumping and read pulses are derived from the same laser. Figure 6.12 represents the pulse sequence from phase locked signal generators that drive the AOMs and the chopper for our experiment. The yellow pulse of width of 1μs is the signal that drives the AOM generating the probe pulse, the magenta pulse is the signal that drives the optical chopper and represents both the optical pump and the EIT control based on before the overlap with the probe and when it overlaps with the probe respectively[3]. The blue signal is used to drive the AOM controlling the recovery pulse. It derived from the same laser as the optical pump.

All three pulses were synced based on the TTL (transistor-transistor logic) out of the optical chopper. The chopper frequency drifted, but since the AOM derived pulses (from two SRS DS345 signal generators) were locked to it, it did not matter. First, the probe field was scanned till a stable EIT peak was observed. We then zoomed in on the resonance by decreasing the frequency scan of the probe laser. Once we established maximum transmission (given by the DC level of the EIT signal) we engaged the servo lock of the probe laser system. The control field and probe fields are pulsed

[3]The 300ns time delay shown in the figure has no bearing on the actual overlap of the light pulses as the chopper does not generate a sharp cut-off.

by Acousto-Optic Modulators (AOM) and their pulses are carefully overlapped by adjusting the relative phase of the signal generators driving the AOMs. When control laser is then turned off, we expected the part of the probe field to be converted to atomic coherence. One of the main constraints on the efficient generation of a large spin wave is decoherence between the ground states of the lambda system. Coherence can be destroyed by many mechanisms such as depolarizing atom-atom and atom-cell wall collisions , external magnetic field gradients and atoms escaping out of the optical beam path [86]. We employed a passive three layer magnetic shield to minimize external field gradients and used a paraffin coated Cs cell to minimize atom-wall, spin depolarizing collisions [87, 88]. We addressed the issue of atoms escaping the laser beams by increasing the spot size of the control laser to 1cm. Any further increase in spot size resulted in a decrease in intensity of the control beam.

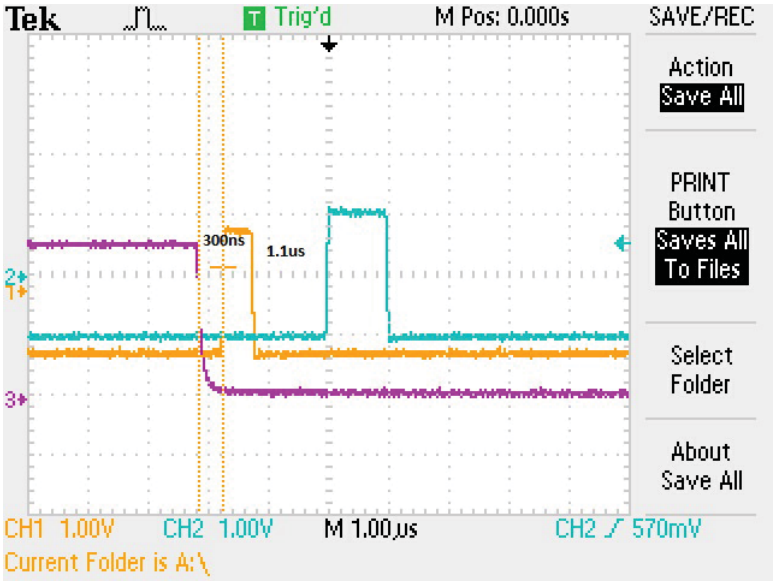

Figure 6.12. TTL pulse train direct from the signal generators. Optical pump (pink), probe(yellow), recovery(blue). The optical pump and the probe overlap in the experiment due to the decay tail of the chopper.

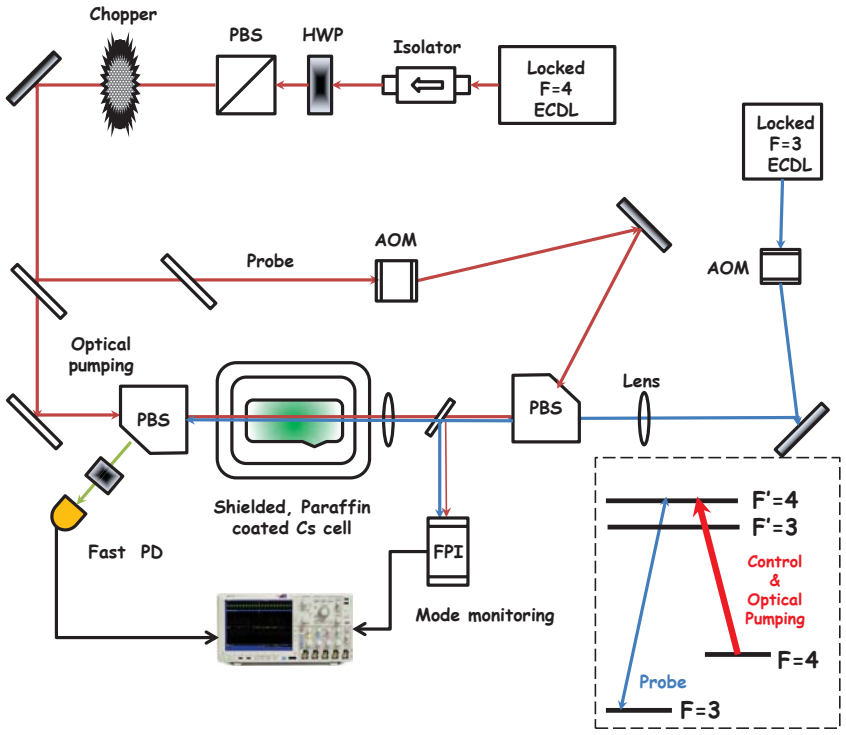

Figure 6.13. Setup for generating atomic coherence by pulsed EIT.

6.1.2.1. Discussion and Results

Novikova *et al.*, [89] provided a prescription for optimizing generation of atomic coherence in the context of light storage. We list those conditions and discuss our results.

The first condition was to ensure that the bandwidth of the probe pulse was less than the so called EIT window. The EIT window can be defined as the FWHM of the EIT transmission signal. In our case, from figure 6.7, the window is 7.187 MHz. Our probe pulse had a duration of 1μs and hence this condition is met. We can calculate the Rabi frequency of our laser as it is proportional to the width of the EIT window. The equation is given as [90]

$$B \propto \frac{\mid \Omega_c \mid^2}{\gamma}, \tag{6.6}$$

Where Ω_c is the control laser Rabi frequency and $\gamma = 2\pi \times 5.22$MHz is the decay rate of the excited state of the Cs D2 line. Using these numbers we estimate the control laser Rabi frequency to be more than 1.59 MHz. This is just an estimate as we do not have perfect EIT, i.e., the probe is not fully transmitted and this indicates loss due to absorption.

The next condition given in [89] dictates that the probe pulse be delayed by at least one temporal width of the original pulse. The group velocity delay can be calculated as

$$\tau = \frac{3}{8B\pi} N\lambda^2 L, \tag{6.7}$$

where τ is the group delay, L is the length of the vapor cell, N is the number density of atoms, λ is the wavelength of light employed and B is the EIT bandwidth. From our data, $B = 1.59$MHz, $N = 2 \times 10^{15}$atoms/cm^3, $L = 10$cm and $\lambda = 852$nm and therefore we obtain $\tau = 10.89\mu$s. To further characterize the EIT window, we defined the EIT contrast as the ratio of the maximum height of the signal to the floor of the signal [87]. As more atoms participate in EIT, the contrast increases as shown in figure 6.14. As the temperature increases, the atoms acquire higher thermal velocities

and move out of the laser beams. Also, collisions are expected to broaden the width of the EIT resonance. We plot the relative widths in figure 6.15.

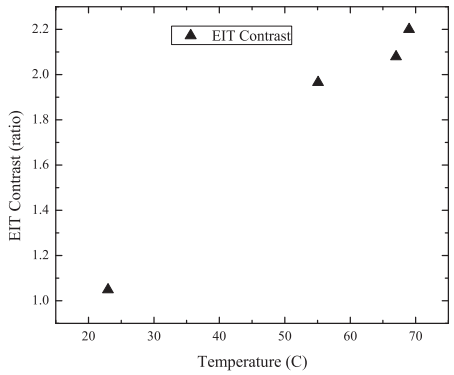

Figure 6.14. EIT contrast.

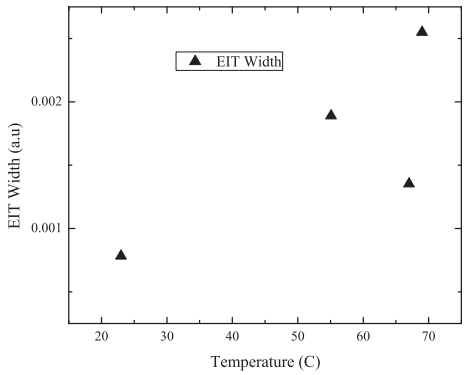

Figure 6.15. EIT width.

We repeated the experiments for a variety of control and probe field powers but could not observe stored atomic coherence. At this point, we are unable to provide evidence or replicate the results of the slow light experiments by Phillips *et al.*, [56]. The signal that we observed (figure 6.16) was inconclusive because it was not repeatable under different experimental conditions of pulse widths, temperatures, control laser power etc. Figures 6.17 to 6.20 show data obtained on one particular day. Thus we are reluctant to conclusively state that we have the ability to generate a large atomic spin wave. Hence we conclude that further optimization needs to be done.

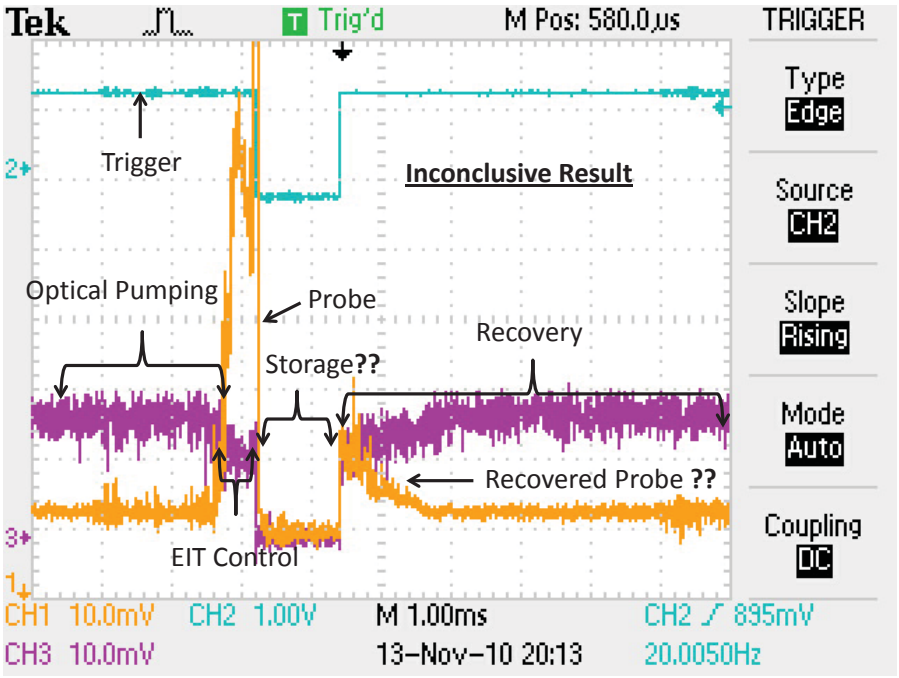

Figure 6.16. Inconclusive result for generation of atomic coherence. Optical pump and recovery pulse (pink), TTL trigger (blue), Total Signal (yellow).

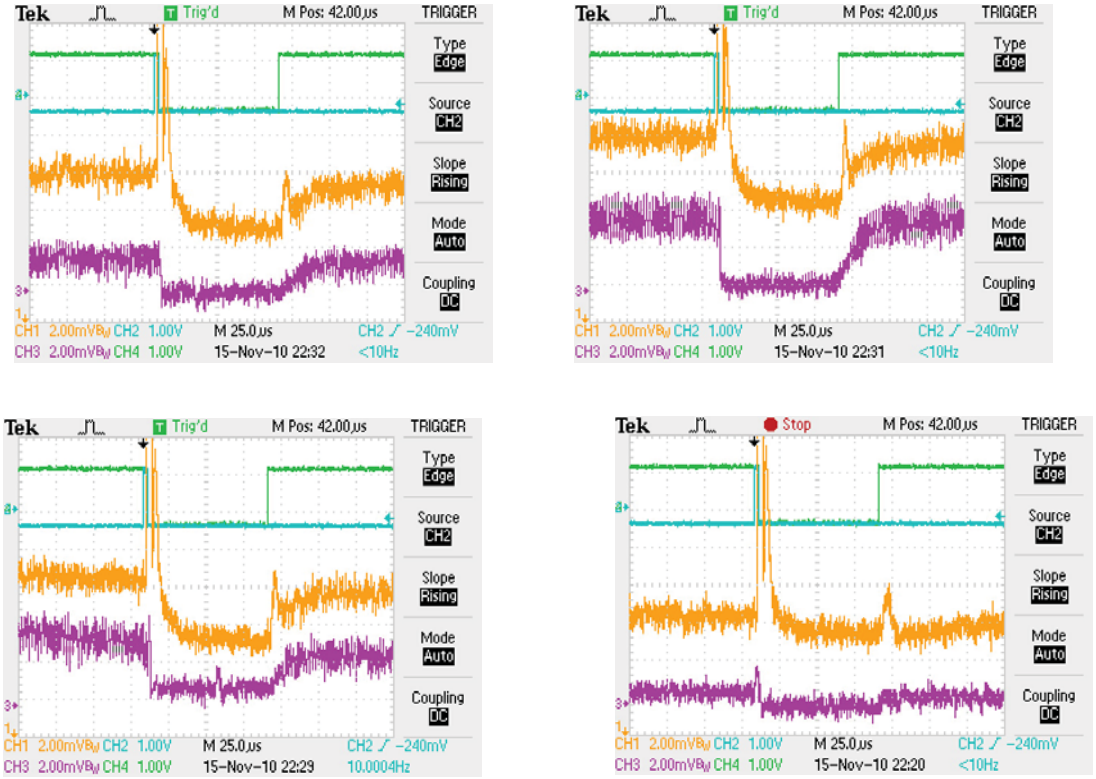

Figure 6.17. Inconclusive result for generation of atomic coherence. Optical pump and recovery pulse (pink), TTL trigger (blue), Total Signal (yellow).

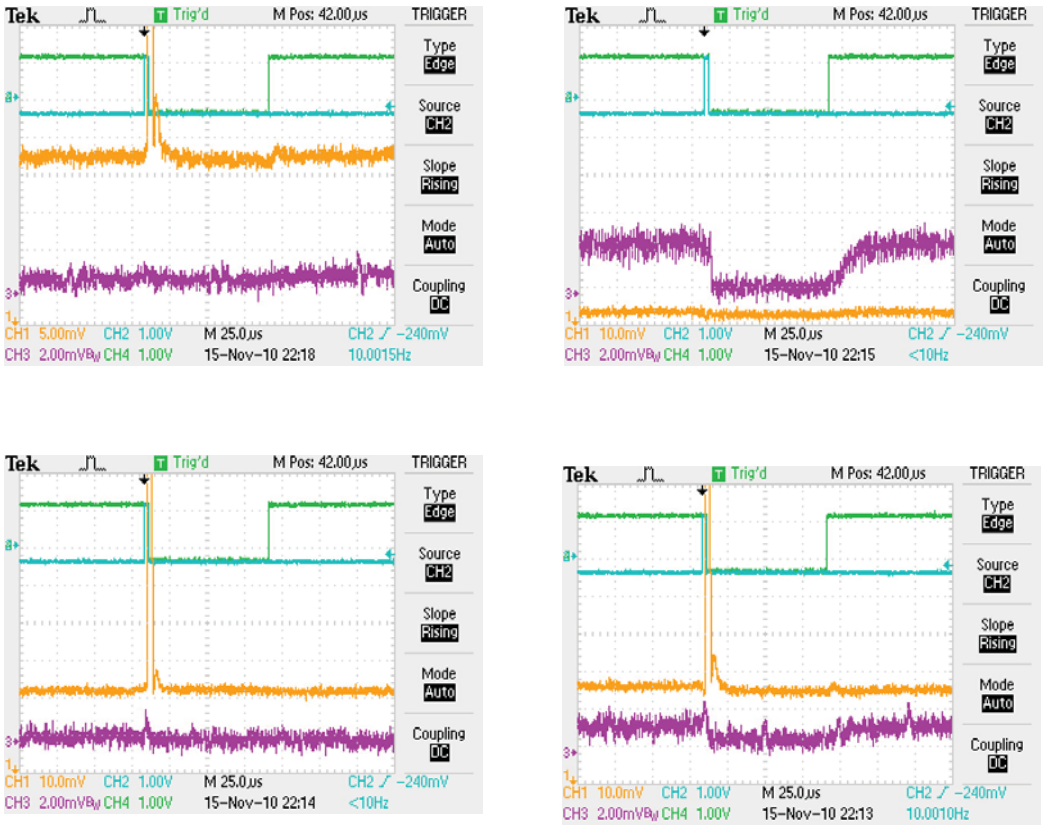

Figure 6.18. Inconclusive result for generation of atomic coherence. Optical pump and recovery pulse (pink), TTL trigger (blue), Total Signal (yellow).

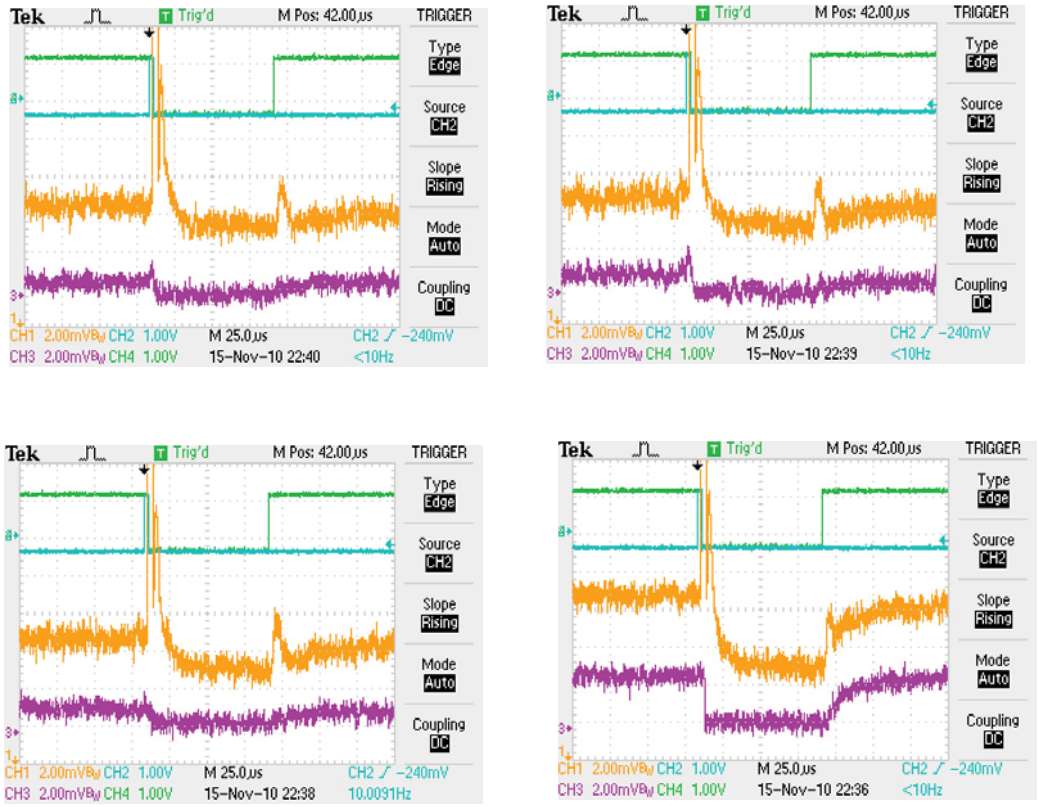

Figure 6.19. Inconclusive result for generation of atomic coherence. Optical pump and recovery pulse (pink), TTL trigger (blue), Total Signal (yellow).

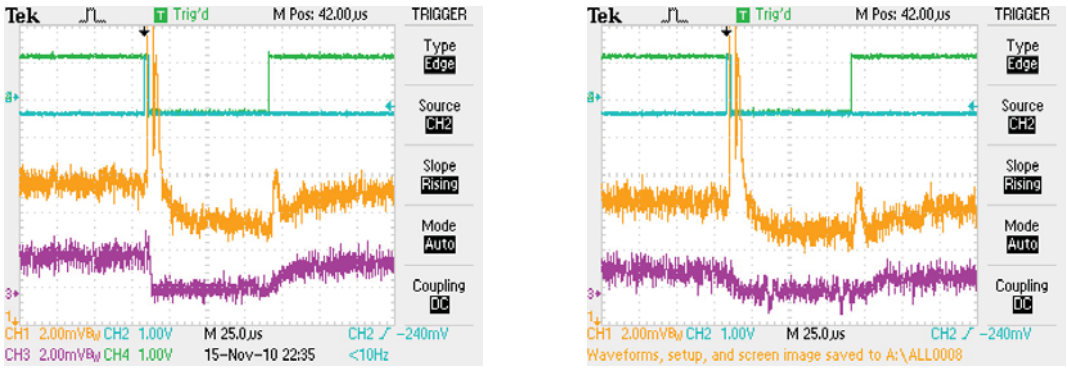

Figure 6.20. Inconclusive result for generation of atomic coherence. Optical pump and recovery pulse (pink), TTL trigger (blue), Total Signal (yellow).

There are many possible reasons not to have observed consistent regeneration of the probe despite satisfying the conditions of pulse bandwidth, group velocity control and maintaining an appropriate EIT window. First, to our knowledge, most slow light experiments have used Zeeman levels instead of bare hyperfine levels as we have. This leads us to believe that maintaining phase coherence between the $|F = 3\rangle$ and $|F = 4\rangle$ lasers is citical. Of the groups who have employed bare hyperfine levels, they used a single laser and generated both control and probe beams by using an EOM at the hyperfine splitting frequency (6GHz for Rb and 9.1GHz for Cs). This ensures almost perfect laser phase coherence. Another possible issue could be our choice of the D2 line instead of the D1 line because D1 line is less cluttered by Zeeman transitions than the D2 line. Our choice was dictated by the lack of availability of high power single mode 894nm lasers. Perhaps passive magnetic shielding is insufficient and active magnetic shielding is also necessary. We do not have access to calibrating equipment to our magnetic shield at the location of the setup and have relied on the numbers for isolation effectiveness provided by the manufacturer. It could also be possible that periodic degaussing of the chamber is necessary. Our lasers had a long term linewidth of about 4MHz and given the fact that we did observe CW EIT signals leads us to believe that the servo lock control is working and should not be an issue. However, the commercial tapered amplified based control laser did exhibit power fluctuations and further investigation is necessary to characterize this.

A few changes to make would be to switch to a Zeeman setup, which ensures the laser phase coherence condition. However, this could entail a complete revamping of the laser locking setup to a dichroic atomic vapor lock design and requires extensive and expensive calibration of magnetic fields and design of high current active magnetic field control electronics. Another approach would be to ensure phase coherence by generating the control and pump beams shifted by 9.1GHz from the same laser by using a high frequency EOM. This is also an expensive investment and the electronics down the chain tend to be more complicated. Yet another option would be to try the same experiment on the simpler structure of the D1 line. However, if phase coherence

is the limitation, we end up back to square one. To summarize, more work needs to be done whichever path is taken and hopefully, modifications to the setup in the future will generate more conclusive results.

LIST OF REFERENCES

LIST OF REFERENCES

[1] M. H. Shamos. *Great Experiments in Physics: Firsthand Accounts from Galileo to Einstein*. Dover classics of science and mathematics. Dover Publications, 1987.

[2] G. L. Trigg. *Landmark Experiments in Twentieth Century Physics*. Dover Science Books. Dover Publications, 2011.

[3] B. Kramer. *The Art of measurement: metrology in fundamental and applied physics*. Forsche, Messen, Prüfen. VCH, 1988.

[4] W.H. Steel. *Interferometry*. Cambridge monographs on physics. Cambridge U.P., 1967.

[5] M. Born, E. Wolf, A. B. Bhatia, P. C. Clemmow, D. Gabor, A. R. Stokes, A. M. Taylor, P. A. Wayman, and W. L. Wilcock. *Principles of Optics: Electromagnetic Theory of Propagation, Interference and Diffraction of Light*. Cambridge University Press, 2000.

[6] A. D. Cronin, J. Schmiedmayer, and D. E. Pritchard. Optics and interferometry with atoms and molecules. *Rev. Mod. Phys.*, 81:1051–1129, Jul 2009.

[7] A. A. Michelson and E. W. Morley. On the relative motion of the earth and the luminiferous ether. *American Journal of Science*, 34(203):333–345, 1887.

[8] http://dictionary.reference.com/browse/sensitivity.

[9] Z. Y. Ou. Enhancement of the phase-measurement sensitivity beyond the standard quantum limit by a nonlinear interferometer. *Physical Review A*, 85(2):023815, 2012.

[10] C. M. Caves. Quantum limits on noise in linear amplifiers. *Phys. Rev. D*, 26(8):1817–1839, Oct 1982.

[11] D. Kouznetsov, R. Ortega-Martinez, and D. Rohrlich. Quantum noise limits for nonlinear, phase-invariant amplifiers. *Phys. Rev. A*, 52(2):1665–1669, Aug 1995.

[12] P. M. Anisimov, G. M. Raterman, A. Chiruvelli, W. N. Plick, S. D. Huver, H. Lee, and J. P. Dowling. Quantum metrology with two-mode squeezed vacuum: parity detection beats the heisenberg limit. *Phys Rev Lett*, 104(10):103602, Mar 2010.

[13] S. W. Ballmer. *LIGO interferometer operating at design sensitivity with application to gravitational radiometry*. PhD thesis, Massachusetts Institute of Technology. Dept. of Physics, 2006.

[14] The advanced ligo project (https://www.advancedligo.mit.edu/).

[15] D. F. Walls and G. J. Milburn. *Quantum Optics*. Springer, 2008.

[16] H. A. Bachor and T. C. Ralph. *A Guide To Experiments in Quantum Optics*. Physics Textbook. Wiley-VCH, 2004.

[17] L. Pezz and A. Smerzi. Mach-Zehnder interferometry at the Heisenberg limit with coherent and squeezed-vacuum light. *Phys Rev Lett*, 100(7):073601, Feb 2008.

[18] R. Loudon. Squeezed light. *Journal of Modern Optics*, 34:709–759, 1987.

[19] Y. Chen, X. Bao, Z. Yuan, S. Chen, B. Zhao, and J. W. Pan. Heralded generation of an atomic noon state. *Phys Rev Lett*, 104(4):043601, Jan 2010.

[20] F. W. Sun, B. H. Liu, Y. X. Gong, Y. F. Huang, Z. Y. Ou, and G. C. Guo. Experimental demonstration of phase measurement precision beating standard quantum limit by projection measurement. *EPL (Europhysics Letters)*, 82(2):24001, 2008.

[21] V. Giovannetti, S. Lloyd, and L. Maccone. Quantum-enhanced measurements: Beating the standard quantum limit. *Science*, 306(5700):1330–1336, 2004.

[22] B. Yurke, S. L. McCall, and J. R. Klauder. SU(2) and SU(1,1) interferometers. *Phys. Rev. A*, 33:4033–4054, Jun 1986.

[23] Boyd R. W. *Nonlinear Optics 3rd Ed.* Academic Press, 2008.

[24] Z. Y. Ou. Fundamental quantum limit in precision phase measurement. *Phys. Rev. A*, 55:2598–2609, Apr 1997.

[25] Z. Y. Ou. Complementarity and fundamental limit in precision phase measurement. *Phys. Rev. Lett.*, 77:2352–2355, Sep 1996.

[26] Z. Y. Ou, S. F. Pereira, H. J. Kimble, and K. C. Peng. Realization of the einstein-podolsky-rosen paradox for continuous variables. *Phys. Rev. Lett.*, 68:3663–3666, Jun 1992.

[27] P. A. Franken, A. E. Hill, C. W. Peters, and G. Weinreich. Generation of Optical Harmonics. *Phys.Rev.Lett.*, 7:118–119, 1961.

[28] P. Campagnola. Second harmonic generation imaging microscopy: Applications to diseases diagnostics. *Analytical Chemistry*, 83(9):3224–3231, 2011.

[29] Y. R. Shen. *The principles of nonlinear optics*. Wiley Series in Pure and Applied Optics. J. Wiley, 1984.

[30] J. A. Armstrong, N. Bloembergen, J. Ducuing, and P. S. Pershan. Interactions between light waves in a nonlinear dielectric. *Phys. Rev.*, 127(6):1918–1939, Sep 1962.

[31] Z. Y. Ou. Propagation of quantum fluctuations in single-pass second-harmonic generation for arbitrary interaction length. *Phys. Rev. A*, 49(3):2106–2116, Mar 1994.

[32] R. D. Li and P. Kumar. Quantum-noise reduction in traveling-wave second-harmonic generation. *Phys. Rev. A*, 49(3):2157–2166, Mar 1994.

[33] G. S. Agarwal. Master equations in phase-space formulation of quantum optics. *Phys.Rev.*, 178:2025–2035, 1969.

[34] G. S. Agarwal. Quantum theory of second harmonic generation. *Optics Communications*, 1(3):132 – 134, 1969.

[35] M. Orszag, P. Carrazana, and H. Chuaqui. Quantum theory of second-harmonic generation. *Optica Acta: International Journal of Optics*, 30(3):259–266, 1983.

[36] Y. R. Shen. Quantum Statistics of Nonlinear Optics. *Phys.Rev.*, 155:921–931, 1967.

[37] L. F. Abbott. *Relativity, Cosmology, Topological Mass and Supergravity.* World Scientific,Singapore, 1983.

[38] H. A. Schmitt and A. Mufti. Generalized coherent states as eigenstates of linearized quadratic casimir operators. *Journal of Physics A: Mathematical and General*, 23(17):L861, 1990.

[39] D. Binosi and A. Quadri. The Background Field Method as a Canonical Transformation. 2012.

[40] L.F. Abbott. Introduction to the Background Field Method. *Acta Phys.Polon.*, B13:33, 1982.

[41] Y. J. Feng and C. S. Lam. Generalized background field method. *Phys.Rev.*, D56:6640–6647, 1997.

[42] H. G. Dosch. The method of vacuum background fields. *Nucl.Phys.Proc.Suppl.*, 23B:186–190, 1991.

[43] O. K. Lim, B. Boland, and M. Saffman. Observation of twin beam correlations and quadrature entanglement by frequency doubling in a two-port resonator. *EPL (Europhysics Letters)*, 78(4):40004, 2007.

[44] B. Yurke, P. Grangier, and R. E. Slusher. Squeezed-state enhanced two-frequency interferometry. *J. Opt. Soc. Am. B*, 4(10):1677–1682, Oct 1987.

[45] http://literature.agilent.com/litweb/pdf/5965-7920e.pdf.

[46] P. Galatola, L. A. Lugiato, P. Porreca, M. G.and Tombesi, and G. Leuchs. System control by variation of the squeezing phase. *OPTICS COMMUNICATIONS*, 85(1):95–103, AUG 15 1991.

[47] A. S. Villar. The conversion of phase to amplitude fluctuations of a light beam by an optical cavity. *American Journal of Physics*, 76(10):922–929, 2008.

[48] L. M. Duan, M. D. Lukin, J. I. Cirac, and P. Zoller. Long-distance quantum communication with atomic ensembles and linear optics. *Nature*, 414(6862):413–418, Nov 2001.

[49] H.J. Briegel, W. Dür, J. I. Cirac, and P. Zoller. Quantum repeaters: The role of imperfect local operations in quantum communication. *Phys. Rev. Lett.*, 81:5932–5935, Dec 1998.

[50] K. F. Reim, P. Michelberger, K. C. Lee, J. Nunn, N. K. Langford, and I. A. Walmsley. Single-photon-level quantum memory at room temperature. *Phys. Rev. Lett.*, 107:053603, Jul 2011.

[51] E. Arimondo. Coherent population trapping in laser spectroscopy. volume 35 of *Progress in Optics*, pages 257 – 354. Elsevier, 1996.

[52] Z. Y. Ou. Efficient conversion between photons and between photon and atom by stimulated emission. *Physical Review A*, 78(2):023819, 2008.

[53] Daniel Steck. Cesium d line data, August 2009.

[54] M. Fleischhauer, A. Imamoglu, and J. P. Marangos. Electromagnetically induced transparency: Optics in coherent media. *Rev. Mod. Phys.*, 77(2):633–673, Jul 2005.

[55] W. Happer. Optical pumping. *Rev. Mod. Phys.*, 44(2):169–249, Apr 1972.

[56] D. F. Phillips, A. Fleischhauer, A. Mair, R. L. Walsworth, and M. D. Lukin. Storage of light in atomic vapor. *Phys. Rev. Lett.*, 86(5):783–786, Jan 2001.

[57] A. Kuzmich, W. P. Bowen, A. D. Boozer, A. Boca, C. W. Chou, L. M. Duan, and H. J. Kimble. Generation of nonclassical photon pairs for scalable quantum communication with atomic ensembles. *Nature*, 423(6941):731–734, 2003.

[58] M. O. Scully and M. S. Zubairy. *Quantum Optics*. Cambridge University Press, September 28, 1997.

[59] A. A. Lagana, M. A. Lohe, and L. von Smekal. Construction of a universal quantum computer. *Phys. Rev. A*, 79:052322, May 2009.

[60] M. G. Raymer and J. Mostowski. Stimulated raman scattering: Unified treatment of spontaneous initiation and spatial propagation. *Phys. Rev. A*, 24(4):1980–1993, Oct 1981.

[61] J. Mostowski and M. G. Raymer. The buildup of stimulated raman scattering from spontaneous raman scattering. *Optics Communications*, 36(3):237 – 240, 1981.

[62] L. Q. Chen, G. W. Zhang, C. H. Yuan, J. Jing, Z. Y. Ou, and W. Zhang. Enhanced raman scattering by spatially distributed atomic coherence. *Applied Physics Letters*, 95:1115, 2009.

[63] A. S Zibrov A.Andre D.F Philips R.L. Walsworth C. H van der Wal, M. D Eisaman and M.D Lukin. Towards non-classical light storage via atomic-vapor raman scattering. *cfa-www.harvard.edu/Walsworth/pdf/walspie03.pdf*.

[64] S. Manz, T. Fernholz, J. Schmiedmayer, and J. W. Pan. Collisional decoherence during writing and reading quantum states. *Phys. Rev. A*, 75(4):040101, Apr 2007.

[65] D. Felinto, C. W. Chou, H. de Riedmatten, S. V. Polyakov, and H. J. Kimble. Control of decoherence in the generation of photon pairs from atomic ensembles. *Phys. Rev. A*, 72(5):053809, Nov 2005.

[66] E. Figueroa, F. Vewinger, J. Appel, and A. I. Lvovsky. Decoherence of electromagnetically induced transparency in atomic vapor. *Opt. Lett.*, 31(17):2625–2627, Sep 2006.

[67] C. Schroll, W. Belzig, and C. Bruder. Decoherence of cold atomic gases in magnetic microtraps. *Phys. Rev. A*, 68:043618, Oct 2003.

[68] Y. R. Shen and N. Bloembergen. Theory of stimulated brillouin and raman scattering. *Phys. Rev.*, 137:A1787–A1805, Mar 1965.

[69] L. Mandel and E. Wolf. *Optical Coherence and Quantum Optics*. Cambridge University Press.

[70] M. Fleischhauer, A. Imamoglu, and J. P. Marangos. Electromagnetically induced transparency: Optics in coherent media. *Reviews of Modern Physics*, 77(2):633, 2005.

[71] M. Fleischhauer and M. D. Lukin. Dark-state polaritons in electromagnetically induced transparency. *Phys. Rev. Lett.*, 84(22):5094–5097, May 2000.

[72] M. Bajcsy, A. S. Zibrov, and M. D. Lukin. Stationary pulses of light in an atomic medium. *Nature*, 426(6967):638–641, 2003.

[73] M. Klein, Y. Xiao, M. Hohensee, D. F. Phillips, and R. L. Walsworth. Slow light and eit under realistic (imperfect) conditions. pages 72260H–72260H–8, 2009.

[74] F. Reif. *Fundamentals of Statistical and Thermal Physics*. McGraw-Hill series in fundamentals of physics. McGraw-Hill, 1965.

[75] E. E. Mikhailov, Y. V. Rostovtsev, and G. R. Welch. Group velocity study in hot 87Rb vapour with buffer gas. *Journal of Modern Optics*, 50(15-17):2645–2654, 2003.

[76] S. Brandt, A. Nagel, R. Wynands, and D. Meschede. Buffer-gas-induced linewidth reduction of coherent dark resonances to below 50 hz. *Phys. Rev. A*, 56:R1063–R1066, Aug 1997.

[77] N. B. Phillips. *Slow and Stored light under conditions of electromagnetically induced transparency and four wave mixing in an atomic vapor*. PhD thesis, College of William and Mary, August 2011.

[78] C. Garrod. *Statistical Mechanics and Thermodynamics: PC Version*. Oxford University Press, USA, 1995.

[79] S. Rosin and I. I. Rabi. Effective collision cross sections of the alkali atoms in various gases. *Phys. Rev.*, 48:373–379, Aug 1935.

[80] N. Beverini, P. Minguzzi, and F. Strumia. Foreign-gas-induced cesium hyperfine relaxation. *Phys. Rev. A*, 4:550–555, Aug 1971.

[81] M. Mitchner and C.H. Kruger. *Partially ionized gases*. Wiley series in plasma physics. Wiley, 1973.

[82] M. A. Bouchiat and J. Brossel. Relaxation of optically pumped rb atoms on paraffin-coated walls. *Phys. Rev.*, 147:41–54, Jul 1966.

[83] M. V. Balabas, T. Karaulanov, M. P. Ledbetter, and D. Budker. Polarized alkali-metal vapor with minute-long transverse spin-relaxation time. *Phys. Rev. Lett.*, 105:070801, Aug 2010.

[84] C. E. Wieman and Hollberg L. Using diode lasers for atomic physics. *Review of Scientific Instruments*, 62(1):1–20, 1991.

[85] R. Scholten. http://optics.ph.unimelb.edu.au/atomopt/diodes.html.

[86] M. D. Lukin. Colloquium : Trapping and manipulating photon states in atomic ensembles. *Rev. Mod. Phys.*, 75:457–472, Apr 2003.

[87] M. Klein, M. Hohensee, D. F. Phillips, and R. L. Walsworth. Electromagnetically induced transparency in paraffin-coated vapor cells. *Phys. Rev. A*, 83:013826, Jan 2011.

[88] M. Klein, I. Novikova, D. F. Phillips, and R. L. Walsworth. Slow light in paraffin-coated rb vapour cells. *Journal of Modern Optics*, 53(16-17):2583–2591, 2006.

[89] I. Novikova, M. Klein, D. F. Phillips, and R. L. Walsworth. Optimizing stored light efficiency in vapor cells. *Proc. SPIE 5735, Advanced Optical and Quantum Memories and Computing II, 87*, pages 87–97, 2005.

[90] J. P. Marangos. Electromagnetically induced transparency. *Journal of Modern Optics*, 45(3):471–503, 1998.

[91] Richard W. Fox, Chris W. Oates, and Leo W. Hollberg. *Stabilizing diode lasers to high-finesse cavities*, volume 40, chapter 1. 2003.

APPENDIX

APPENDIX

A. Laser Diode System Mechanical Design

Experiments in atomic physics need a source of light which is coherent, single longitudinal mode, has a narrow linewidth, is tunable and is stable in frequency. Free running lasers do not satisfy all these requirements simultaneously. These requirements are realized by a simple and cost effective setup known as the Extended Cavity Diode Laser (*ECDL*) system. In an ECDL, the laser linewidth is narrowed by optical feedback and frequency stability is achieved by both passive (controlling the injection current, temperature regulation) and active (electronic feedback) means. I am indebted to Prof. R. Scholten at the university of Melbourne and Prof. Vasant Natarajan at the Indian Institute of Science for providing design prototypes and technical feedback for our diode laser systems.

A.1 Design 1

Laser linewidth narrowing is achieved by optical feedback by sending the 0^{th} order mode into the laser diode. In order to do this the grating (Newport,holographic 1800 lines/mm) has to be positioned at the correct angle.

$$\begin{aligned} m\lambda &= 2d\sin\alpha \\ d &= 1800\times 10^{3} lines/mm \\ \lambda &= 850\times 10^{-9} m \\ \Rightarrow \sin\alpha &= 50^{\circ} \end{aligned} \tag{A.1}$$

We cut a commercially available 3-axis mirror mount and mounted it on a large thermal block. The common theme in case of any ECDL design is mechanical stability and thermal stability. To satisfy this, we used a $4\times3\times3$ inch thick block of Aluminum.

Aluminum is easy to machine and has good thermal conductivity. We specifically chose grade 6061 Aluminum. This is particular grade of Al is used in aircraft bodies and in race cars. It has very good thermal properties and is particularly conducive to machining. Next, the commercial Newport mount had to be cut to accommodate the grating mount and the ECDL tube and finally everything was assembled along with the micrometers.

The Piezo receptacle is an essential part because there is a lot of pressure being applied by the ball joint of the micrometer on the PZT material. It could lead to early mechanical failure of the device, if there was no protective sheathing.

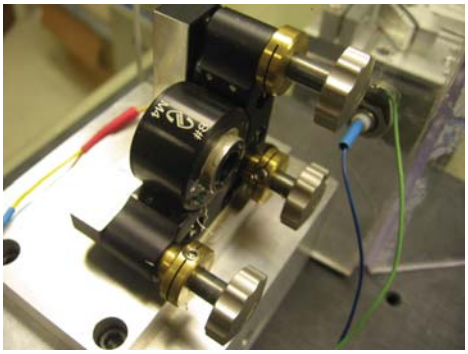

(a) Modified mirror mount.

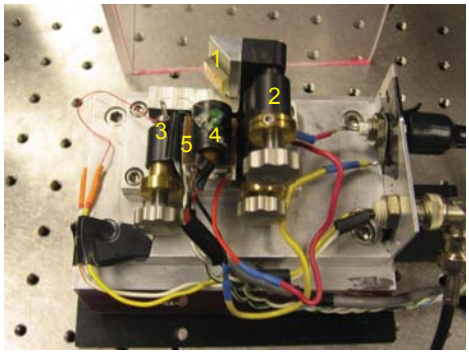

(b) 1-Diffraction grating, 2-Modified mirror mount,3-Piezo receptacle,4-LD collimation tube and thermistor,5-TEC.

Figure A.1. Laser design based on Prof. R. Scholten's design at the university of Melbourne.

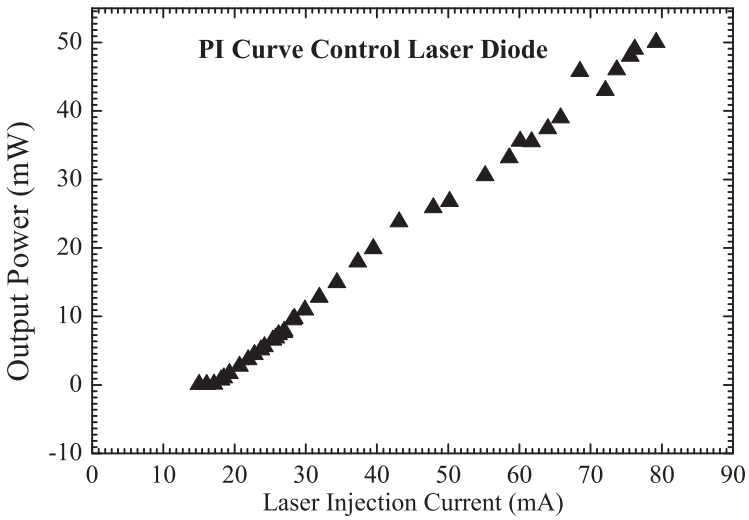

Figure A.2. Laser power vs intensity curve after the threshold was optimized.

A.2 Design 2

In design 2 , everything was machined and no commercial mounts were used. This is a standard design being used in commercial laser systems. This design is based on double flexure mounts for the laser. The advantage of this design over the first was that it was very easy to align the laser as the grating holder is fully adjustable and there are multiple ways to adjust the feedback into the laser. An important point to note is that brass was to make the O-ring holding the LD, as it has superior thermal properties. As it will be seen later, this is necessary because of the placement of the TEC element is different in both designs. After assembly, the system looked as shown in figure A.3.

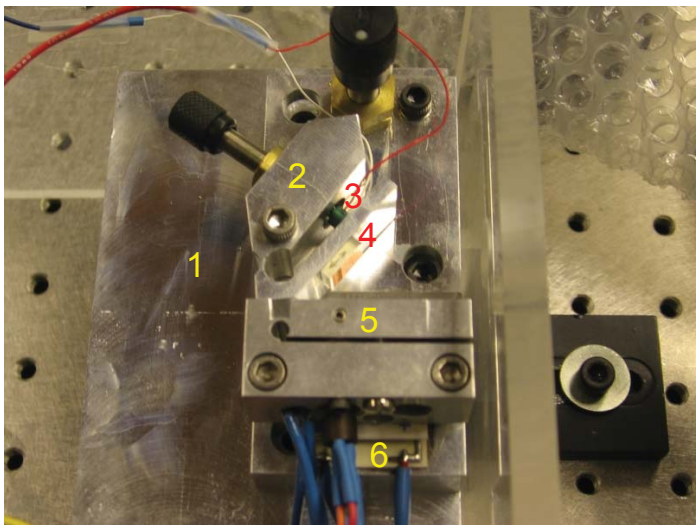

(a) 1-Thermal Block, 2-Grating mount,3-Piezo,4-Grating,5-LD mount and collimating lens,6-TEC.

Figure A.3. Design 2 fully assembled.

B. Electronics Design

Presented below are circuit schematics of a a balanced photodetector based on the OPT101 monolithic amplifier, photodiode chip and the servo lock circuit. The servo lock circuit shown in figures B.3, B.4 was adapted from Fox and Hollberg's paper [91].

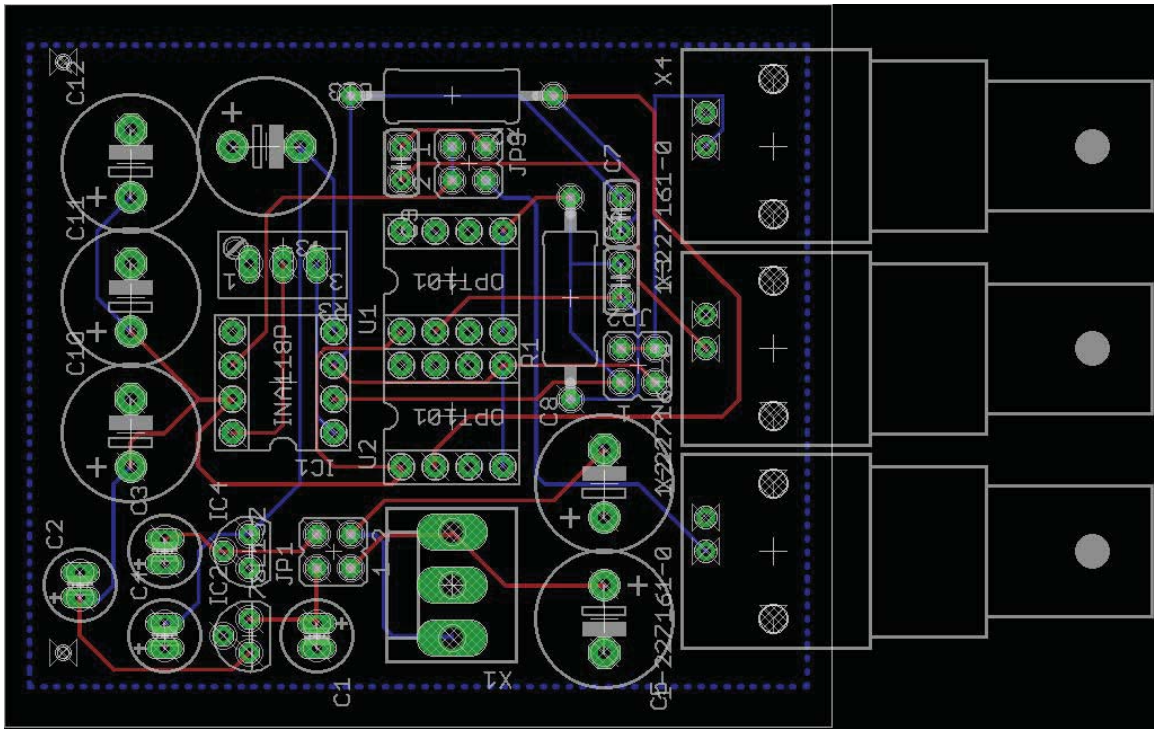

Figure B.1. Balanced Photodetector PCB.

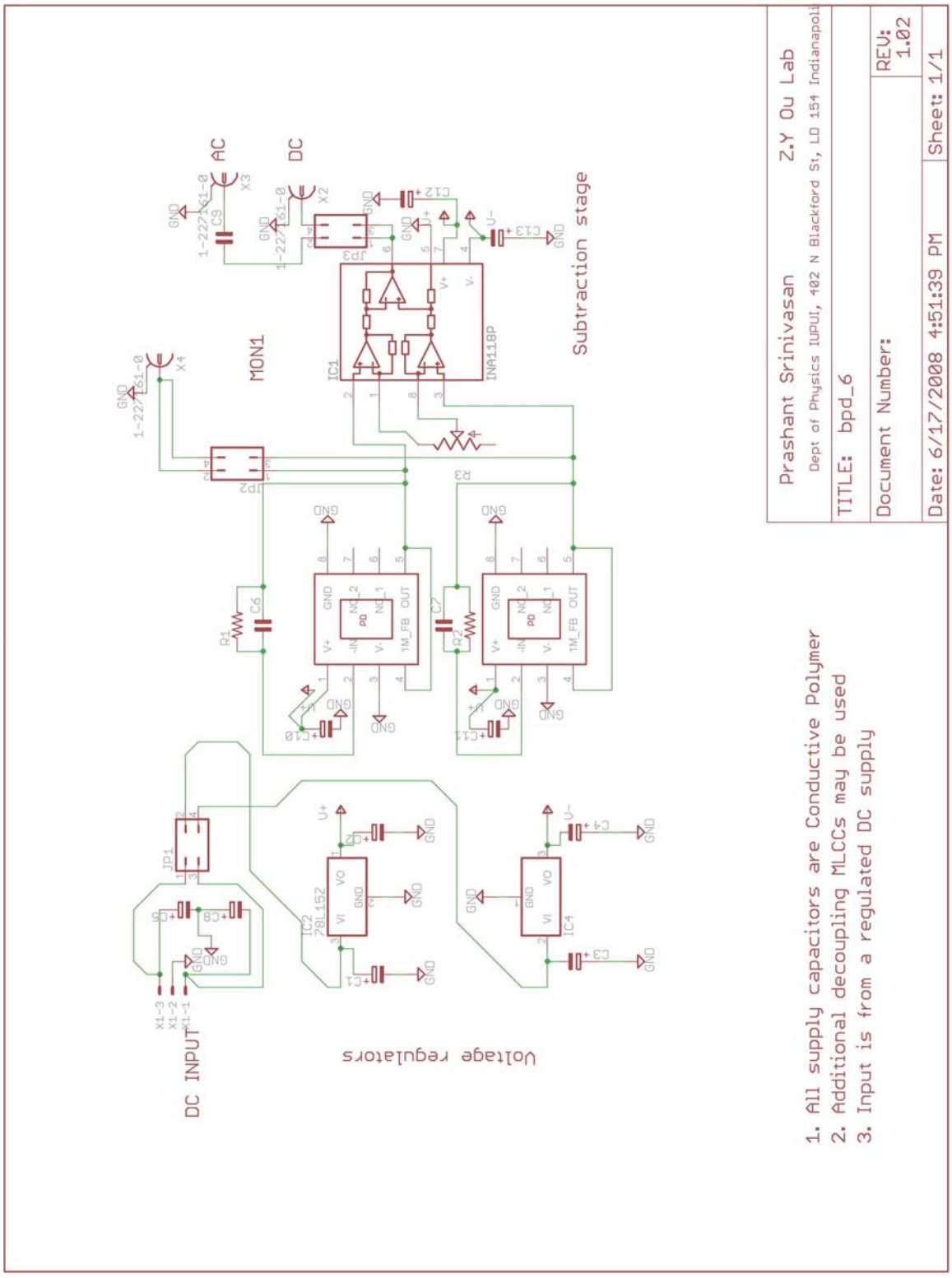

Figure B.2. Balanced Photodetector.

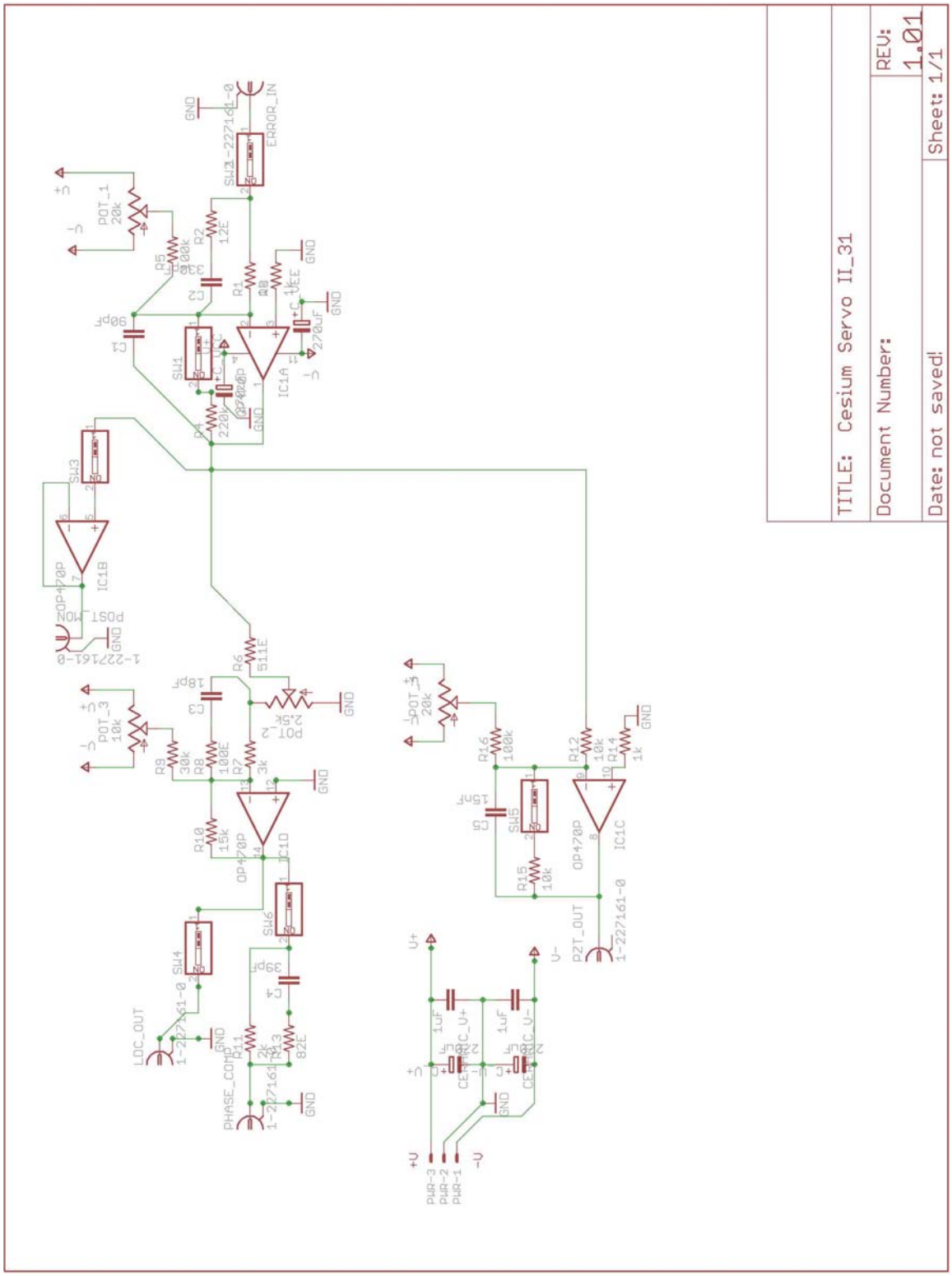

Figure B.3. Schematic for the servo lock circuit.The design was done using a free version of EAGLE CAD from Cadsoft Inc.

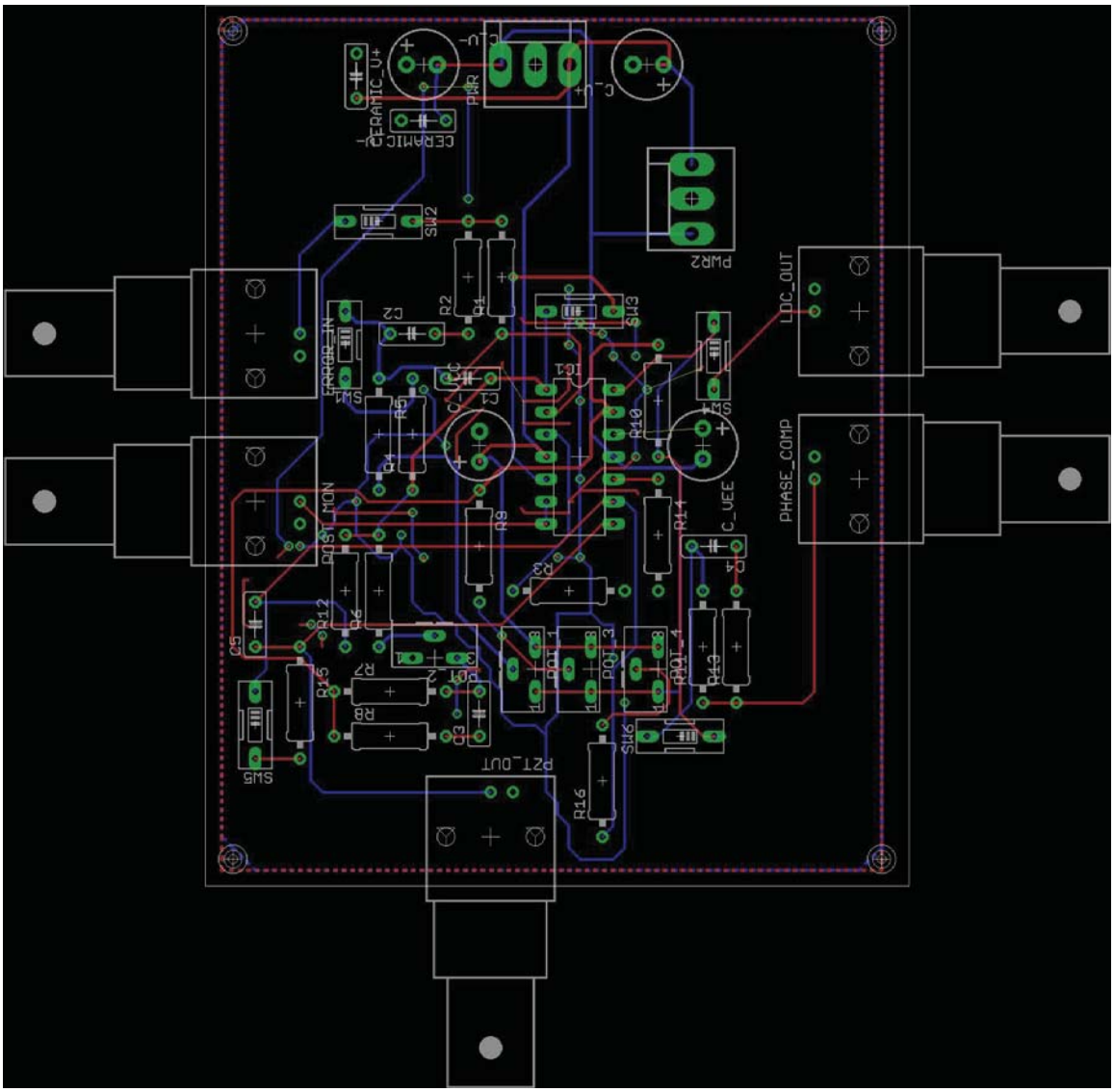

Figure B.4. PCB layout for the servo lock circuit.

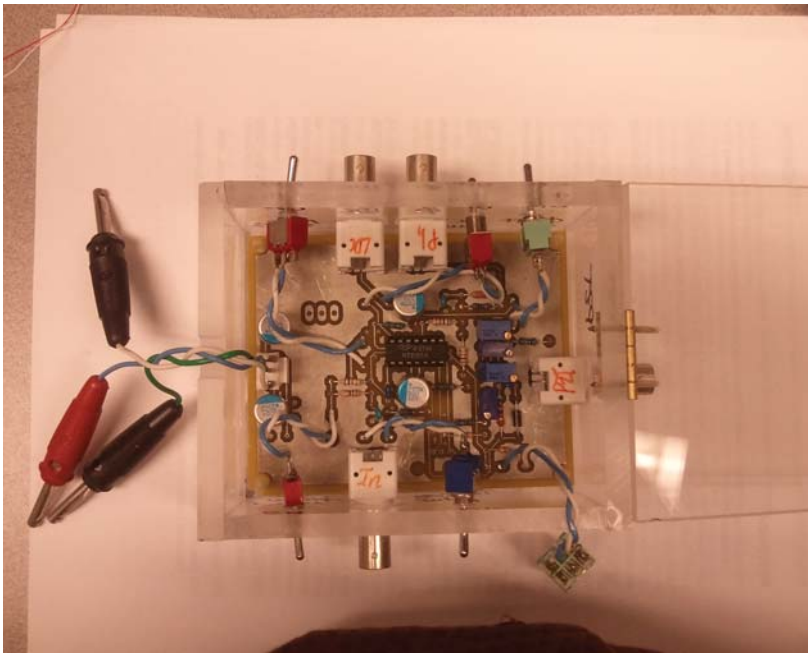

Figure B.5. The assembled servo lock circuit.

C. Laser Frequency Stabilization

There are many ways to stabilize the frequency of a laser. Common techniques are saturation spectroscopy, locking to a high finesse cavity, frequency and wavelength modulation spectroscopy, modulation transfer spectroscopy and techniques that use the dichroism of atomic vapor via magnetic interactions. Our lasers were stabilized by frequency modulation spectroscopy (FMS) as dictated by the availability of instrumentation. The basic idea in FMS is to add radio-frequency sidebands to the laser before it interacts with the atomic vapor. If the interaction is resonant, it generates a signal that varies as the modulation frequency. The signal can then be detected coherently by phase sensitive techniques. The idea is to perform the detection at a frequency that is away from common technical noise sources.

The basic arrangement for our setup is as shown in figures C.1, C.2. The optical arrangement is exactly the same as for saturation spectroscopy. We tap off about 3 mW power from the laser by means of a half-wave plate (HWP) and a polarizing beamsplitter cube (PBS). The tapped off light is split by a 50:50 PBS to generate probe and saturating beams. The probe beam is sent through an electro optic modulator (New Focus 4002, resonant, 7MHz EOM) attenuated to about 500μW and the saturation beam overlaps almost perfectly with the probe beam inside the cell. After exiting the cell, part of the probe beam is tapped off by a microscope coverslip and sent to a home-made Si photodiode (PD) to monitor saturation spectroscopy signals. The rest of the probe is detected by another homemade detector (based on the *EG&G* FFD100 Si PIN Photodiode). The photocurrent contains information about the frequency dependent response of the Cs atoms to the phase modulated probe light. The output from the fast PD (RF) is sent into a double balanced mixer (Mini circuits ZAD Series). An SRS DS345 provides a 7 MHz sine wave input, which is split by a 50:50 RF power splitter (Minicircuits ZSC-2-1) from one one half of the power is fed

into the mixer and the other half to the EOM. The intermediate frequency output after mixing (IF) was amplified (Mini-circuits ZFL500 series) before being sent into the Pre-amp and low pass filter setup. While the amplifier is not absolutely necessary, we found that pre-amplifying the signal before low pass filtering generated cleaner error signals. This amplified IF was sent into the B-Channel of an SRS560 Pre-amp and low pass filter. On the A channel, we connected a DC offset leveler which consisted of a potentiometer connected to a 9V battery. The pre-amp subtracted this offset and we eventually obtain our error signal at a zero baseline. Before the final error signal was obtained, we engaged the low pass loop filter on the Pre-Amp and set the cut off frequency to either 100 kHz or 300 kHz. The output signal has both high and low frequency components. These signals are first attenuated by passive variable attenuators and are then sent to servo. Attenuators are necessary because it is possible to saturate the servo at times and it provides a useful way to check the robustness of the locking as a function of signal strength input to the servo. The home made servo system is basically two integrators. The servo has two subsystems which selectively integrates fast and slow frequency components respectively. The fast and slow integrated signals show dispersion like features figure C.3. This completes the feedback loop.

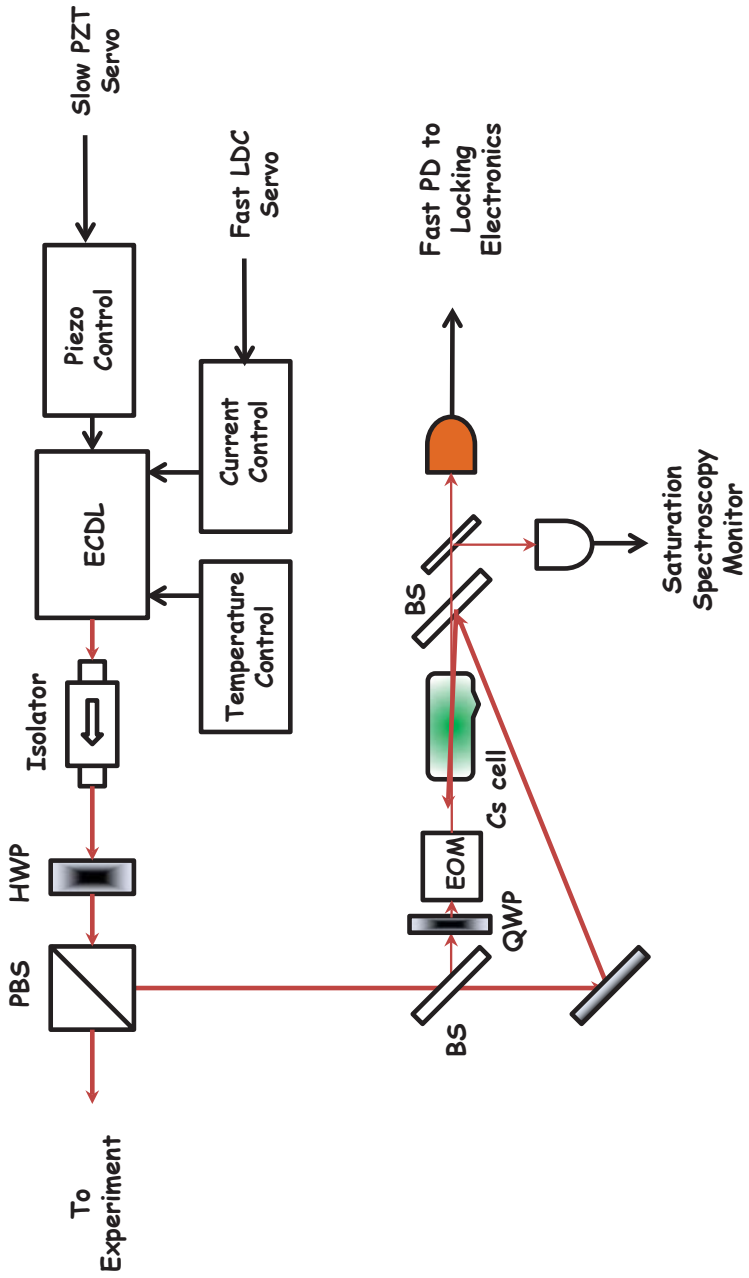

Figure C.1. Optical arrangement for FM Spectroscopy.

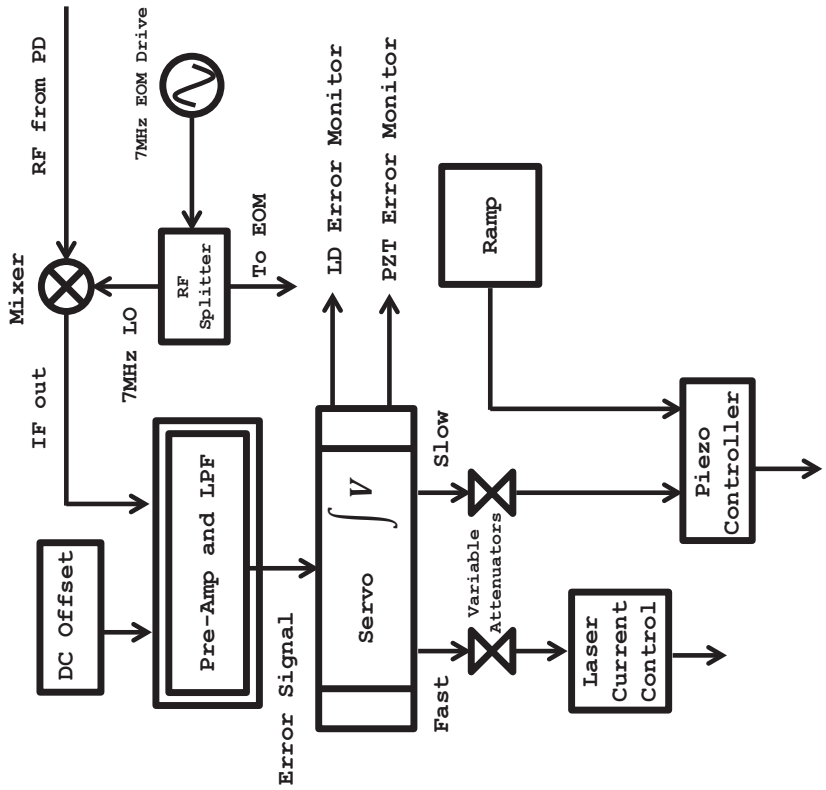

Figure C.2. Electronics for FM Spectroscopy.

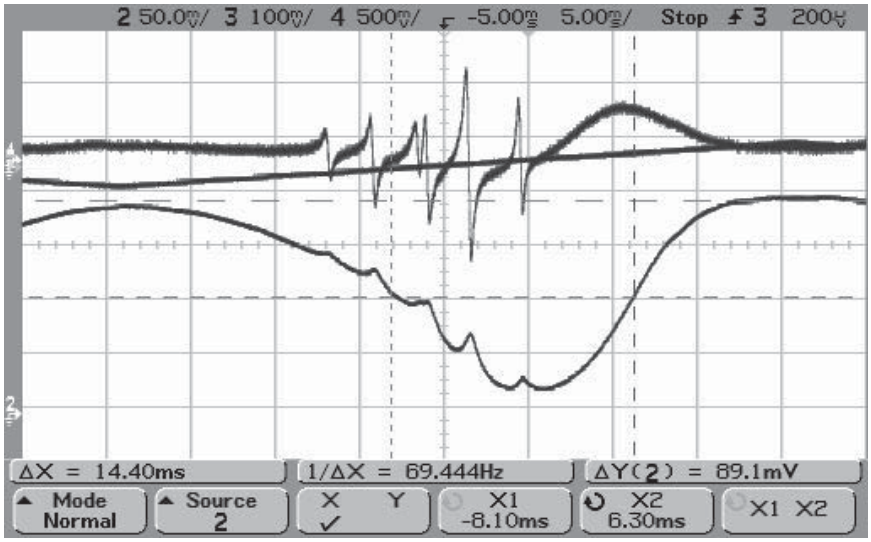

Figure C.3. The peaks are dispersion like signals from FM spectroscopy. Also shown are saturation spectroscopy peaks in a doppler well and the piezo ramp that provides the trigger for the display. Note that the baseline is not flat and this is inherent to FMS. The background can be removed by chopping the saturation beam.

To lock the laser, we first turn on the ramp signal for the PZT and scan the laser frequency to obtain saturation spectroscopy signals. We then engage the locking electronics at unity gain and attenuate servo inputs by more than 80 dB. This ensures a "loose" lock. Then we zoom in on the desired hyperfine transition, simultaneously observing the flattening of the error signal. Once we zoom in on one particular feature, we disengage the attenuators to "tighten" the lock. The final step is to fully turn off the ramp signal. At this point we are locked on top of the transition. The FM technique does not require dithering the laser current signal that is characteristic of side-lock techniques. We made a rough measurement of the laser linewidth based on the fluctuations in the error signal, which was calibrating by sending the light into a standard FP-cavity and generating a PZY voltage vs., frequency plot. We measured the linewidth to be about 1.3 MHz over a period of minutes.

D. C++ Code

```
1 /*
2 *Title: Calculation of Quantum Fluctuations in a Nonlinear ↩
    Interferometer with Harmonic Generation
3 *Author: Prashant Srinivasan
4 *Version: Release
5 *Date: September 2012
6 *Institution: Dept of Physics, IUPUI
7 *Credits: I am highly indebted to Edwin Tham and the authors of ↩
    the odeint library (http://headmyshoulder.github.com/odeint-↩
    v2/feedback.html)
8 */
9 #include <iostream>
10 #include <iterator>
11 #include <algorithm>
12 #include <boost/numeric/odeint.hpp>
13 #include <cmath>
14 #include <vector>
15 #include <fstream>
16 #include <iomanip>
17 #include <stdio.h>
18 #include <time.h>
19
20 using namespace std;
21 using namespace boost::numeric::odeint;
22 typedef std::vector< double > state_type;
```

```
23 //typedef bulirsch_stoer_dense_out <state_type > ↩
     dense_stepper_type;
24 //typedef runge_kutta_fehlberg78 < state_type >   stepper_type;
25 //typedef bulirsch_stoer < state_type >   stepper_type;
26 typedef controlled_runge_kutta< runge_kutta_cash_karp54< ↩
     state_type > > stepper_type;
27 //typedef controlled_runge_kutta< runge_kutta_dopri5< state_type↩
      > > dopri_stepper_type;
28 //typedef dense_output_runge_kutta< dopri_stepper_type > ↩
     dense_stepper_type;
29
30 class NLI_class {
31   private:
32     double gamma;
33     double th_initial;
34     double delta;
35   public:
36    NLI_class (double g, double theta_initial, double d) : gamma(↩
       g), th_initial(theta_initial),delta(d) {} //, delta(d) , ↩
       double d
37
38    void operator()( state_type &u , state_type &du , double z ) ↩
       {
39
40         du[0] = (u[0]*u[0]-1.0)*cos(u[1]+th_initial+delta);
41         du[1] = gamma * ((2.0/(1-u[0]*u[0]))-1.0/(u[0]*u[0]));
42         du[2] = gamma * (2.0/(1-u[0]*u[0]));
43         du[3] = gamma * (1.0/(u[0]*u[0]));
44
45         du[4]=(u[0]*u[4]*cos(u[1]+delta+th_initial)+sqrt(2.0)*↩
              sqrt(1.0-u[0]*u[0])*u[12]*cos(u[1]+delta+th_initial)+↩
```

```
    sqrt(2.0)*sqrt(1.0-u[0]*u[0])*u[16]*sin(u[1]+delta+↩
    th_initial)+u[8]*( (gamma/(1.0-u[0]*u[0]))- u[0]*sin(↩
    u[1]+delta+th_initial)));
46  du[5]=(u[0]*u[5]*cos(u[1]+delta+th_initial)+sqrt(2.0)*↩
    sqrt(1.0-u[0]*u[0])*u[13]*cos(u[1]+delta+th_initial)+↩
    sqrt(2.0)*sqrt(1.0-u[0]*u[0])*u[17]*sin(u[1]+delta+↩
    th_initial)+u[9]*( (gamma/(1.0-u[0]*u[0]))- u[0]*sin(↩
    u[1]+delta+th_initial)));
47  du[6]=(u[0]*u[6]*cos(u[1]+delta+th_initial)+sqrt(2.0)*↩
    sqrt(1.0-u[0]*u[0])*u[14]*cos(u[1]+delta+th_initial)+↩
    sqrt(2.0)*sqrt(1.0-u[0]*u[0])*u[18]*sin(u[1]+delta+↩
    th_initial)+u[10]*( (gamma/(1.0-u[0]*u[0]))- u[0]*sin↩
    (u[1]+delta+th_initial)));
48  du[7]=(u[0]*u[7]*cos(u[1]+delta+th_initial)+sqrt(2.0)*↩
    sqrt(1.0-u[0]*u[0])*u[15]*cos(u[1]+delta+th_initial)+↩
    sqrt(2.0)*sqrt(1.0-u[0]*u[0])*u[19]*sin(u[1]+delta+↩
    th_initial)+u[11]*( (gamma/(1.0-u[0]*u[0]))- u[0]*sin↩
    (u[1]+delta+th_initial)));
49  du[8]=(-u[0]*u[8]*cos(u[1]+delta+th_initial)+sqrt(2.0)*↩
    sqrt(1.0-u[0]*u[0])*u[16]*cos(u[1]+delta+th_initial)-↩
    sqrt(2.0)*sqrt(1.0-u[0]*u[0])*u[12]*sin(u[1]+delta+↩
    th_initial)+u[4]*( (-gamma/(1.0-u[0]*u[0]))- u[0]*sin↩
    (u[1]+delta+th_initial)));
50  du[9]=(-u[0]*u[9]*cos(u[1]+delta+th_initial)+sqrt(2.0)*↩
    sqrt(1.0-u[0]*u[0])*u[17]*cos(u[1]+delta+th_initial)-↩
    sqrt(2.0)*sqrt(1.0-u[0]*u[0])*u[13]*sin(u[1]+delta+↩
    th_initial)+u[5]*( (-gamma/(1.0-u[0]*u[0]))- u[0]*sin↩
    (u[1]+delta+th_initial)));
51  du[10]=(-u[0]*u[10]*cos(u[1]+delta+th_initial)+sqrt(2.0)↩
    *sqrt(1.0-u[0]*u[0])*u[18]*cos(u[1]+delta+th_initial)↩
    -sqrt(2.0)*sqrt(1.0-u[0]*u[0])*u[14]*sin(u[1]+delta+↩
```

```
    th_initial)+u[6]*( (-gamma/(1.0-u[0]*u[0]))- u[0]*sin↩
    (u[1]+delta+th_initial)));
52  du[11]=(-u[0]*u[11]*cos(u[1]+delta+th_initial)+sqrt(2.0)↩
    *sqrt(1.0-u[0]*u[0])*u[19]*cos(u[1]+delta+th_initial)↩
    -sqrt(2.0)*sqrt(1.0-u[0]*u[0])*u[15]*sin(u[1]+delta+↩
    th_initial)+u[7]*( (-gamma/(1.0-u[0]*u[0]))- u[0]*sin↩
    (u[1]+delta+th_initial)));
53  du[12]=(((gamma*u[16])/(u[0]*u[0]))-sqrt(2.0)*sqrt(1.0-u↩
    [0]*u[0])*u[4]*cos(u[1]+delta+th_initial)+sqrt(2.0)*↩
    sqrt(1.0-u[0]*u[0])*u[8]*sin(u[1]+delta+th_initial));
54  du[13]=(((gamma*u[17])/(u[0]*u[0]))-sqrt(2.0)*sqrt(1.0-u↩
    [0]*u[0])*u[5]*cos(u[1]+delta+th_initial)+sqrt(2.0)*↩
    sqrt(1.0-u[0]*u[0])*u[9]*sin(u[1]+delta+th_initial));
55  du[14]=(((gamma*u[18])/(u[0]*u[0]))-sqrt(2.0)*sqrt(1.0-u↩
    [0]*u[0])*u[6]*cos(u[1]+delta+th_initial)+sqrt(2.0)*↩
    sqrt(1.0-u[0]*u[0])*u[10]*sin(u[1]+delta+th_initial))↩
    ;
56  du[15]=( ((gamma*u[19])/(u[0]*u[0]))-sqrt(2.0)*sqrt(1.0-↩
    u[0]*u[0])*u[7]*cos(u[1]+delta+th_initial)+sqrt(2.0)*↩
    sqrt(1.0-u[0]*u[0])*u[11]*sin(u[1]+delta+th_initial))↩
    ;
57  du[16]=( ((-gamma*u[12])/(u[0]*u[0]))-sqrt(2.0)*sqrt↩
    (1.0-u[0]*u[0])*u[8]*cos(u[1]+delta+th_initial)-sqrt↩
    (2.0)*sqrt(1.0-u[0]*u[0])*u[4]*sin(u[1]+delta+↩
    th_initial));
58  du[17]=( ((-gamma*u[13])/(u[0]*u[0]))-sqrt(2.0)*sqrt↩
    (1.0-u[0]*u[0])*u[9]*cos(u[1]+delta+th_initial)-sqrt↩
    (2.0)*sqrt(1.0-u[0]*u[0])*u[5]*sin(u[1]+delta+↩
    th_initial));
59  du[18]=( ((-gamma*u[14])/(u[0]*u[0]))-sqrt(2.0)*sqrt↩
    (1.0-u[0]*u[0])*u[10]*cos(u[1]+delta+th_initial)-sqrt↩
```

```
            (2.0)*sqrt(1.0-u[0]*u[0])*u[6]*sin(u[1]+delta+th_initial));
60          du[19]=( ((-gamma*u[15])/(u[0]*u[0]))-sqrt(2.0)*sqrt(1.0-u[0]*u[0])*u[11]*cos(u[1]+delta+th_initial)-sqrt(2.0)*sqrt(1.0-u[0]*u[0])*u[7]*sin(u[1]+delta+th_initial));
61
62
63    }
64 };
65
66 struct streaming_observer {
67
68   std::ostream &m_out;
69   streaming_observer( std::ostream &out ) : m_out( out ) {}
70
71    void operator()( const state_type &x , double t ) const
72    {
73      m_out << t;
74     for( size_t i=0 ; i < x.size() ; ++i )
75       m_out << "\t" << x[i];
76     m_out << "\n";
77   }
78 };
79 inline void save(state_type& v, string filename)
80 {
81   ofstream output(filename);
82   for(int i=0;i<v.size();++i){
83     output << setprecision(64) << v[i] << endl;
84   }
85 }
```

```
86
87 int main(){
88   //clock_t start = clock(); //Uncomment if program execution ↩
       time is desired.
89
90   state_type x( 20 );
91   state_type Gamma;
92   state_type delta;
93   const double  pi=acos(-1.0);
94   const int delta_n=1000;
95   const double delta_step=(2*pi)/delta_n;
96   const double dz = 1e-15;
97   const double  zeta =0.5;
98   const double  theta_initial=0.00;
99   const double  u20=tanh(zeta);
100  const double  u10=1.0/cosh(zeta);
101  //double abs_error = 1.0e-10;
102  //double rel_error = 1.0e-10;
103  double d=0.0;
104  double G=0.0;
105
106  for(int i=0;i<=delta_n;i++){
107    //When i=0, the d=0.0 and G=0.0 are pushed into the vector.
108    delta.push_back(d);
109    Gamma.push_back(G);
110    // Compute delta and Gamma
111    d=d+delta_step;
112    G=-u10*u10*u20*sin(theta_initial+d);
113  }
114
115 save(delta,"delta.csv");
```

```
116 save(Gamma,"Gamma.csv");
117
118 //Numeric Integration
119     for (unsigned i = 0; i < Gamma.size(); ++i) {
120
121       x[0] = u20; x[1] = 0.0; x[2] = 0.0; x[3] = 0.0;
122       x[4] = 1.0; x[5]=  0.0; x[6]=  0.0; x[7]=  0.0;
123       x[8]=  0.0; x[9]=  1.0; x[10]= 0.0; x[11]= 0.0;
124       x[12]= 0.0; x[13]= 0.0; x[14]= 1.0; x[15]= 0.0;
125       x[16]= 0.0; x[17]= 0.0; x[18]= 0.0; x[19]= 1.0;
126
127
128       NLI_class nli_obj(Gamma[i], theta_initial,delta[i]);
129
130       /*Use this for Stoer Method, RK4_Cash. Uncomment the ↩
             appropriate function call*/
131       integrate_adaptive( stepper_type() , nli_obj , x , 0.0 , ↩
             zeta , dz , streaming_observer( std::cout ) );
132       //integrate_adaptive( runge_kutta4< vector<double > >(), ↩
             nli_obj , x , zeta , zeta , dz,streaming_observer( std::↩
             cout ) );
133
134           /*Use these for dopri_dense_output, stoer_dense ↩
                methods. Uncomment as need be. Error bounds need ↩
                to be uncommented as well.*/
135       //integrate_const( dense_stepper_type() , nli_obj , x , ↩
             0.0 , zeta , dz , streaming_observer( std::cout ) );
136       //integrate_adaptive( stepper_type( default_error_checker<↩
              double >( abs_error , rel_error ) ) , nli_obj , x , ↩
             0.0 ,zeta , dz , streaming_observer( std::cout ) );
137   }
```

```
138
139 //printf("Time elapsed: %f\n", ((double)clock() - start) / ↩
      CLOCKS_PER_SEC); //Uncomment this to get the program run time↩
      .
140 //system("PAUSE"); //Uncomment this if need be.
141 }
142
143 /*
144 *Title: Sorting program
145 *Author: Prashant Srinivasan
146 *Version: Release
147 *Date: September 2012
148 *Institution: Dept of Physics, IUPUI
149 *Instructions: Take the EXE generated by the main simulation and↩
       in the windows prompt type "EXE_name">data.txt. The sort is ↩
      performed on the data.txt file.
150 */
151
152 #include <string>
153 #include <fstream>
154 #include<iostream>
155 using namespace std;
156
157 void sort(std::string const& in_fn, std::string const& out_fn)
158 {
159   std::ifstream is(in_fn);
160   std::ofstream os(out_fn);
161
162   std::string line;
163   std::string previous_line="4";
164   while (std::getline(is, line)){
```

```
165     if (line.size() && std::stod(line) == 0.0 && previous_line ↩
           != "4"){
166             os << previous_line << '\n';
167     }
168     previous_line=line;
169 
170   }
171 }
172 
173 int main()
174 {
175 
176   sort("C:/data.txt","C:/sorted.txt");
177 }
```

VITA

VITA

Prashant Srinivasan

Education

- Ph.D., Physics, Indiana University-Purdue University Indianapolis (December 2012).
- M.S., Physics, Indiana University-Purdue University Indianapolis (August 2007).
- B.E., Telecommunications Engineering, B.M.S College of Engineering, Bangalore, India (September 2001).

Awards

- School of science TA award, IUPUI (2012).
- Outstanding TA award, American Physical Society (2012).
- Outstanding TA award, American Physical Society (2008).
- Research investment fellowship, IUPUI (2004-2006).
- Academic scholarship, IUPUI (2004-2012).
- Outstanding research presentation, Sigma Xi, Lamar University (2003).
- Academic scholarship, Lamar University (2003).

Research experience at IUPUI

- Numerical simulation of quantum fluctuations in harmonic generation (Fall 2011-Spring 2012).
- Experimental investigation of generation of atomic coherence in Cs atoms (Fall 2007-Fall 2011).

- Development of stable diode laser systems (Fall 2004-Fall 2007).
- Interaction of lithium with lipid membranes (Fall 2007-Fall 2010).
- Interaction of buffers with lipid membranes (Fall 2007-Fall 2010).

Research experience at the Indian Institute of Science

- Second harmonic generation (Fall 2002-Spring 2003).
- Modeling of Erbium doped fiber amplifier systems (Fall 2002-Fall 2003).
- DNA on a chip (Fall 2002-Spring 2003).

Teaching experience

- Laboratory teaching assistant IUPUI, (2004-2012).
- Course instructor, IUPUI (Summer 2011).
- Instructor, Summer school, Indian Institute of Astrophysics (Summer 2003).
- Teaching assistant, Indian Institute of Science (Summer 2001-2003).

Publications and presentations

- F. Shafiei, P. Srinivasan, and Z. Y. Ou. Generation of three-photon entangled state by quantum interference between a coherent state and parametric down-conversion. *Physical Review A*, v70,043803,2004.
- P.Srinivasan, Z.Y. Ou, Evolution of quantum fluctuations in harmonic generation for arbitrary phase. *In preparation.*
- P. Srinivasan, Z.Y Ou, Quantum Fluctuations and Precision Phase Measurements. *Proc.* 127^{th} *annual meeting of the Indiana Academy of Science, March 2012*
- M. M. Koerner, A. Mossa-Basha, P. Srinivasan, H.I. Petrache. Interaction of Buffers with Lipid Membranes. *Volume 96, Issue 3, Supplement 1, February 2009, Pages 459a*

- P. Srinivasan, Suppression of quantum fluctuations, squeezing and nonlinear interferometry in harmonic generation. *Invited talk, IUPUI* (2012).
- P. Srinivasan. High gain C- band EDFA. *Proc.* 4^{th} *annual Sigma-Xi Lamar Student Research Conference, April 2003*